Entropy driven and reaction driven self-assembly of colloidal semiconductor nanocrystals.

This thesis was funded by the “Nederlandse Organisatie voor Wetenschappelijk onderzoek (NWO) Chemische wetenschappen (CW)” (TOP-grant 700.53.308) and by the European Union 7th framework programme “NanoSpec” program (NMP-2009-1.2.-1)
Printed by GVO drukkers & vormgevers B.V.
ISBN/EAN: 978-90-393-5856-6

Entropy driven and reaction driven self-assembly of colloidal semiconductor nanocrystals

Entropie gedreven and reactie gedreven zelf-organisatie van colloïdale halfgeleidende nanokristallen

(met een samenvatting in het Nederlands)

Proefschrift

ter verkrijging van de graad van doctor aan de Universiteit Utrecht op gezag van de rector magnificus, prof. dr. G.J. van der Zwaan, ingevolge het besluit van het college voor promoties in het openbaar te verdedigen op woensdag 14 november 2012 des middags te 12.45 uur.

Door

Wilhelmus Hubertus Evers

geboren op 14 mei 1985, te Weert

Promotoren: Prof. dr. D. Vanmaekelbergh
Prof. dr. A. Meijerink

Table of Contents

Chapter 1

Introduction to semiconductor nanocrystals and nanocrystal self-assembly

1.1 Introduction

Nanocrystals (NCs) have become of great interest in the last decades. Nowadays different strategies for the synthesis and preparation of colloidal nanocrystals have been developed resulting in a good control of their size, shape, composition and surface chemistry. This is required if one wishes to obtain suspensions with NCs with a well-defined electronic structure and optical properties.[1] Especially semiconductor nanocrystals, i.e. quantum dots, show interesting properties due to the opportunity to tune the band gap and conduction electron and valence hole levels by only changing the size of the nanocrystal.

Furthermore, nanostructured materials can be obtained by self-assembly of colloidal nanocrystals into NC superlattices. In the 1990's Murray *et al.* showed already that NCs show the propensity to self-assemble into ordered structures, i.e. lattices composed of NC building blocks.[2] After the demonstration of single-component superlattices composed of CdSe nanocrystals, binary superlattices (BNSL) were realized with NC of different diameters, nature and composition, for instance semiconducting, metallic or magnetic.[2-14] Many of these BNSL showed interesting properties.[4, 5, 13-16] For instance, p-type conductivity was obtained in BNSLs of PbTe and Ag2Te NCs[4] and magnetoresistance was reported for superlattices that contain paramagnetic iron oxide nanocrystals.[14, 17] The BNSLs were prepared with various methods and conditions, e.g. (fast) evaporation of the solvent or non-solvent destabilization.[7, 18, 19] Although a lot of successes have been achieved in the recent past, the driving forces of the lattice formation are not completely understood.

In this chapter, a general introduction to colloidal semiconductor nanocrystals will be given. The evolution of the energy levels from the bulk semiconductor case to single semiconducting nanocrystals (quantum dots) will be briefly addressed in the first part. In the second part of the introduction the focus will be on the self-assembly process of nanocrystals in a suspension.

1.2 Nanocrystals

Nanocrystals are what the word implies: crystalline structures with dimensions in the nanometre regime. NCs can have various elemental compositions and they can be metallic, magnetic or semiconducting. For all type of nanocrystals, the magnetic, electronic and optical properties may vary strongly with the size and shape. This is, however, due to a variety of different physical effects. In the case of semiconductor nanocrystals, the confinement of the electron and hole excitations in the nanocrystal host causes that the energies of the valence hole and conduction electron and the band gap become dependent on the size. In the next section a more detailed explanation of this size effect will be given.

1.2.1 Bulk semiconductors

To understand the properties of QDs, the underlying principles of bulk semiconductors have to be understood. Therefore, a brief description of bulk semiconductors is given in this section.

An electron travelling in a semiconductor can be seen as travelling through a periodic potential caused by the crystal lattice, instead of as a free electron. For a free electron within a potential well the time-independent Schrödinger equation in one dimension is given in equation (1.1).

$$-\frac{\hbar^2}{2m}\frac{d^2}{dx^2}\psi(x) + V(x)\psi(x) = E\psi(x) \quad (1.1)$$

In a crystal, the potential energy *V(x)* has to satisfy the condition set by the periodic lattice of the crystal: the potential energy at *V(x+a)*, where *a* is the lattice constant, should be the same as the potential energy at *V(x)*. The equation (1.1) can be rewritten after a translation of the wavefunction *ψ(x)* by the lattice constant *a, i.e. (ψ(x+a))* to equation (1.2).

$$-\frac{\hbar^2}{2m}\frac{d^2}{dx^2}\psi(x+a) + V(x)\psi(x+a) = E\psi(x+a) \quad (1.2)$$

After a translation of the lattice constant *a* along the lattice, the eigenvalue of the Schrödinger equation *E*, should have the same value for the original and the translated coordinate. This implies that the wavefunctions *ψ(x)* and *ψ(x+a)* should only differ with a phase factor. The so called Bloch wavefunctions satisfy this condition.[20, 21] The wavefunction in equation (1.2) could be rewritten as follows,

$$\psi_{Bloch,k}(x) = e^{ikx} \cdot u_k(x). \quad (1.3)$$

The first term is a plane wave where k is the wavevector ($k=2\pi/a$). The second term u_k is a function periodic with the lattice constant, hence, $u_k(x)=u_k(x+ka)$ and the subscripted '*k*' stands for different wavenumbers. This periodicity has consequences for the energy dispersion of the electrons. When the electrons have a wavelength different from the periodic lattice spacing, they are only slightly disturbed by the periodicity and therefore behave like free electrons with the same energy dispersion of a free electron in vacuum. On the other hand, when the electrons have a wavelength near that of the periodic lattice they are reflected by the lattice. A free electron in vacuum can be described by equation (1.3), with $u_k(x)=1$ and energy:

$$E(k) = \frac{\hbar^2 k^2}{2m} \quad (1.4)$$

An electron in free space has a continuum energy dispersion, as depicted by the dashed line in Figure 1.1a. In a periodic lattice, however, when the wavelength of the electron is close to the lattice spacing *a*, the electrons are reflected by the periodic potential coming from the lattice. At a wave number of $\pm\frac{\pi}{a}n$ the wave function is a standing wave due to the reflections at the periodic lattice. From this, a forbidden energy interval arises for which no propagating wave exists. These so-called forbidden energy intervals are called band gaps. An energy dispersion relation for a lattice with a lattice constant of *a* is given in Figure 1.1a.

Due to the periodicity, the whole range of *k* values consist of equivalent intervals with an interval spacing of 2π/a. Each such interval is called a Brillouin zone, after Léon Brillouin who started this notation.[20, 21] Since the whole range of energy values is divided in equivalent regions of wave numbers differing in integer number of 2π/a, all the branches in the dispersion curve (Figure 1.1A) can be brought together in a so called reduced zone scheme, given in Figure 1.1B. The reduced dispersion curve is also referred to as the band structure[21].

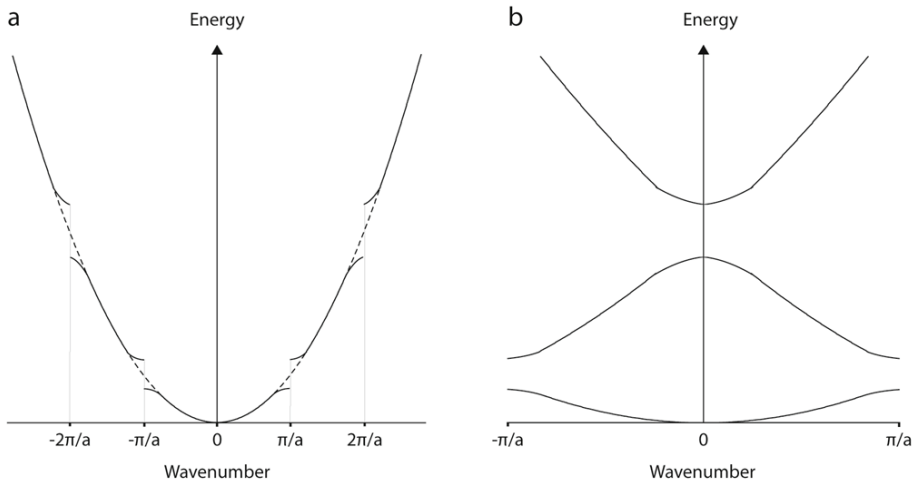

Figure 1.1: Energy dispersion relation of a particle in a one-dimensional periodic potential (a – solid line) and of a free electron in vacuum (a – dashed line). b) Reduce zone scheme of the energy dispersion relation of a particle in a one dimensional periodic potential. [20]

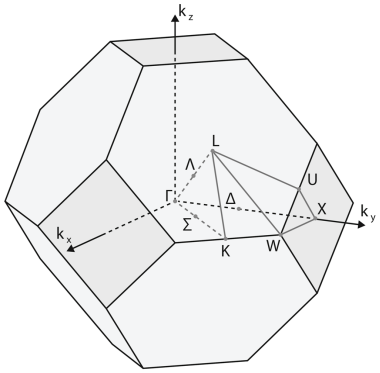

Figure 1.2: The first Brillouin zone for a face-centered cubic lattice.[21]

In a 3-dimensional crystal the Bragg reflections of the electrons become more complex. Bragg reflections due to the periodicity of the lattice will happen in all three dimensions. As an example the Brillouin zone of PbSe will be discussed. The first Brillouin zone for an FCC lattice (e.g. the rock salt PbSe lattice) can be represented by a truncated octahedron as shown in Figure 1.2.[21] For PbSe the fundamental bandgap is located at the L points in the Brillouin zone, i.e. in the {111} direction in reciprocal space.[22, 23] Eight L points are present in the first Brillouin zone as is evident from Figure 1.2. Since every L-point is shared with a neighbouring Brillouin zone, the fundamental bandgap of PbSe is 4-fold degenerate or 8-fold if spin is included. Hence, the lowest exciton state of PbSe ($1S_h$-$1S_e$) is 64-fold degenerate, leading to a complex exciton fine structure for PbSe.[22, 23]

1.2.2 Semiconductors nanocrystals

At the nanoscale the properties of semiconductors change. Quantum confinement of the electron, hole, or electron-hole excitations occurs resulting in discrete electronic energy levels and distinct optical properties. The quantum confinement commences when the Bohr radius of the exciton, the most probable distance between the electron and hole in an exciton, becomes larger than the radius of the crystal in which it is confined.[1, 24] The equation for the exciton Bohr radius is given in equation (1.5),

$$a_b = \frac{4\pi\varepsilon_0\varepsilon\hbar^2}{\mu_{eh}e^2} \qquad (1.5)$$

where μ_{eh} is the reduced mass of the electron and hole.[25] The exciton Bohr radius in a semiconductor crystal can be considerable (between ~2 and 100 nm) due to a small electron/hole mass and/or high dielectric constant. Three distinct regimes for confinement can be defined (Figure 1.3). When the Bohr radius is much smaller than the crystal, no confinement is observed. However, when the Bohr radius is comparable with the crystal radius weak confinement can be expected, i.e. the weak confinement regime. The exciton

does no longer 'fit' into the nanocrystal, hence the electron and hole have to increase their kinetic energy. Consequently, the energy gap, E_g, has to increase and the states near the edge of the conduction and valance band become discrete. In the last regime, i.e. the strong confinement regime, the crystal size is much smaller than the Bohr radius. At this size, the band gap increases even more and the energy levels at the edges of the band gap become more separated in energy. Analogous to atoms, the states near the edge of the band gap are identified as S, P, D, etc. states depending on their symmetry.[1, 24] Nanocrystals that show strong quantum confinement are called quantum dots.

An alternative way of approaching quantum confinement is starting from an atomic point of view similarly as in the construction of molecular orbitals (MO) by linear combination of atomic orbitals (LCAO), i.e. the quantum dot is seen as a big molecule. The simplest case as example for the LCAO method is a di-atomic molecule. An electron of this molecule can be either found in the atomic orbital of atom 1 or 2, hence, the overall wavefunction is a superposition of these two atomic orbitals. The energy levels of two single orbitals split in two molecular orbitals, the region of constructive (bonding) interference and the region of destructive (anti-bonding) interference of the two atomic wavefunctions.[26] When only the bonding MO is filled, e.g. in semiconductors where the Fermi level lies in-between the two bands, this orbital is called the highest occupied molecular orbital (HOMO) and the empty anti-bonding orbital is called the lowest unoccupied molecular orbital (LUMO) while the gap between the HOMO and LUMO is called the band gap. When the molecule size is increased more energy levels arise with smaller difference between the HOMO and LUMO MOs (Figure 1.4). For large molecules, i.e. bulk material, the energy levels form a nearly continuous band, see Figure 1.4.[24, 27]

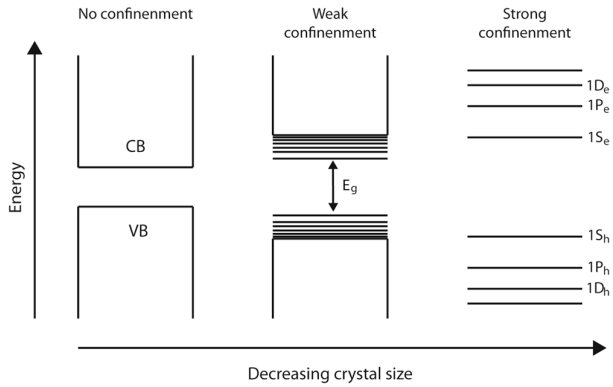

Figure 1.3: Quantum confinement. The quantum confinement increases with decreasing crystal size and discrete energy levels emerge at the band edges. Moreover, the band gap, E_g, increases with decreasing crystal size.

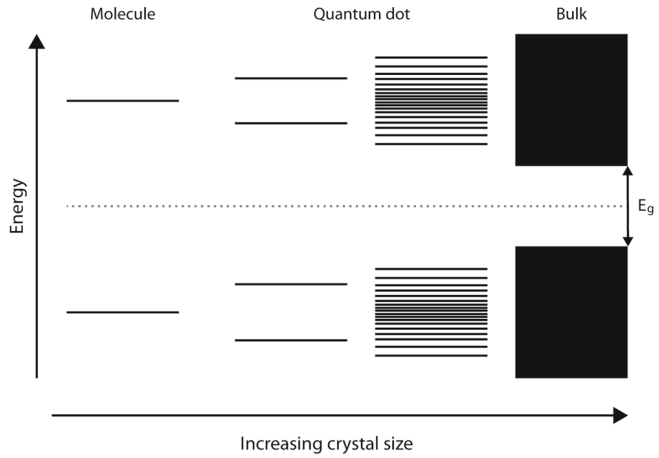

Figure 1.4: Evolution of the energy level-distribution, from a di-atomic molecule to a bulk crystal. The band gap decreases, i.e. the gap in-between the HOMO and LUMO levels, as function of the crystal size. Hence a quantum dot can be seen as a large molecule.

1.3 Superlattice formation and the hard-sphere model

The formation of nanocrystal superlattices from a NC suspension can be driven by several thermodynamic driving forces. In general, we can deduce three different cases of this kind of self-assembly i.e. purely entropic, purely energetic (enthalpy) and a combination of the two. Purely entropic self-assembly is for instance observed in non-interacting hard-sphere like systems. In contrast, by inducing a charge difference by charged ligands, or activation of certain facets of the nanocrystals, the self-assembly can be tuned to be predominantly energy driven. In certain situations, for example in anisotropic rod-like systems the van der Waals (vdW) attractions become important, it can be expected that both the entropic and enthalpic contributions are important in the assembly. In this section, we will give a brief summary of the work reported in the literature.

Regardless of the kind of superlattice and preparation method, nanocrystal superlattices form to lower the Gibbs free energy of the system. Although superlattice formation has been studied extensively, the energy contributions and interactions are not yet fully quantified. The change of the Gibbs free energy (ΔG) of the system in terms of the enthalpy (ΔH_{sys}) and entropy (ΔS_{sys}) can be written as:

$$\Delta G_{sys} = \Delta H_{sys} - T\Delta S_{sys} \quad (1.6)$$

Hence, to minimize the Gibbs free energy of a system the enthalpy (ΔH) has to minimize and/or the entropy has to increase. Here, it is more convenient to give the Gibbs free energy as a function of the time *t* during which the superlattice formation occurs:

$$G(t) - G_i = [H(t) - H_i] - T[S(t) - S_i] \quad (1.7)$$

In equation (1.8) the parameter *t* is a parameter that measures the evolution of the process at a certain time, while the subscript *i* denotes the initial state of the system before any change has occurred. The change in time can, for instance, reflect the increase of concentration (evaporation of the solvent) or the diffusion of a 'bad' solvent in a solution (1.7).[28] First we will discuss the entropy. To obtain a lower Gibbs free energy, the entropy should be maximized, i.e. the degrees of freedom should be maximized. The entropy parameter is especially important for hard-sphere systems with only short-range repulsive interactions ($H(t)-H_i \approx 0$). Hard-spheres have been studied extensively in the 'large' colloids world and have only short-range hard-core repulsion.[29] Hence, the phase behavior is determined entirely by entropy and depends only on volume fraction ϕ occupied by the nanocrystals in the suspension (filling fraction).[29, 30] It seems contradictory that the entropy of a system of hard spheres is increased by the formation of a crystal and indeed the conformational entropy of the spheres is decreased. However, if one compares a concentrated liquid (volume fraction ≈ 49%) with the ordered phase of the same density, the gain in entropy due to the larger free volume per particle for local movement in the crystal lattice (49%

volume fraction), more than compensates this loss in conformational freedom.[29, 30] Hence, the entropy increases in a crystalline solid compared to the disordered phase of high density, opening the pathway to crystallization of hard spheres. From the above, it is reasonable that crystal structures with a high packing fraction are favored. We now focus on suspensions that contain hard spheres of two different diameters. Simulations show that binary crystal structures with a maximum density comparable or higher than the packing fraction of the single component superlattices (fcc/hcp ρ=0.74)[10] can be formed by hard spheres of two different diameters. In Figure 1.5 the packing fraction versus the size ratio of binary mixtures is given for a number of common crystals structures which are already observed previously in literature.[9] The packing fraction of some of the structures given in Figure 1.5 is lower than the packing fraction of the single component fcc/hcp lattice, e.g. the maximum packing fractions of the Laves phases ($MgZn_2$, $MgCu_2$ and $MgNi_2$) is 0.71 and the maximum packing fraction for CsCl is 0.73. Hence, the packing fraction alone is not the only criterium to evaluate the stability of various crystal structures.[31] Nevertheless, it does give a good indication in many circumstances. In the literature, many examples exists where full free energy calculation are used to find out which crystal structures are stable with only entropic contributions. Hynninen *et al.* showed that the laves phases are stable with only entropic contributions, while e.g. the CsCl phase could only be stabilized if repulsive/attractive interactions are added.[32] In Table 1.1 a summary is given of the crystal structures that have been shown to be stable for a binary mixture of hard-spheres as function of the size ratio. In chapter 2, we will investigate in detail if organically capped semiconductor and/or metal NCs in a good solvent can crystallize as hard spheres.

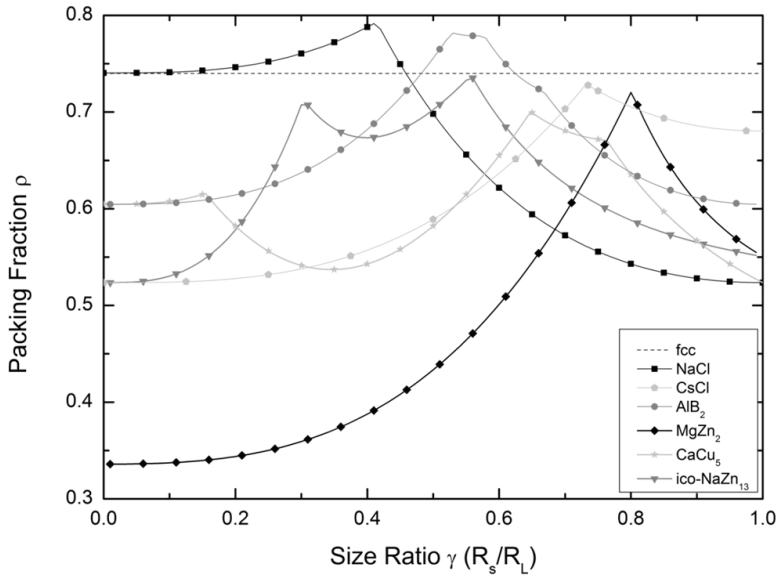

Figure 1.5: Space filling curves of NaCl, CsCl, AlB_2, $MgZn_2$, $CaCu_5$ and ico-$NaZn_{13}$ in the size-ratio range $0 \leq \gamma \leq 1$.

Size Ratio (γ)	Stable crystal structure	Reference
0.033	fcc with disordered small particles	[33]
0.05	fcc with disordered small particles	[33]
0.10	fcc with disordered small particles	[33]
0.20	fcc with disordered small particles	[33]
0.414	NaCl	[34]
0.45	NaCl and AlB_2	[34]
0.50	AlB_2	[35]
0.54	AlB_2 and ico-AB_{13}	[35]
0.58	AlB_2 and ico-AB_{13}	[35, 36]
0.59	AlB_2 and ico-AB_{13}	[35]
0.60	AlB_2 and ico-AB_{13}	[35]
0.61	AlB_2 and ico-AB_{13}	[35]
0.625	ico-AB_{13}	[35]
0.74	only fcc_L and fcc_S	[32]
0.76	Laves Phases ($MgZn_2$, $MgCu_2$, $MgNi_2$)	[32]
0.80	Laves Phases ($MgZn_2$, $MgCu_2$, $MgNi_2$)	[32]
0.82	Laves Phases ($MgZn_2$, $MgCu_2$, $MgNi_2$)	[32]
0.84	Laves Phases ($MgZn_2$, $MgCu_2$, $MgNi_2$)	[32]
0.85	Eutectic solid solution	[37]
0.875	Eutectic solid solution	[37]
0.90	Azeotropic	[37]
0.92	Azeotropic	[37]
0.9425	Azeotropic	[37]
0.95	fcc solid solution (spindle)	[37]

Table 1.1: A list of structures as a function of the size ratio which have been shown to be stable in hard-sphere systems.

Enthalpy accounts for many different terms of interaction, both attractive and repulsive. The interactions could for instance be London-Van der Waals forces (vdW), charge-charge, charge-dipole and dipole-dipole interactions.[8, 10, 38-40] Different particles have different properties and hence different interactions. In Figure 1.6, results for the effective interactions between two spherical organically capped nanocrystals of semiconductor (CdSe) and of metallic (Au) nature without charge or dipole are given. The calculations hold for organically capped nanocrystals in an ideal solvent (i.e. interactions between the capping molecules of two particles are screened by a very similar capping-solvent interaction). It is evident that the interaction between two metallic nanocrystals is much stronger than the interactions between two semiconductor particles ($\geq$ 2 kT versus $<<$ kT respectively). These interactions already indicate that the self-assembly process of (metallic) spherical NCs is a complex process, which could be highly sensitive to subtle changes in environment.

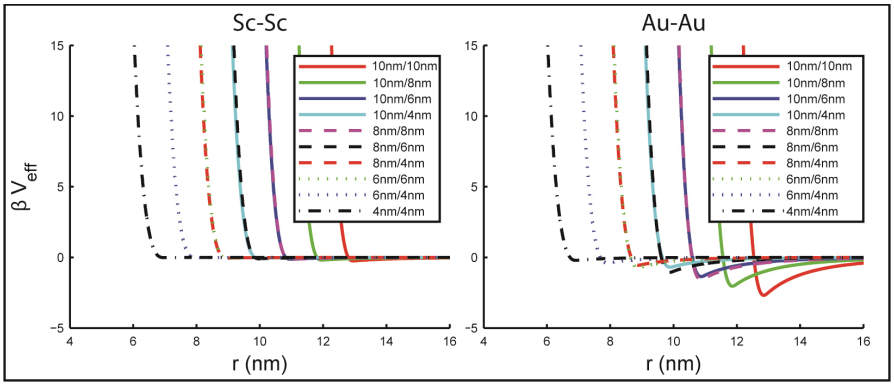

Figure 1.6: Effective interactions between nanocrystals as function of nanocrystal size. Left interactions for Semiconductor-Semiconductor (Sc-Sc) and right Gold-Gold (Au-Au) nanocrystals with Hamaker constant A =0.3 eV and A=3 eV, respectively. More details can be found in chapter 2.

Next, we consider nanocrystals with an anisotropic shape. It can be imagined that particles other than spheres, e.g. rods or octapods, show stronger vdW interactions between the cores due to their large size and anisotropic shape (attraction along the length of the rods/pods). For instance it has been shown that the self-assembly of monodisperse octapod-shaped nanocrystals into chains and subsequently the self-assembly of these sheets into superstructures is mainly driven by vdW interactions.[41, 42] The self-assembly of the octapods was induced by slightly decreasing the stability of the colloidal suspension by changing the composition of the solvent. In this manner the strength of the vdW interactions between the octapods could be tuned.

Another system where the interaction between two colloids becomes important is that of self-assembly of nanorods in a good solvent under controlled evaporation of the solvent. Large sheets of upstanding hexagonally packed rods have been obtained and several studies of the driving forces have been undertaken showing the complex nature of the self assembly of the nanorods. For instance, CdS or CdSe nanorod self-assembly is, among others, subjected to interactions of net charge, dipole-dipole interactions and vdW interactions.[43-45] It also has been shown that the type of solvent is vital to the self-assembly process. For instance Singh *et al.* used chloroform as solvent, which has a permittivity such that the nanorods dissolve but still considerably screens the Coulomb and dipole-dipole interactions.[45] As a result, the self-assembly in chloroform (compared to toluene) was not observed due to the reduction of the electrostatic forces. Furthermore, Pietra *et al.* showed that the formation of nanorod-sheets is a complex process consisting of several steps.[46] First the rod bundles form in solution (very probably due to vdW attractions). Secondly these bundles are adsorbed at the solvent/air interface (evaporation front). And lastly, the bundles pack together at the interface to maximize attractive vdW attractions. This scheme already indicates that the relative importance of different interactions is different at different stages of the self-assembly process.

The last type of systems to discuss here are systems which are entirely energy driven and form irreversible chemical bonds between the separate building blocks, i.e. oriented attachment of nanocrystals into rods or sheets. Oriented attachment is the process in which nanometer sized crystals fuse by atomic bonding of specific crystal facets. Oriented attachment is different from normal nanocrystal self-assembly in the strength of the driving forces. Where nanocrystal self-assembly is mainly driven by entropic and/or vdW forces, oriented attachment is driven by inter-atomic bonding. Therefore where 'normal' self-assembly is a reversible process, oriented attachment is an irreversible aggregation process which could be more difficult to control. Several examples exist in literature of oriented attachment of nanocrystals into rods, wires, rings, or sheets.[47-51] For example Cho *et al.* changed the synthesis parameters for the synthesis of spherical particles and found oriented attachment of the in-situ created nanocrystals along the {100} crystal facet. They argued that the formation was aided by the presence of a dipole moment due to the uneven distribution of the {111} Pb and Se facets. Once two nanocrystals attach the electrical dipole is enhanced leading to further elongation along the rod, resulting in wires[48]. Furthermore, Schliehe *et al.* altered a PbS synthesis by addition of a chlorine containing co-solvent which altered the nucleation and growth rates of the synthesis and allowed the {110} facets to attach.[47] Moreover, the dense packing of capping ligands (oleic acid) on the {100} horizontal planes prevented the formation of 3D crystals. In both examples the synthesis was modified to achieve oriented attachment and the attachment took place in the bulk of solution.

The initiation of superlattice formation from nanocrystals can also be discussed on the basis of the chemical potential, i.e. equation (1.7). The chemical potential μ *is* determined by the standard chemical potential μ^* of the nanocrystals in a certain solvent and the concentrations c of the nanocrystals relative to a reference concentration, the Boltzmann constant k_B and the temperature T.[25, 26]

$$\mu = \mu^* + k_B T \ln\left(\frac{c}{c_{ref}}\right) \qquad (1.7)$$

The formation of a superlattice is only possible when the chemical potential of the dispersed nanocrystal is higher than the chemical potential of the nanocrystal in a superlattice. Two possible opportunities arise to change the chemical potential, i.e. changing the standard chemical potential μ^*, and changing the concentration c. The most obvious way to increase the concentration is to evaporate the solvent. This method for superlattice crystallization is widely applied in literature.[8, 9] On the other hand the standard chemical potential (a measure for the potential energy) can be changed by changing the nanocrystal/solvent interaction, by (slow) addition/diffusion of a so called "bad"-solvent into a stable nanocrystal suspension. The addition causes a destabilization of the nanocrystals due to the unfavorable change in composition of the surrounding medium. Consequently, the chemical potential will increase and colloidal crystallization will lower

the free energy of the system. This method of superlattice formation for nanocrystals was first reported by Murray *et al.*[2]

1.4 Outline of this thesis

In the first chapters of this thesis we present results on the self-assembly of colloidal semiconductor nanocrystals. In chapter 2 we report on the formation of binary superlattices consisting of two different semiconductor nanocrystals or a semiconductor and metallic nanocrystal. We consider the key question if only entropy or also attractive forces are important in the self-assembly. This study is performed by comparing the observed binary superlattices with the predictions of hard-sphere models.
In chapter 3, we present the first ternary superlattice structure obtained from a suspension containing three differently sized semiconductor nanocrystals (PbSe and CdSe). We show that, most probably, the interactions in this more complex system are similar as in the binary case.
In the fourth chapter we utilize electron tomography to characterize the superlattice structure in a three-dimensional way. This also furthers our understanding of the self-assembly process. For instance we show that self-assembly induced by solvent evaporation takes place at the solvent-air interface and not in the bulk of solution. Moreover, we identify a new crystal phase not identified before in the literature.
In chapter 5, we performed a study on the oriented attachment of PbSe nanocrystals on an ethylene glycol substrate. We demonstrate that by tuning 'simple' chemical parameters such as temperature or concentration we can have full dimensional control and can prepare PbSe rods/wires or 2D sheets that have an added square or honeycomb superlattice structure. In addition we show that we can exchange the Pb^{2+} ions for Cd^{2+} or Cu^{+} ions, resulting in new semiconductor compounds with preservation of the superlattice structure.
In the 6th chapter we study the optical properties of one of the NCs used in the previous chapters, i.e. PbSe|CdSe core|shell particles. The photoluminescence of these particles shows two peaks which become more separated in energy when the core diameter is decreased below 4 nm. We show that these two peaks are due to intrinsic exciton transitions in each NC, rather than emission from different NC sub-ensembles. Most probably, the splitting is due to intervalley coupling and electron-hole exchange in the 64-fold exciton system.

References

1. Rogach, A. L., *Semiconductor Nanocrystal Quantum Dots*. 2008.
2. Murray, C. B.; Kagan, C. R.; Bawendi, M. G. *Science* **1995,** 270, (5240), 1335-1338.
3. Rogach, A. L.; Talapin, D. V.; Shevchenko, E. V.; Kornowski, A.; Haase, M.; Weller, H. *Advanced Functional Materials* **2002,** 12, (10), 653-664.
4. Urban, J. J.; Talapin, D. V.; Shevchenko, E. V.; Kagan, C. R.; Murray, C. B. *Nat Mater* **2007,** 6, (2), 115-121.
5. Heath, J. R. *Nature* **2007,** 445, (7127), 492-493.
6. Kiely, C. J.; Fink, J.; Brust, M.; Bethell, D.; Schiffrin, D. J. *Nature* **1998,** 396, (6710), 444-446.
7. Redl, F. X.; Cho, K. S.; Murray, C. B.; O'Brien, S. *Nature* **2003,** 423, (6943), 968-971.
8. Shevchenko, E. V.; Talapin, D. V.; Kotov, N. A.; O'Brien, S.; Murray, C. B. *Nature* **2006,** 439, (7072), 55-59.
9. Chen, Z.; O'Brien, S. *ACS Nano* **2008,** 2, (6), 1219-1229.
10. Chen, Z.; Moore, J.; Radtke, G.; Sirringhaus, H.; O'Brien, S. *Journal of the American Chemical Society* **2007,** 129, (50), 15702-15709.
11. Shevchenko, E. V.; Talapin, D. V.; O'Brien, S.; Murray, C. B. *Journal of the American Chemical Society* **2005,** 127, (24), 8741-8747.
12. Rogach, A. L. *Angewandte Chemie International Edition* **2004,** 43, (2), 148-149.
13. Chen, J.; Dong, A.; Cai, J.; Ye, X.; Kang, Y.; Kikkawa, J. M.; Murray, C. B. *Nano Letters* **2010,** 10, (12), 5103-5108.
14. Dong, A.; Chen, J.; Vora, P. M.; Kikkawa, J. M.; Murray, C. B. *Nature* **2010,** 466, (7305), 474-477.
15. Majumdar, A. *Science* **2004,** 303, (5659), 777-778.
16. Wang, R. Y.; Feser, J. P.; Lee, J.-S.; Talapin, D. V.; Segalman, R.; Majumdar, A. *Nano Letters* **2008,** 8, (8), 2283-2288.
17. Cheon, J.; Park, J.-I.; Choi, J.-s.; Jun, Y.-w.; Kim, S.; Kim, M. G.; Kim, Y.-M.; Kim, Y. J. *Proceedings of the National Academy of Sciences of the United States of America* **2006,** 103, (9), 3023-3027.
18. Talapin, D. V.; Shevchenko, E. V.; Kornowski, A.; Gaponik, N.; Haase, M.; Rogach, A. L.; Weller, H. *Advanced Materials* **2001,** 13, (24), 1868-1871.
19. Shevchenko, E.; Talapin, D.; Kornowski, A.; Wiekhorst, F.; Kötzler, J.; Haase, M.; Rogach, A.; Weller, H. *Advanced Materials* **2002,** 14, (4), 287-290.
20. Gaponenko, S. V., *Optical Properties of Semiconductor Nanocrystals*. Cambridge Universiry Press: 1998.
21. Gaponenko, S. V., *Introduction to Nanophotonics*. Cambridge University Press: 2010.
22. Koole, R.; Allan, G.; Delerue, C.; Meijerink, A.; Vanmaekelbergh, D.; Houtepen, A. J. *Small* **2008,** 4, (1), 127-133.
23. Allan, G.; Delerue, C. *Physical Review B* **2004,** 70, (24), 245321.
24. Bawendi, M. G.; Steigerwald, M. L.; Brus, L. E. *Annu. Rev. Phys. Chem.* **1990,** 41, 477-496.
25. Ball, D. W., *Physical Chemistry*. Thomson Brooks/Cole: 2003.
26. Atkins, P.; Paula, J. D., *Atkins' Physical Chemistry*. 8th edition ed.; 2006.
27. Alivisatos, A. P. *The Journal of Physical Chemistry* **1996,** 100, (31), 13226-13239.
28. Vanmaekelbergh, D. *Nano Today* **2011,** 6, (4), 419-437.
29. Frenkel, D. *Physica A* **1999,** 263, 26-38.
30. Gasser, U. *Journal of Physics: Condesed Matter* **2009,** 21, 203101-23125.
31. Filion, L. Self-assembly in colloidal hard-sphere systems. Utrecht University, Utrecht, 2011.
32. Hynninen, A. P.; Filion, L.; Dijkstra, M. *The Journal of Chemical Physics* **2009,** 131, (6), 064902-9.
33. Dijkstra, M.; van Roij, R.; Evans, R. *Physical Review E* **1999,** 59, (5), 5744-5771.
34. Trizac, E.; Eldrigde, M. D.; Madden, P. A. *Molecular Physics* **1997,** 90, (4), 675 - 678.
35. Eldridge, M. D.; Madden, P. A.; Pusey, P. N.; Bartlett, P. *Molecular Physics* **1995,** 84, (2), 395 - 420.

36. Eldridge, M. D.; Madden, P. A.; Frenkel, D. *Molecular Physics* **1993,** 79 (1), (105).
37. Kranendonk, W. G. T.; Frenkel, D. *Molecular Physics* **1991,** 72, (3), 715-733.
38. Shevchenko, E. V.; Talapin, D. V.; Murray, C. B.; O'Brien, S. *Journal of the American Chemical Society* **2006,** 128, (11), 3620-3637.
39. Talapin, D. V.; Shevchenko, E. V.; Murray, C. B.; Titov, A. V.; Kral, P. *Nano Letters* **2007,** 7, (5), 1213-1219.
40. Bodnarchuk, M. I.; Kovalenko, M. V.; Heiss, W.; Talapin, D. V. *Journal of the American Chemical Society* **2010,** 132, (34), 11967-11977.
41. Miszta, K.; de Graaf, J.; Bertoni, G.; Dorfs, D.; Brescia, R.; Marras, S.; Ceseracciu, L.; Cingolani, R.; van Roij, R.; Dijkstra, M.; Manna, L. *Nature Materials* **2011,** 10, (11), 872-876.
42. Rupich, S. M.; Talapin, D. V. *Nature Materials* **2011,** 10, (11), 815-816.
43. Titov, A. V.; KralÌ l, P. *Nano Letters* **2008,** 8, (11), 3605-3612.
44. Min, Y.; Akbulut, M.; Kristiansen, K.; Golan, Y.; Israelachvili, J. *Nat Mater* **2008,** 7, (7), 527-538.
45. Singh, A.; Gunning, R. D.; Ahmed, S.; Barrett, C. A.; English, N. J.; Garate, J.-A.; Ryan, K. M. *Journal of Materials Chemistry* **2012,** 22, (4), 1562-1569.
46. Pietra, F.; Rabouw, F. T.; Evers, W. H.; Byelov, D. V.; Petukhov, A. V.; Donegá, C. d. M.; Vanmaekelbergh, D. *Submitted to Nanoletters* **2012**.
47. Schliehe, C.; Juarez, B. H.; Pelletier, M.; Jander, S.; Greshnykh, D.; Nagel, M.; Meyer, A.; Foerster, S.; Kornowski, A.; Klinke, C.; Weller, H. *Science* **2010,** 329, (5991), 550-553.
48. Cho, K.-S.; Talapin, D. V.; Gaschler, W.; Murray, C. B. *Journal of the American Chemical Society* **2005,** 127, (19), 7140-7147.
49. Koh, W.-k.; Bartnik, A. C.; Wise, F. W.; Murray, C. B. *Journal of the American Chemical Society* **2010,** 132, (11), 3909-3913.
50. Chen, J. S.; Zhu, T.; Li, C. M.; Lou, X. W. *Angewandte Chemie* **2011,** 123, (3), 676-679.
51. Mallavajula, R. K.; Archer, L. A. *Angewandte Chemie International Edition* **2011,** 50, (3), 578-580.

Chapter 2

Entropy-driven formation of binary semiconductor-nanocrystal superlattices

One of the main reasons for the current interest in colloidal nanocrystals is their propensity to form superlattices, systems in which (different) nanocrystals are in close contact in a well-ordered 3-D geometry resulting in novel material properties. However, the principles underlying the formation of binary nanocrystal superlattices are not well understood. In this chapter, we present a study of the driving forces for the formation of binary nanocrystal superlattices by comparing the formed structures with full free energy calculations. Self-assembly is induced by evaporation of the solvent. The nature (metallic or semiconducting) and the size-ratio of the two nanocrystals are varied systematically. With semiconductor nanocrystals, self-organization at high temperature leads to superlattices (AlB_2, $NaZn_{13}$, $MgZn_2$) in accordance with the phase diagrams for binary hard-sphere mixtures; hence entropy increase is the dominant driving force. A slight change of the conditions results in structures that are energetically stabilized. This is also the case when self-assembly is induced by addition of a non-solvent. This study provides rules for the rational design of 3-D nanostructured binary semiconductors, materials with promises in thermoelectrics and photovoltaics and which cannot be reached by any other technology.

2.1 Introduction

Colloidal, monolayer-stabilized nanocrystals (NC) can be synthesized with a nearly spherical shape and with a well-defined diameter that does not vary by more than 5% in the sample. Due to their monodisperse size and shape, such NCs show a strong propensity to assemble into NC superlattices.[1] More than a decade ago, the formation of single-component superlattices that consist of CdSe semiconductor NCs was reported.[1] This was followed by the demonstration of binary superlattices, consisting of NCs of different diameters and different nature, i.e. semiconductor, metallic or magnetic.[1-13] In such systems, novel collective properties can arise from the (quantum mechanical) interactions between the different components that are in close contact in a 3-D ordered geometry. Some striking examples have already been reported.[4, 14-16] For instance, a binary superlattice of two types of insulator nanoparticles is found to become conductive due to inter-particle charge transfer.[3] Colloidal crystallization is the only method known to date to obtain nanostructured systems, with order in 3 dimensions. However, for further progress in the field of designed nanostructured materials, improved control of nanocolloid crystallization is a key factor.

Apart from the viewpoint of emerging nanomaterials, the formation of (binary) NC superlattices is of strong interest in colloidal science. Nanocrystals have a mass that is about a million times smaller than that of the colloidal particles commonly used in crystallization studies; hence, their thermal velocity is about a factor of thousand higher. This agrees with the fact that nanocolloid crystallization is a relatively fast process, still occurring under (near) equilibrium conditions. While crystallization of micron-sized colloids takes days to months[17], NC superlattices are formed within a few minutes. Fast and reversible crystallization should allow one to study the thermodynamics of NC superlattice formation in a broad parameter range. Although a plethora of NC superlattices have been reported, the principles underlying their formation have not been studied systematically. For instance, attractions as well as entropic factors have been proposed as the driving force behind the formation of binary superlattices[10] but clear rules have not been presented.

In the case of micrometer-sized colloids, the interactions between the particles can be tailored and systems are available that resemble hard spheres.[17-22] It has been shown that the crystallization of a binary mixture of micrometer-sized colloidal hard spheres is driven only by an increase in entropy.[17, 20, 22] In the case of monolayer-stabilized NCs in a good organic solvent, the effective interaction consists to a first approximation of Van der Waals attraction between the cores and steric repulsion between the stabilizing ligand molecules. The Van der Waals attraction between two *semiconductor* nanocrystals is weak due to the large center-to-center distance between the NC cores, and is almost completely screened by the steric repulsion (see appendix 2.1). Hence, semiconductor nanocrystals in a good solvent may have an interaction potential resembling that of hard spheres. In contrast, when

metal nanocrystals are involved, the Van der Waals attractions are stronger and the pair potential exceeds the thermal energy considerably (Appendix 2.1).

Here, we present a systematic study of the thermodynamic driving force behind the formation of binary nanocrystal superlattices by comparing the crystal structures formed with phase diagrams obtained for binary mixtures of hard spheres, the free energy being calculated with the Frenkel-Ladd Einstein integration method in computer simulations (see appendix 2.1). We have combined two different semiconductor NCs (i.e. PbSe and CdSe NC), as well as a semiconductor NC (PbSe) with metallic gold NCs. We have studied superlattice formation induced by the evaporation of the solvent, i.e. by increasing the particle concentration at a controlled and variable temperature. Secondly, crystallization was initiated by increasing the interaction between the particles by addition of a non-solvent. The NC size ratio and, in several cases, also the relative particle concentration (composition) in the binary suspensions were varied systematically. Solvent evaporation from mixtures of semiconductor NCs results in superlattices that agree to a large extent with the theoretical phase diagrams of binary hard-sphere mixtures, provided that the temperature is sufficiently high. This is in contrast with the formation of superlattices i) at lower temperature, ii) when metallic nanocrystals are involved, or iii) when a non-solvent is added to increase the interactions. In all these cases, superlattices that are known to be unstable for binary hard-sphere mixtures are formed, implying that Van der Waals attractions become important.

2.2 Experimental

2.2.1 Nanocrystal synthesis

PbSe NCs were synthesized by a method described by Houtepen et al.[23] The synthesis was performed in a water and oxygen free environment. (1) 1.9 gram of lead acetate tri hydrate (99.999% Aldrich), 4 mL of diphenyl ether (99% DPE, aldrich), 3 mL of oleic acid (OA, 90% Aldrich) and 16 mL trioctyl phospine (TOP, 90% Fluka) were heated to 100 °C under low pressure (10-3 bar) for ~3 hours. (2) A second mixture containg 0.31 g Se (99.999% Alfa Aesar) and 4 mL TOP was prepared. Subsequently 11.5 mL of solution (1) and 1.7 ml of solution (2) was injected into 10 mL 190 °C DPE. The reaction mixture was kept at a constant temperature of 145 °C. After 30 seconds to 10 minutes the reaction mixture was quenched with 20 mL butanol and 10 mL methanol. The crude synthesis mixtures were washed twice by precipitating with methanol, centrifugation and redispersion of the sediment in toluene.

CdSe NCs were synthesized by a method described by de Mello Donega et al.[24] The synthesis was performed in a water and oxygen free environment. 0.79 gram of Selenium

(99.999% Alfa Aesar), 0.28 g of dimethylcadmium (99.99% ARC Technologies) and 10 mL of TOP (96% Aldrich) was prepared. The solution was injected into a mixture of 20 gram dried trioctylphospineoxide (TOPO, 99% Aldrich) and 10 g hexadecylamine (HDA) at a temperature of ~300 °C, resulting in a temperature drop to ~170 °C. The temperature was raised and stabilized to the desired growth temperature of 240 °C for 30 minutes, resulting in nanocrystals with a diameter of approximately 3 nm. The synthesis mixtures were washed twice by precipitating with methanol, centrifugation and redispersion of the sediment in toluene.

Au NCs were synthesized by a method described by Brust et al.[25] The synthesis was performed at room temperature in ambient environment. (1) 0.27 g of $HAuCl_4$ (99.9%, Aldrich) was desolved in 22.29 g ultra pure water. (2) A second mixture of 1.90 g of tetraoctylammonium bromide (TOAB, 98%, Aldrich) dissolved in 60 g toluene (99.8%, Aldrich). 5.3 mL of (1) and 14.8 g of (2) were mixed and stirred vigorously. A third stock solution (3) was prepared by adding 0.076 g of Sodium borohydride (98%, Aldrich) to 4.86 g of ultra pure water. Subsequently (3) was rapidly injected in the mixture of (1) and (2). The solution was stirred for ~18 hours and afterwards 75 µL of 1-dodecanethiol (≥97%, Fluka) was added to the mixture. The sample was washed twice by precipitating with ethanol, centrifugation and redispersion of the sediment in toluene.

2.2.2 Self-assembly process

By solvent evaporation:
Superlattice formation was achieved by mixing two colloidal suspensions with known concentrations. Either PbSe and CdSe or PbSe and Au NC suspensions were used dissolved in Tetra ChloroEthylene (TCE). The concentration ratio, both relative and total, and temperature were varied. Colloidal crystallization was achieved on a TEM grid that makes an angle of 30 degrees with the suspension surface (Figure 2.1), the solvent was evaporated at enhanced temperature of 70 °C and under reduced pressure (~10 mbar).[26]

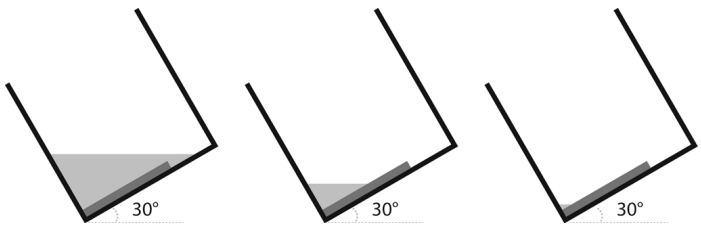

Figure 2.1: Schematic representation of the self-assembly process. From left to right: a sample, usually a TEM grid, is placed in a suspension containing nanocrystals. The sample is positioned to make an angle of 30° with the surface of the solution. The solvent is evaporated under reduced pressure (~10 mbar) and enhanced temperature (70 °C).

By addition of non-solvent:
The non-solvent method was based on a procedure described by Talapin *et al.* in 2001 with which they obtained mono-component superlattices of CdSe and FePt NCs.[27] Superlattice formation was achieved by placing a suspension containing nanocrystals in a vial, hereafter the non-solvent, i.e. a solvent in which the nanocrystals have limited stability, was carefully added to the dispersion and placed on a heating plate. Alternative no heating of the suspension was used and the sample was left undisturbed for several days.

2.3 Results and discussion

We have studied the formation of superlattices starting from binary mixtures of PbSe and CdSe NCs, or PbSe and gold NCs. The effective diameter of the NCs was obtained from the center-to-center distance in TEM pictures of single-component hexagonal monolayers. While we label our single-component lattices face-centred-cubid (fcc), from our experimental data we cannot distinguish between fcc, hcp and random stackings of hexagonal planes. In the first case, the effective diameter of the PbSe NCs was varied between 7 and 11 nm, while that of the CdSe NCs was 5.8 nm; hence, the size ratio γ ranged from 0.53 to 0.83. In binary mixtures of PbSe and Au NCs, γ varied between 0.47 and 0.86. The size dispersion in the original suspensions was $\leq 5\%$ for the PbSe and CdSe suspensions and about 10 % for the Au NC suspensions. Nanocolloid crystallization by solvent evaporation was achieved under controlled pressure (~10 mbar) and temperature ($20\ ^\circ C \leq T \leq 70\ ^\circ C$). The TEM substrate was tilted over an angle of 30 degrees with respect to the liquid/air interface. Previous studies have shown that crystal nucleation occurs at the organic liquid/air interface.[9] Generally, colloidal crystallization leads to a polycrystalline thin-film solid, with single-crystal domains between 1 and 10 μm in size. Examples are presented in Figure 2.2 and Figure 2.4, and in the Appendix. We have analysed the crystal structures that are present on the TEM grids and measured the relative surface area that they occupy on the grid. In several cases the relative fraction of a given crystal structure depends on the particle concentration ratio in the binary suspension. Addition of a non-solvent which increases the Van der Waals attractions leads to the formation of 3-D single-component superlattices that we collected by dipping a TEM grid in the suspension.

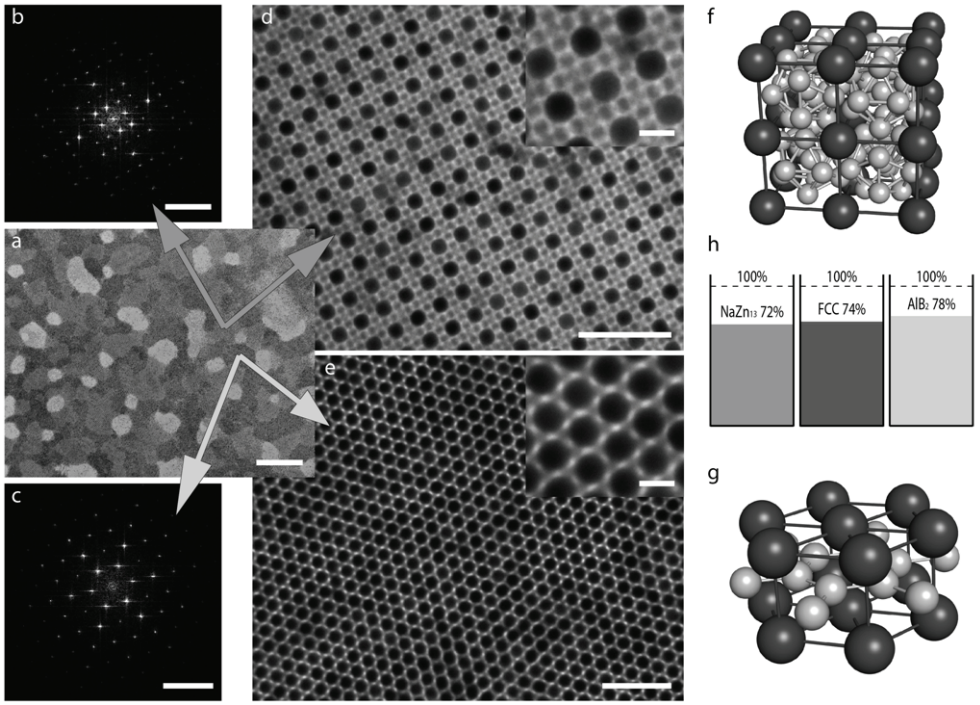

Figure 2.2: Binary superlattices obtained by solvent evaporation at 70 °C from a suspension of PbSe nanocrystals (11 nm effective diameter) and CdSe nanocrystals (5.8 nm effective diameter) at a size ratio γ of 0.53 and particle concentration ratio of about 4. (a) Overview of the TEM grid with different domains; (b,d,f) Fourier transform, TEM projection, and unit cell of a part of a $PbSe(CdSe)_{13}$ domain; (c,e,g) Fourier transform, TEM projection, and unit cell of part of a $PbSe(CdSe)_2$ domain; (h) filling fractions of the observed binary lattices with respect to the fcc lattice. The scale bars are 500 nm for panel a, 0.25 nm^{-1} for panels b and c, 50 nm for panels d and e, and 10 nm for the insets of panel d and e.

Phase diagrams for binary hard-sphere mixtures.

The self-assembled crystal structures on the TEM grids are compared with the phase diagrams as determined from free energy calculations using the Frenkel-Ladd Einstein thermodynamic integration in computer simulations for binary mixtures of hard spheres[18-21]. Using this method, the free-energy can be determined exactly and accounts for all entropic contributions. This theoretical work was performed by Dr. L. Fillion, working in the group of Prof. M. Dijkstra, Soft Condensed Matter, Utrecht. From the available theoretical predictions the following conclusions can be drawn (Table 1.1): apart from the single-component fcc phases, for $0.414 \leq \gamma \leq 0.45$, NaCl is stable[18]; for $0.45 \leq \gamma \leq 0.61$, AlB_2 is stable[18-20]; for $0.54 \leq \gamma \leq 0.625$, $NaZn_{13}$ is stable[19, 20]; and for $0.76 \leq \gamma \leq 0.84$ it was recently established that the Laves phases ($MgZn_2$, $MgCu_2$, $MgNi_2$) are stable[21], although their maximum filling fraction is lower than that of the fcc lattice. Note that between $0.63 \leq \gamma \leq 0.75$ there are no known stable binary hard-sphere crystal structures.

2.3.1 Binary crystal structures formed by solvent evaporation

The results obtained with the method of solvent evaporation are summarised in Table 2.1 (combinations of PbSe and CdSe semiconductor NCs) and Table 2.2 (combinations of PbSe and Au NCs). For convenience, the results obtained with the solvent evaporation method will be presented here in order of increasing size ratio γ and according to the theoretically predicted stability regions for binary hard-sphere crystal structures.

size ratio (effective)	Diameter NC (nm)		Crystal structure	2D surface coverage (%)
	Large	*Small*		
0.53	11.0 (PbSe)	5.8 (CdSe)	AlB_2	60
			$NaZn_{13}$	1
			Single component	10
0.56	10.3 (PbSe)	5.8 (CdSe)	AlB_2	10
			$NaZn_{13}$	60
			Single component	10-20
0.59	9.8 (PbSe)	5.8 (CdSe)	AlB_2	<1
			Single component	10-50
0.6	9.61 (PbSe)	5.8 (CdSe)	AlB_2	<1
			$NaZn_{13}$	<1
			unknown	<1
			Single component	10-80
0.62	9.43 (PbSe)	5.8 (CdSe)	AlB_2	<1
			$NaZn_{13}$	<1
			unknown	<1
			Single component	20-60
0.65	8.88 (PbSe)	5.8 (CdSe)	$MgZn_2$	<1
			$CaCu_5$	<1
			Single component	
0.72	8.09 (PbSe)	5.8 (CdSe)	$MgZn_2$	<1
			Single component	>50
0.73	8.0 (PbSe)	5.8 (CdSe)	$MgZn_2$	25
			$CaCu_5$	1
			Single component	40-60
0.75 T=70°C	7.76 (PbSe)	5.8 (CdSe)	$MgZn_2$	10-15
			CsCl	<1-5
			Single component	20-50
0.75 T=20°C	7.76 (PbSe)	5.8 (CdSe)	$MgZn_2$	<1-7
			CsCl	10-15
			Single component	20-40
0.79	7.37 (PbSe)	5.8 (CdSe)	$MgZn_2$	<1
			$CaCu_5$	<1
			Single component	20-80
0.8	7.23 (PbSe)	5.8 (CdSe)	$MgZn_2$	<1
			$CaCu_5$	<1
			Single component	30-80

Table 2.1: Overview of the superlattices obtained by solvent evaporation from binary suspensions of semiconductor nanocrystals, i.e. combinations of PbSe NC and CdSe NC with varying size ratio $\gamma=\sigma_S/\sigma_L$, where $\sigma_{S(L)}$ is the diameter of the small (large) particles. Solvent evaporation was performed at 70 °C (unless otherwise stated). The relative importances of the different structures that are formed are expressed in percentage surface coverage.

size ratio (effective)	Diameter NC (nm)		Crystal structure	2D surface coverage (%)
	Large	*Small*		
0.47	11.0 (PbSe)	5.2 (Au)	NaCl	1-5
			CuAu	<1
			Cu_3Au	<1
			$CaCu_5$	<1
			Single component	10-50
0.53	9.8 (PbSe)	5.2 (Au)	CuAu	<1
			Single component	10-20
0.55	9.49 (PbSe)	5.2 (Au)	CuAu	<1
			Single component	10-20
0.57	9.8 (PbSe)	5.58 (Au)	$NaZn_{13}$	<1
			Single component	1-20
0.59	11.0 (PbSe)	6.59 (Au)	AlB_2	<1
			Single component	10-50
0.61	9.49 (PbSe)	5.8 (Au)	AlB_2	<1
			Single component	10-50
0.64	9.8 (PbSe)	6.29 (Au)	CuAu	1-5
			Single component	30-50
0.68	11.0 (PbSe)	7.51 (Au)	AlB_2	<1
			Single component	10-50
0.74	6.98 (PbSe)	5.2 (Au)	CsCl	20-30
			Single component	10-30
0.83	6.98 (PbSe)	5.8 (Au)	CsCl	1-10
			$CaCu_5$	1-5
			Single component	10-50
0.86	8.1 (Au)	6.98 (PbSe)	CsCl	<1
			Single component	30-50

Table 2.2: Overview of the superlattices obtained by solvent evaporation from binary suspensions of semiconductor nanocrystals with gold NCs with varying size ratio $\gamma=\sigma_S/\sigma_L$. Solvent evaporation was performed at 70 °C. The relative importances of the different structures that are formed are expressed in percentage surface coverage.

In the range $0.45 < \gamma < 0.54$, we have performed several experiments. Combining the large PbSe and smaller Au NCs (Table 2.2), we observed mostly single-component lattices of PbSe and Au NCs. Binary lattices covering small fractions (about 1 %) of the TEM grid were observed occasionally. In contrast, solvent evaporation from a binary suspension of two semiconductor NCs, i.e. large PbSe and smaller CdSe NCs ($\gamma = 0.53$) at 70 °C leads to superlattice films that contain $PbSe(CdSe)_2$ structures and the single-component fcc phases. The $PbSe(CdSe)_2$ superlattice is iso-structural with AlB_2. Upon changing the particle concentration ratio of PbSe and CdSe NCs in the suspension, we found that the AlB_2 phases reach a maximum surface coverage of about 60 % at a particle number concentration ratio of 10, this happens at the cost of the single-component phases (see Figure 2.3). We remark that the binary $PbSe(CdSe)_{13}$ crystal structure is also observed, however with a low surface coverage that does not increase with increasing the particle concentration of the small CdSe NCs with respect to that of the large PbSe NCs, even up to a factor of 20. This provides strong evidence that at $\gamma = 0.53$ and high T (70 °C) the $PbSe(CdSe)_2$ AlB_2 structure is the only stable binary superlattice structure coexisting with the single-component crystal structures. This result is in accordance with the theoretical phase diagram of binary hard-sphere mixtures.

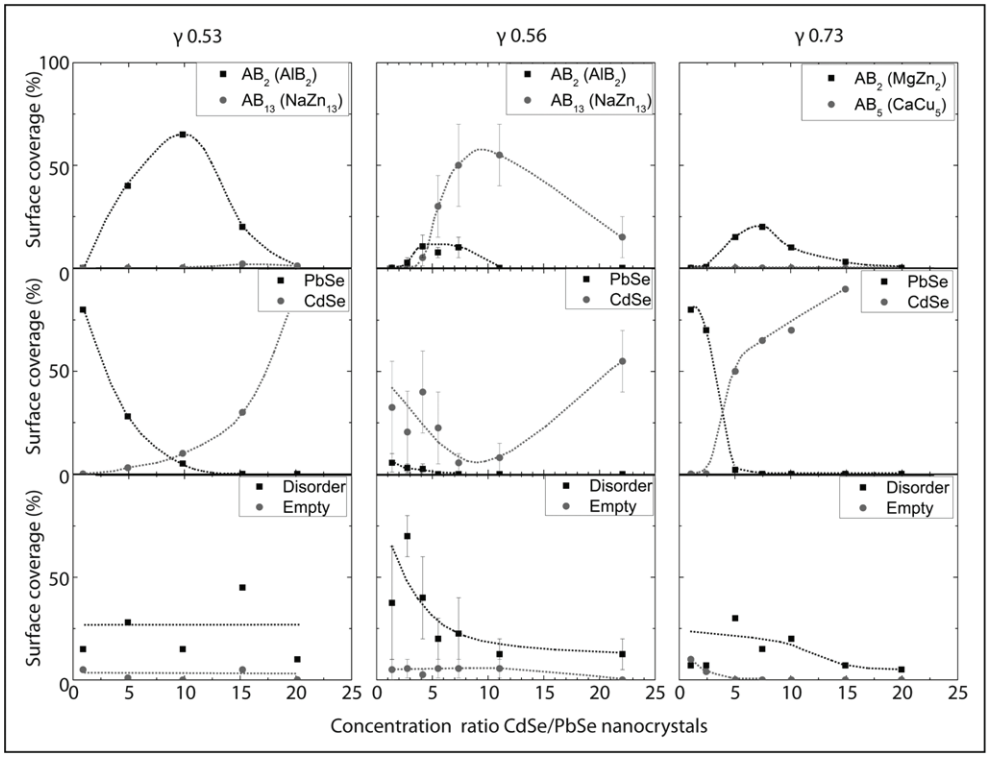

Figure 2.3: The effect of changing the particle concentration in the binary mixtures on the relative importance of the formed single-component and binary NC superlattices. The size ratio of the large PbSe NCs with respect to the small CdSe NCs is γ=0.53 (left panels), γ= 0.56 (center panels), γ=0.73 (right panels). The dotted lines represent guides to the eye. The size ratio of 0.56 is from former published work.[11] The uncertainty on the percentage of surface coverage is about 25 relative %.

In the second size ratio range $0.54 \leq \gamma \leq 0.61$, the theoretical phase diagrams of binary hard-sphere mixtures predict that the binary crystal structures AlB_2 and $NaZn_{13}$ are both stable.[18-20] Note that the latter is only stable at sufficiently high particle number ratio of small to large hard spheres. Solvent evaporation at high temperature (70 °C) from suspensions that combine large PbSe and small CdSe semiconductor NCs with size ratio $\gamma = 0.56$ results in NC films that show four different superlattices: the two fcc lattices, and the binary $PbSe(CdSe)_2$ AlB_2 and $PbSe(CdSe)_{13}$ $NaZn_{13}$ superlattices (Figure 2.2). Electron tomography has shown that the $PbSe(CdSe)_{13}$ superlattices are genuine icosahedral $NaZn_{13}$ structures[9] (see also chapter 4). The effect of changing the particle number ratio is shown in Figure 2.3. At a particle number ratio CdSe NC/PbSe NC below 4, the $PbSe(CdSe)_2$ AlB_2 structure is the most important binary crystal structure, reaching a maximum coverage at a particle number ratio of about 5. Further increase of the concentration of the small CdSe NCs results in an increasing importance of the $PbSe(CdSe)_{13}$ superlattice, reaching a maximum coverage of about 55 % on the TEM grid. At a size ratio $\gamma = 0.59$, there are still $PbSe(CdSe)_2$ AlB_2 domains present, but $PbSe(CdSe)_{13}$ $NaZn_{13}$ is the dominant binary NC superlattice for solvent evaporation at 70 and 20 °C. These results show that for mixtures of

two semiconductor nanocrystals, AlB_2 and $NaZn_{13}$ are the stable binary crystal structures for size ratios $0.54 \leq \gamma \leq 0.61$, in agreement with the theoretical predictions for binary hard-sphere mixtures.[18-20] In contrast, solvent evaporation from binary suspensions that combine semiconductor PbSe NCs with metallic Au NCs results predominantly in single-component fcc lattices. Several binary crystal structures were observed, though with a minute coverage (≤ 1%). The absence of substantial amounts of AlB_2 and $NaZn_{13}$ structures provides evidence that with metallic NCs entropy is not the only driving force in the formation of superlattices.

In the third range, $0.64 \leq \gamma \leq 0.75$, the theoretical phase diagrams of binary hard-sphere mixtures show no stable binary structures. Solvent evaporation at 70 °C of suspensions that contain large PbSe and smaller CdSe NCs ($\gamma = 0.65$ and 0.72) shows nanocrystal films that contain predominantly single-component lattices. Minute fractions of binary NC superlattices that contain $CaCu_5$ and $MgZn_2$ are also observed. Free-energy calculations of the Gibbs free energy of $CaCu_5$ were performed at a size ratio range of 0.64-0.70 as the highest packing fraction lies within this range and were compared to the Gibbs free energy of the fcc phase. It was found that the phase separated fcc phase has a lower Gibbs free energy than that of the $CaCu_5$ structure, indicating that $CaCu_5$ is not thermodynamically stable for binary hard-sphere mixtures. At $\gamma = 0.73$, however, the $MgZn_2$ becomes the dominant binary crystal structure, coexisting with the single-component fcc lattice and a minute fraction of $CaCu_5$. If the concentration of the small CdSe NCs is increased with respect to that of the larger PbSe NCs, the $MgZn_2$ phase reaches a maximum surface coverage of 25 % at around a particle concentration ratio CdSe NC/PbSe NC of 7. When the relative concentration of the smaller CdSe particles is increased further, the single-component CdSe superlattice becomes dominant. Strikingly, the $PbSe(CdSe)_5$ superlattice ($CaCu_5$) is only marginally present in the entire range of relative particle concentration, showing that this phase is very likely not thermodynamically stable. We conclude that $PbSe(CdSe)_2$ ($MgZn_2$) is a thermodynamically stable phase at $\gamma = 0.73$, hence at a size-ratio slightly smaller than predicted by simulations ($\gamma = 0.76$).[21] The same conclusion holds for a size ratio γ of 0.75. Using this combination of PbSe and CdSe NCs, we have also performed solvent evaporation experiments at temperatures below 70 °C. In Figure 2.4, typical overviews of the nanocrystal films formed at 70 °C and 20 °C are presented. At 70 °C, 95 % of the binary structures consists of $PbSe(CdSe)_2$ ($MgZn_2$), with a minor fraction (5%) of PbSe(CdSe), isostructural with cubic CsCl. Solvent evaporation at 20 °C, however, leads to a reduction of the $MgZn_2$ fraction (50 -1 % of the binary crystals, depending on the sample) and an increase of the CsCl structure (50 – 99 % of the binary crystals). These results show that reducing the temperature leads to new structures that are not stable in the theoretical phase diagrams of binary hard-sphere mixtures. Hence, energetic interactions between the nanocrystals become important when the temperature is lowered.

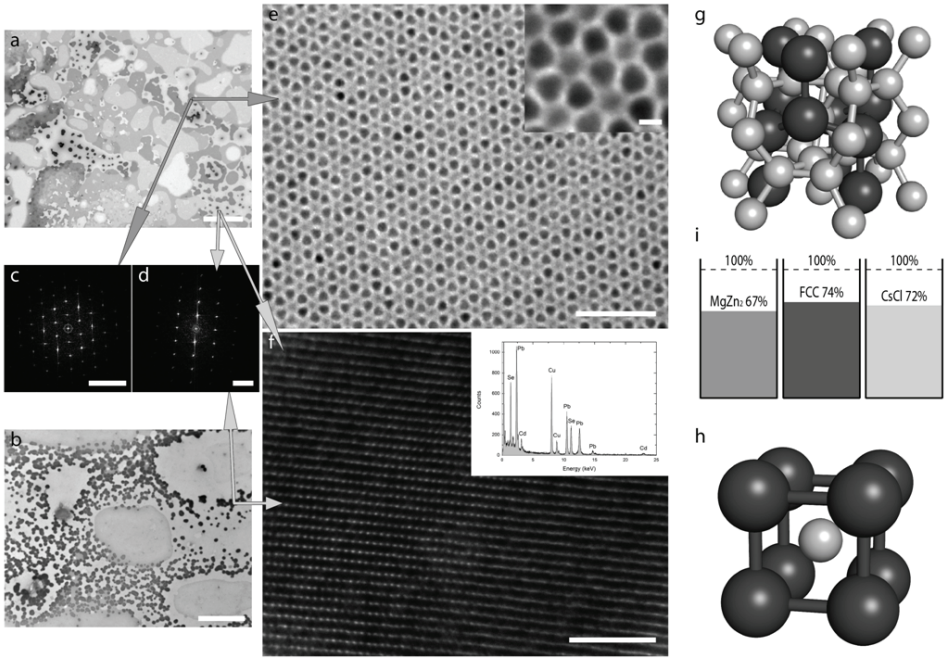

Figure 2.4: Binary superlattices formed from a suspension of large PbSe nanocrystals (7.76 nm effective diameter) and smaller CdSe nanocrystals (5.8 nm effective diameter) by solvent evaporation at 70 and 20 °C; the particle size ratio γ is 0.75, and the particle concentration ratio is 2. (a, b) Overview of the structures observed on the TEM grid after solvent evaporation at 70 and 20 °C, respectively. (c, e, g) Fourier transform, TEM projection, and unit cell of the PbSe(CdSe)$_2$ lattice isostructural with$MgZn_2$. (d,f,h) Fourier transform, TEM projection, and unit cell of the PbSe(CdSe) lattice isostructural with CsCl; the insert of f shows the results of EDX elemental analysis providing evidence for a binary structure of PbSe and CdSe nanocrystals. The scale bars for panels a and b are 5 μm, panels c and d are 0.25 nm^{-1}, panels e and f are 50 nm, and 5 nm for the inset of panel e.

Recent theoretical work has shown the Laves phases ($MgZn_2$, $MgCu_2$, $MgNi_2$,) to be stable in the size ratio range $0.76 \leq \gamma \leq 0.84$.[21] In accordance with this prediction, the combination of PbSe and CdSe NCs at $\gamma = 0.79$ and $\gamma = 0.80$ leads to PbSe(CdSe)$_2$ superlattices with a $MgZn_2$ structure. However, this binary crystal structure constitutes only a small fraction of the NC film that consists mainly of single-component lattices. Apart for the $MgZn_2$ structure, the other Laves phases were not observed. Indeed, a finite-size scaling analysis shows that the free-energy difference between the three Laves structures is small, but that $MgZn_2$ has the lowest free energy in the thermodynamic limit.[21] In accordance with this, using a combination of CdTe and CdSe NCs, Chen et al. observed the $MgZn_2$ phase at $\gamma = 0.81$.[8] We remark that with mixtures of micron-sized hard spheres, Laves phases have not been observed yet. The combination of metallic Au NCs with PbSe NCs results in NC films with a significant contribution of CsCl (up to 30 %), in coexistence with the single-component phase (Figure 2.5). Free energy simulations show that this structure can only be stabilized if inter-particle interactions are incorporated.

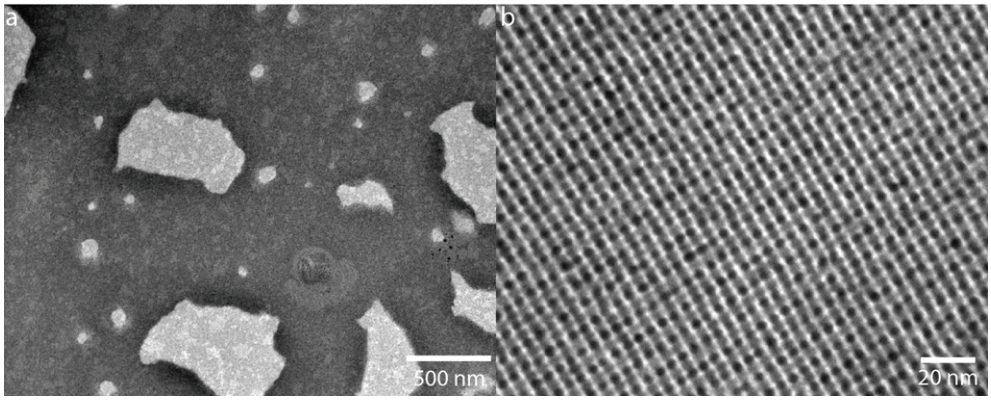

Figure 2.5: Binary and single-component superlattices obtained from a suspension of PbSe nanocrystals (7.0 nm effective diameter) and Au nanocrystals (5.2 nm effective diameter) at a size ratio γ=0.74. (a) overview of the TEM grid with single component domains of PbSe and Au NCs, binary domains PbSe(Au), iso-structural with CsCl. (b) detailed TEM grid showing a binary PbSe(Au) superlattice with CsCl structure.

2.3.2 Colloidal crystallization by addition of a non-solvent

Adding a non-solvent leads to increased Van der Waals attractions between the NCs, inducing colloidal crystallization even at low particle concentration. We have studied the crystal structures that were formed in binary mixtures of large PbSe and small CdSe NCs, and large PbSe and small Au NCs in hexane to which butanol was added as a non-solvent. The experiments were performed in a broad size ratio range $0.53 \leq \gamma \leq 0.98$. Binary crystal structures were never observed. Instead, 3-D colloidal crystals consisting exclusively of the larger NCs were formed as confirmed by TEM-EDX analysis (see Figure 2.6).

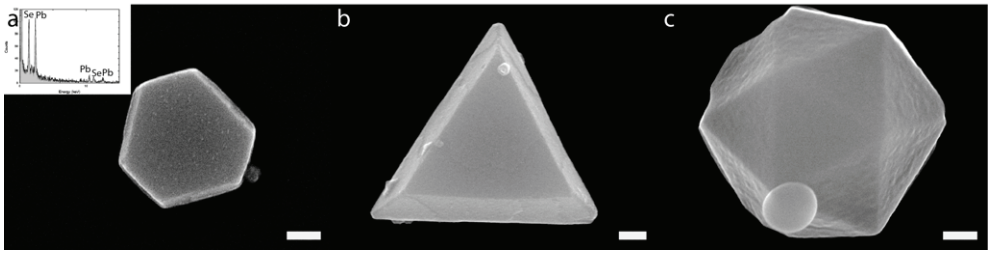

Figure 2.6: Crystals obtained due to addition of a non-solvent to a binary suspension consisting of large Pbse NCs and smaller CdSe or Au NCs. The size ratio γ was varied between 0.53 and 0.98. Only single-component superlattices consisting of the larger PbSe NCs were observed. Different crystal shapes are found: (a) hexagonal platelet, (b) triangular platelet, (c) icosahedrons. In the inset of (a), an EDX spectrum is given, indicating the presence of PbSe NCs only.

2.3.3 Discussion

A summary of the observed crystal structures compared with the theoretical results for binary hard-sphere mixtures is presented in Figure 2.7. The binary NC superlattice structures $PbSe(CdSe)_2$ iso-structural with AlB_2, $PbSe(CdSe)_{13}$ iso-structural with $NaZn_{13}$ and $PbSe(CdSe)_2$ iso-structural with $MgZn_2$ obtained from binary mixtures of organically-capped semiconductor NCs in a good solvent at sufficiently high temperature are as expected on the basis of binary hard-sphere phase diagrams. Similar results were obtained by Chen *et al.*, who combined CdTe and CdSe NCs.[8, 10] Unlike the latter, we have also investigated the effect of changing the particle concentration ratio in the suspension. We find that, for each of the three stable binary structures, the relative importance in the film depends on the composition of the initial suspension. For instance at $\gamma = 0.53$, the importance of the stable $PbSe(CdSe)_2$ structure increases to a maximum at a particle concentration ratio CdSe/PbSe of 10, this happens at the expense of the PbSe fcc structure. At higher CdSe/PbSe ratios, the importance of the binary structure decreases, and the fcc CdSe lattice becomes the dominant structure. Such a correlation between the composition of the suspension and the stoichiometry of the film forms a landmark for true equilibrium structures. Combining two types of semiconductor NCs at high temperature, we did not observe any dominant crystal structure that is in flagrant disagreement with the theoretical predictions for binary hard-sphere mixtures. It should be realized that the contribution due to the Van der Waals interactions (see appendix 2.1) between the NCs can become important to the free-energy when the conditions for self-organization are slightly changed. For instance, while at 70 °C the combination of PbSe and CdSe NCs leads to the formation of the $MgZn_2$ binary superlattice in agreement with the hard-sphere phase diagrams, lowering of the temperature leads to a gradual increase of the CsCl structure that is not stable for binary hard-sphere mixtures. Second, when one of the particles is metallic, the Van der Waals attractions are increased, and several binary crystal structures are observed that can only be stabilized by energetic interactions (see Figure 2.7, PbSe and Au NCs). In line with this, we also found that a gradual increase of the interactions between the nanocrystals induced by adding a non-solvent leads solely to single-component crystal structures.

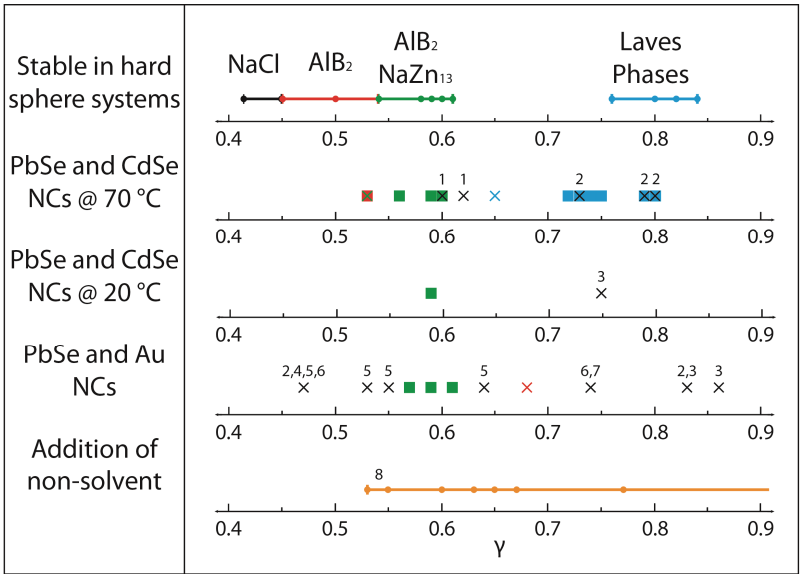

Figure 2.7: Schematic comparison of the structures that are experimentally observed with the theoretical phase diagrams for binary hard-sphere mixtures. Squares indicate crystal structures that are in agreement with the hard-sphere model. Crosses indicate crystal structures that are in disagreement with the hard-sphere model: (1) refers to several unknown crystal structures (Appendix 2.2), coverage <1%; (2) $PbSe(CdSe)_5$ isostructural with CaCu5, coverage <1%, the coverage does not respond to a change in the composition; (3) CsCl structure; (4) NaCl structure; (5) CuAu structure; (6) Cu_3Au structure (appendix 2.3 for examples of the structures).The crystal structures (1-6) have a low (~1%) surface coverage. The number 7 indicates the CsCl structure, observed here with a surface coverage of about 30%. Number 8 is for the addition of non-solvent for which only single component structures are observed.

2.4 Conclusion

Our work shows that under certain conditions, i.e. two types of semiconductor NCs in a good solvent at high temperature, the formation of binary nanocrystal superlattices is driven by an increase in entropy. When these conditions are not fulfilled, interactions must be taken into account to understand the resulting superlattices. Our findings are of importance for the design of novel 3-D nanostructured materials from the huge variety of nanocolloids now available. It is clear that if colloidal crystallization is driven solely by entropy, the resulting binary superlattice structures are determined only by the size-ratio of the nanocrystals and the relative particle concentrations in the suspension. This simplicity opens avenues to the rational design of two-component nanostructured semiconductors. These systems hold promise for novel types of miniaturized transistors, thermo-electric materials and photovoltaics.

References

1. Murray, C. B.; Kagan, C. R.; Bawendi, M. G. *Science* **1995,** 270, (5240), 1335.
2. Rogach, A. L.; Talapin, D. V.; Shevchenko, E. V.; Kornowski, A.; Haase, M.; Weller, H. *Advanced Functional Materials* **2002,** 12, (10), 653.
3. Urban, J. J.; Talapin, D. V.; Shevchenko, E. V.; Kagan, C. R.; Murray, C. B. *Nat Mater* **2007,** 6, (2), 115.
4. Heath, J. R. *Nature* **2007,** 445, (7127), 492.
5. Kiely, C. J.; Fink, J.; Brust, M.; Bethell, D.; Schiffrin, D. J. *Nature* **1998,** 396, (6710), 444.
6. Shevchenko, E. V.; Talapin, D. V.; Kotov, N. A.; O'Brien, S.; Murray, C. B. *Nature* **2006,** 439, (7072), 55.
7. Redl, F. X.; Cho, K. S.; Murray, C. B.; O'Brien, S. *Nature* **2003,** 423, (6943), 968.
8. Chen, Z.; Moore, J.; Radtke, G.; Sirringhaus, H.; O'Brien, S. *Journal of the American Chemical Society* **2007,** 129, (50), 15702.
9. Friedrich, H.; Gommes, C. J.; Overgaag, K.; Meeldijk, J. D.; Evers, W. H.; Nijs, B. d.; Boneschanscher, M. P.; de Jongh, P. E.; Verkleij, A. J.; de Jong, K. P.; van Blaaderen, A.; Vanmaekelbergh, D. *Nano Letters* **2009,** 9, (7), 2719.
10. Chen, Z.; O'Brien, S. *ACS Nano* **2008,** 2, (6), 1219.
11. Overgaag, K.; Evers, W.; de Nijs, B.; Koole, R.; Meeldijk, J.; Vanmaekelbergh, D. *Journal of the American Chemical Society* **2008,** 130, (25), 7833.
12. Shevchenko, E. V.; Talapin, D. V.; O'Brien, S.; Murray, C. B. *Journal of the American Chemical Society* **2005,** 127, (24), 8741.
13. Rogach, A. L. *Angewandte Chemie International Edition* **2004,** 43, (2), 148.
14. Urban, J. J.; Talapin, D. V.; Shevchenko, E. V.; Kagan, C. R.; Murray, C. B. *Nature materials* **2007,** 6, (2), 115.
15. Majumdar, A. *Science* **2004,** 303, (5659), 777.
16. Wang, R. Y.; Feser, J. P.; Lee, J.-S.; Talapin, D. V.; Segalman, R.; Majumdar, A. *Nano Letters* **2008,** 8, (8), 2283.
17. Bartlett, P.; Ottewill, R. H.; Pusey, P. N. *Physical Review Letters* **1992,** 68, (25), 3801.
18. Trizac, E.; Eldrigde, M. D.; Madden, P. A. *Molecular Physics* **1997,** 90, (4), 675
19. Eldridge, M. D.; Madden, P. A.; Pusey, P. N.; Bartlett, P. *Molecular Physics* **1995,** 84, (2), 395
20. Eldridge, M. D.; Madden, P. A.; Frenkel, D. *Nature* **1993,** 365, (6441), 35.
21. Hynninen, A. P.; Filion, L.; Dijkstra, M. *The Journal of Chemical Physics* **2009,** 131, (6), 064902.
22. Eldrige, M. D.; Madden, P. A.; Frenkel, D. *Molecular Physics* **1993,** 79 (1), (105).
23. Houtepen, A. J.; Koole, R.; Vanmaekelbergh, D.; Meeldijk, J.; Hickey, S. G. *Journal of the American Chemical Society* **2006,** 128, (21), 6792.
24. de Mello Donegá, C.; Hickey, S. G.; Wuister, S. F.; Vanmaekelbergh, D.; Meijerink, A. *The Journal of Physical Chemistry B* **2003,** 107, (2), 489.
25. Brust, M.; Walker, M.; Bethell, D.; Schiffrin, D. J.; Whyman, R. *J. Chem. Soc, Chem. Commun.* **1994,** 801-802.
26. Shevchenko, E. V.; Talapin, D. V.; Murray, C. B.; O'Brien, S. *Journal of the American Chemical Society* **2006,** 128, (11), 3620.
27. Talapin, D. V.; Shevchenko, E. V.; Kornowski, A.; Gaponik, N.; Haase, M.; Rogach, A. L.; Weller, H. *Advanced Materials* **2001,** 13, (24), 1868.
28. Frenkel, D.; Smit, B., *Understanding Molecular Simulations: From Algorithms to Applications*. Academic Press: 1996.
29. Dijkstra, M.; van Roij, R.; Evans, R. *Physical Review E* **1999,** 59, (5), 5744.
30. Derjaguin, B.; Landau, L. *Acta Physicochimica U.R.S.S.* **1941,** 14, 633.
31. Verwey, E. J. W.; Overbeek, J. T. G., *Theory of the Stability of Lyophobic Colloids*. Elsevier: 1948.
32. Likos, C. N. *Physics Reports* **2001,** 348, 267.
33. Israelachvili, J., *Intermolecular and Surface Forces*. Academic Press: London, 1992.

34. Shah, P. S.; Holmes, J. D.; Johnston, K. P.; Korgel, B. A. *The Journal of Physical Chemistry B* **2002,** 106, (10), 2545.
35. Saunders, A. E.; Korgel, B. A. *The Journal of Physical Chemistry B* **2004,** 108, (43), 16732.
36. Bargeman, D.; Vader, F. v. V. *Journal of Electroanallytical Chemistry* **1972,** 37, 45.
37. Ge, G.; Brus, L. *The Journal of Physical Chemistry B* **2000,** 104, (41), 9573.
38. Korgel, B. A.; Fullam, S.; Connolly, S.; Fitzmaurice, D. *The Journal of Physical Chemistry B* **1998,** 102, (43), 8379.
39. Filion, L. Self-assembly in colloidal hard-sphere systems. Utrecht University, Utrecht, 2011.

Appendix 2.1 Interactions

In this appendix a brief summary will be given about the interactions that are used in the computer simulations of binary hard sphere mixtures which are used in this thesis. The simulations were performed by Dr. Laura Fillion working in the group of Prof. M. Dijkstra, at the Soft Condensed Matter group of the Utrecht University.

From thermodynamics, the Helmholtz free energy F of a system consisting of N particles in a volume V, and at temperature T is given by

$$F = U - TS \tag{A2.1}$$

where U is the potential energy, and S is the entropy. For a system consisting of hard spheres the pair potential is given by

$$V_{HS}(r_{ij}, \sigma_i, \sigma_j) = \begin{cases} 0 & r_{ij} > (\sigma_i + \sigma_j)/2 \\ \infty & r_{ij} < (\sigma_i + \sigma_j)/2 \end{cases} \tag{A2.2}$$

where r_{ij} is the distance between particles i and j, and σ_i is the diameter of particle i. Since the Boltzmann weight is zero for configurations that contain particle overlaps, the free energy is determined solely by the entropy. (The potential energy contribution to the free energy for all configurations without overlaps is simply zero, hence only the entropic term is left.)
One method of calculating the exact free energy for a general system, such as hard-sphere mixtures, is thermodynamic integration. In this case, it is assumed that there exists a reference system for which we can calculate the free energy analytically. For example, for liquids often the ideal gas is used and for crystals the Einstein crystal can serve as the reference system. If the potential energy of the reference system is given by U_R and the potential energy of our true system of interest is denoted U_T then it is possible to define a new (fictitious) potential energy

$$U(\lambda) = (1 - \lambda)U_T + \lambda U_R \tag{A2.3}$$

which is now a function of a coupling parameter λ, which varies between 0 and 1. Note that this function has the property that when $\lambda = 0$ it reduces to our system of interest, and when $\lambda = 1$ it reduces to the reference system. The free-energy difference between the reference and the system of interest can be determined exactly[28] and is given by

$$F(\lambda = 1) - F(\lambda = 0) = \int_{\lambda=0}^{\lambda=1} d\lambda \left\langle \frac{\delta U(\lambda)}{\delta \lambda} \right\rangle_{\lambda} \tag{A2.4}$$

Thus, to calculate the free energy exactly we simply need to determine $\langle \delta U(\lambda)/\delta\lambda \rangle_{\lambda}$ as a function of λ. Such an average can be determined using a Monte Carlo simulation.

Additionally, after the Helmholtz free energy is known, all other relevant thermodynamic quantities (such as the Gibbs free energy) can then be obtained.
Once the free energies are known, techniques such as common tangent constructions are used to determine the phase diagrams, and thus, the stability of various candidate phases. Such methods make use of the fact that the temperature, pressure and chemical potential of all the species must be equal in the coexisting phases when the system is in thermodynamic equilibrium. Equivalently, the system always chooses the state with the lowest total Gibbs free energy. Specifically, the system will choose a linear combination of phases such that the total Gibbs free energy is minimized.

In order to make predictions for the phase behaviour of complex fluids, one often resorts to simplified models in which the degrees of freedom of the microscopic species (solvent, polymer) are formally integrated out so that the macroscopic constituents interact via effective interactions. This is a well-trodden pathway in statistical physics and has been applied successfully in colloidal science.[29-32] By integrating out the degrees of freedom of the microscopic species in the partition function, one can derive a formal expression for the effective Hamiltonian for the macroscopic species, which include many-body interactions. If the effective pair interactions are sufficiently short-ranged, three-and higher body effective interactions can be neglected and pairwise additively of the effective pair interactions can be assumed. In the case examined in this chapter, particularly in the case of semiconductor nanoparticle mixtures, both the steric interaction and the screened Van der Waals interactions, are short ranged. As a result, pairwise interaction potentials are expected to be a good first approximation for the effective interaction between nanoparticles. In this section, we consider a pairwise potential consisting of a contribution from a Van der Waals (VdWs) interaction between the cores, a steric interaction between the capping ligands, and a hard-sphere repulsion between the cores. The effective potential is given by

$$\beta V_{eff}(r_{ij},\sigma_i,\sigma_j) = \beta V_{vdw}(r_{ij},\sigma_i,\sigma_j) + \beta V_{steric}(r_{ij},\sigma_i,\sigma_j) + \beta V_{HS}(r_{ij},\sigma_i,\sigma_j) \qquad (A2.5)$$

where r_{ij} is the distance between the center of mass of two nanoparticles i and j, σ_i is the diameter of particle i, $V_{HS}(r_{ij},\sigma_i,\sigma_j)$ is given by equation. A2.2 $\beta = 1/k_BT$, k_B is Boltzmann's constant and T is the temperature. We assume that the Van der Waals interaction between the capping layers can be neglected for a monolayer protected nanocrystal in a good solvent.

The Van der Waals interaction between two core-shell particles labelled i and j at distance r_{ij} with diameters $\sigma_{i(j)}$ and Hamaker constant A is given by[26]

$$\beta V_{vdw}(r_{ij},\sigma_i,\sigma_j) = -\frac{\beta A}{12}\left[\frac{S_{ij}}{D_{ij}\left(1+\frac{D_{ij}}{(\sigma_i+\sigma_j)}\right)} + \frac{1}{1+\frac{D_{ij}}{S_{ij}}+\frac{D_{ij}^2}{\sigma_i\sigma_j}} + 2\ln\left(\frac{D_{ij}\left(1+\frac{D_{ij}}{(\sigma_i+\sigma_j)}\right)}{S_{ij}\left(1+\frac{D_{ij}}{S_{ij}}+\frac{D_{ij}^2}{\sigma_i\sigma_j}\right)}\right)\right] \qquad (A2.6)$$

where $S_{ij} = \sigma_i\sigma_j/(\sigma_i + \sigma_j)$and $D_{ij} = r_{ij} -(\sigma_i + \sigma_j)/2$.
For the Hamaker constant, we consider gold-gold interactions, gold-semiconductor interactions, and semiconductor-semiconductor interactions. For the gold-gold interaction we let $A=3$ *eV*. We note that values for the gold-gold interaction are found between approximately 1.1 and 3 eV[33-36], where we note that some of the literature has used the fact that the gold-gold Hamaker constant is approximately equal to the silver-silver Hamaker constant. The CdSe-CdSe Hamaker constant across a hydrocarbon layer is approximately 0.3 eV[37]. We assume that this value is general for semiconductors. The semiconductor-gold interaction can be derived (approximately) from these interactions using the relation[33] $A_{12} \approx \sqrt{A_1 A_2}$. Note that we assume no temperature dependence of the Hamaker constant.

For the steric interaction, we use the Alexander-de Gennes model.[33] This model approximates the interaction between plates with an absorbed polymer layer in a good solvent with a high coverage of the polymer capping molecules. To transform this interaction between plates to an interaction between spheres of diameter σ_i and σ_j we use the Derjaguin approximation.[33] The resulting interaction between the spheres is given by

$$\beta V_{steric}(r_{ij},\sigma_i,\sigma_j) = \begin{cases} \frac{32\pi S_{ij}L^2}{70s^3}\left[28\left(x_{ij}^{-\frac{1}{4}}-1\right)+\frac{20}{11}\left(1-x_{ij}^{\frac{11}{4}}\right)+12(x_{ij}-1)\right] & r_c < r_{ij} < r_c + 2L \\ 0 & Otherwise \end{cases} \quad (A2.7)$$

where $x_{ij} = D_{ij}/(2L)$, $r_c =(\sigma_1 + \sigma_2)/2$, s is the mean distance between attachment points of the capping ligands (which we refer to as the ligand distance for the remainder of this paper) and L is the thickness of the capping layer. Here we have made the further approximation that the interaction length and ligand distance of the capping layer are the same for all nanoparticle mixtures. In reality, the ligand distance and thickness of the capping layer can be different between the various semiconductor and gold nanoparticles.

In the following section we use the interaction given above to study the effect of particle radius, capping ligand distance and capping layer thickness on the effective semiconductor-semiconductor (SC-SC), gold-gold (Au-Au), and semiconductor-gold (SC-Au) interactions. The various nanoparticles examined in this chapter are capped with either dodecanethiol, or a combination of dodecanethiol and oleic acid. The interaction length of dodecanethiol on a silver nanoparticle is $L\approx1.5$ *nm*.[38] Oleid acid should have a slightly shorter interaction range. For the capping ligand distance, Korgel *et al.* measures a mean distance of $s\approx0.43$ nm between the dodecanethiol ligands on a silver nanoparticle.[38] Using these parameters we plot the effective SC-SC, Au-Au, and SC-Au interactions as a function of size ratio (Figure A2.1A). We observe that since the VdWs interactions between the nanoparticles are weaker for smaller particles, the steric screening is generally more effective for the smaller particles. Similarly, the weaker VdWs interactions for SC-SC mixtures also result in more effective steric screening as compared to the SC-Au and particularly, Au-Au mixtures. In

all cases, the effective interaction displays a strong short-range repulsion and longer-ranged, weak attraction of less than 3 k_BT.

In Figure A2.1B, the effect of temperature on the various interaction types is examined. In all cases, the steric interaction screens the VdWs interactions better at higher temperatures. However, the temperature dependence of the screening is almost negligible in the SC-SC interactions which are well screened even at low temperature: the difference between the attractions over the full range of temperatures studied (150-390K) is much less than 1 k_BT. In contrast, over the same temperature range, the attractive well of the Au-Au effective interactions ranges between approximately 2 to 6 k_BT indicating a much stronger role of temperature in the Au-Au interactions.

The effect of the capping layer thickness is examined in Figure A2.1C. In general, the screening of the VdWs interactions is improved by increasing the capping layer thickness, however, the effect is much less important in the case of SC-SC interactions. While the variation of the attractive well for the SC-SC interactions is less than 0.5 k_BT in all cases, in the case of Au-Au effective interactions, the well depth can be tuned from approximately 1 to 8 k_BT by varying the capping layer thickness between 2 and 1 nm. Additionally, the effective particle size is strongly affected by the thickness of the capping layer.

Finally, in Figure A2.1D the effect of ligand distance s is examined. Specifically, the effective interactions for SC-SC, Au-Au, and SC-Au nanoparticles is plotted for mean distances between ligand molecules between s = 0.3-0.5 nm. In general, the distance between the ligand molecules affects the softness of the short-range repulsion, but has no other significant effect in all cases.

In summary, the SC-SC effective interactions have little dependence on the capping layer details, with only slight variations in the softness of the short-range repulsion and attractive well depths never exceeding 1 k_BT over the complete range of parameters examined. Thus, in all cases it appears that the SC-SC interactions are well modelled by a hard-core repulsion, where the only relevant parameters are the relative size ratio between the radius of the particles and the composition of the mixture. The effective length of the capping ligands will affect the relative size ratio between the particles.

In contrast, the temperature, capping layer thickness, and particle size are found to largely effect the Au-Au effective interactions, and to a much smaller extent, the SC-Au interaction. Thus, in modelling SC-Au, or Au-Au mixtures, the details of the ligand coating is expected to be important in determining effective interactions, and, as a result, the resulting phase behaviour of the system.

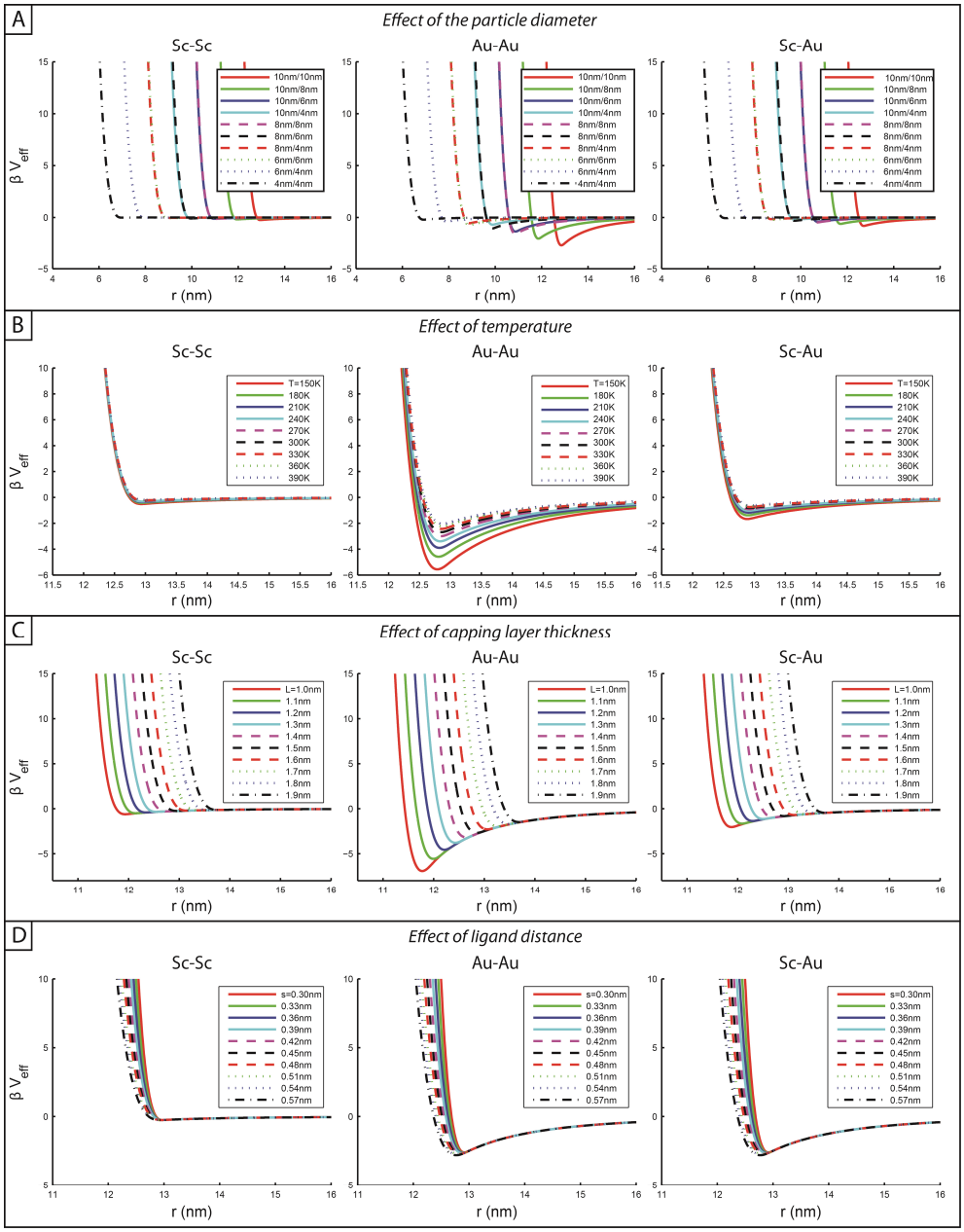

Figure A2.1: Effective interactions between nanocrystals as obtained from Molecular Dynamics simulations (see also the thesis of L. Fillion[39]). From left to right interactions for Semiconductor-semiconductor (Sc-Sc), Gold-Gold (Au-Au) and Semiconductor-Gold (Sc-Au) nanocrystals with Hamaker constant A=0.3 eV, A=3 eV and $A = \sqrt{0.3 * 3}$ eV respectively. A) Effect of particle diameters or particle diameters as labelled and capping layer thickness L=1.5 nm, ligand distance s=0.43nm at temperature of 300K. B) Effect of temperature T between two 10 nm particles (L=1.5 nm, s=0.43 nm). C) Effect of capping layer thickness L between two 10 nm particles (s=0.43 nm, T=300K). D) Effect of ligand distance s between two 10 nm particles (L=1.5 nm, T=300K).

Appendix 2.2 Unknown crystal structures

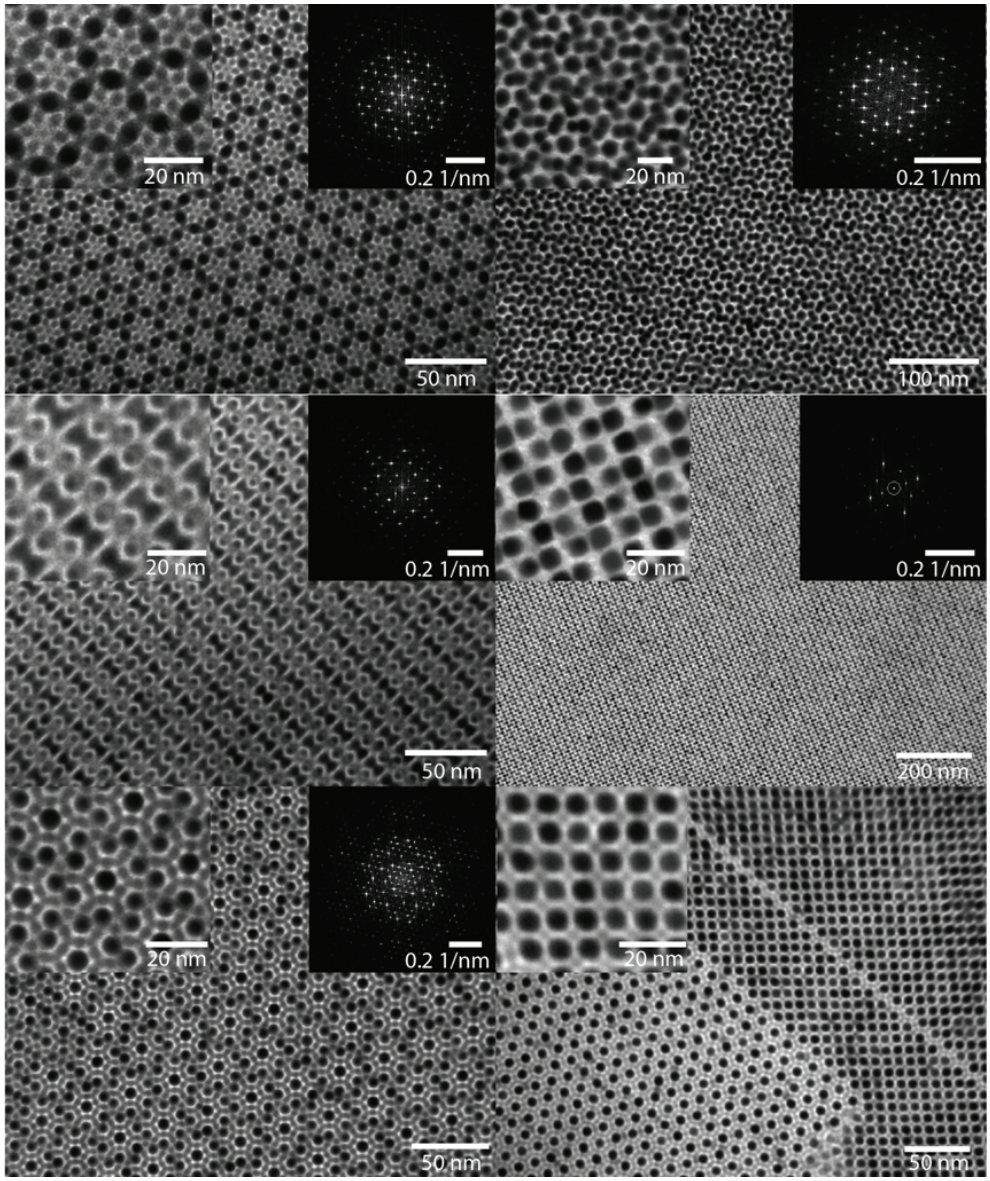

Figure A2.2: Unknown binary superlattices obtained from PbSe and CdSe NCs at a size ratio γ=0.60-0.63. In the inset of each of the images, a zoom in of the TEM pictures of the crystals structures and a Fourier transform are present. Some of the structures have been analyzed by electron tomography, see chapter 4 for more details.

Appendix 2.3 Crystal lattices of PbSe and Au nanocrystals

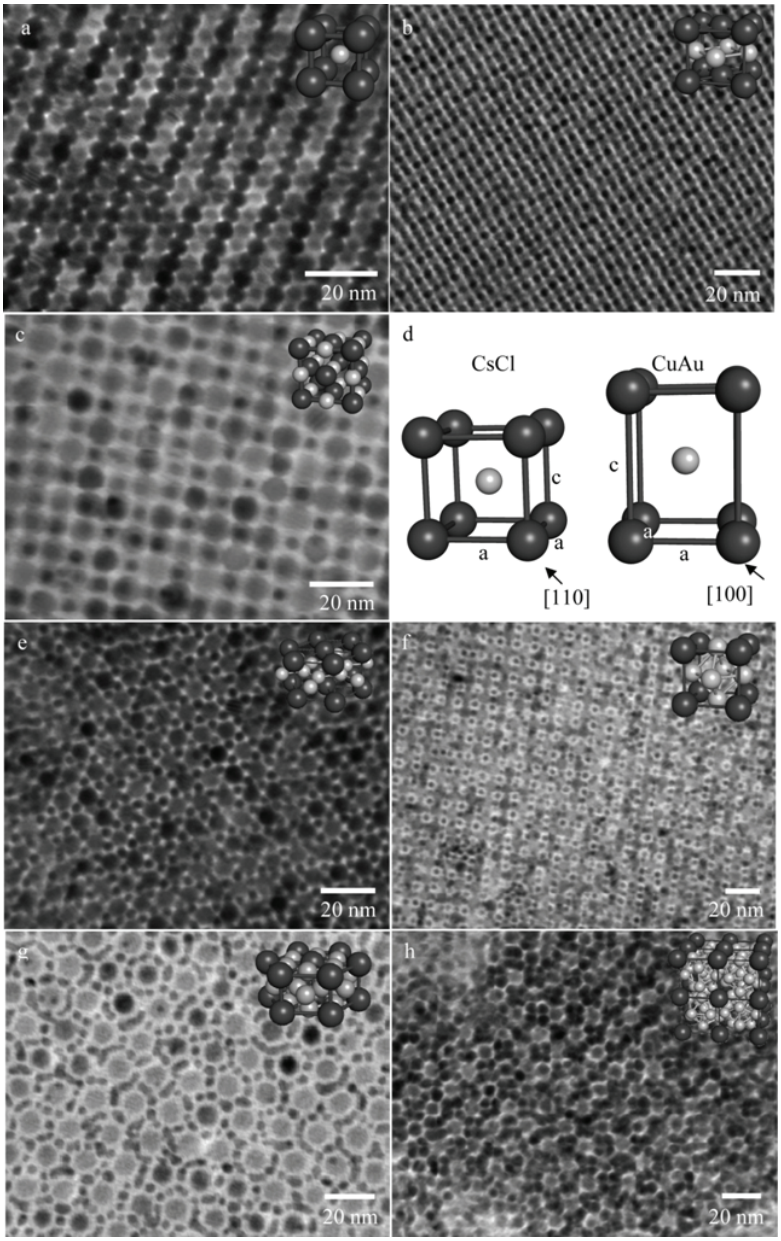

Figure A2.3: Binary superlattices obtained by colloidal crystallization at 70 °C from suspensions of PbSe and Au nanocrystals.(a)-(c) Binary superlattices with AB stoichiometry (a) CuAu structure (γ=0.53), (b) CsCl structure (γ=0.74), (c) NaCl structure (γ=0.47). (d) Cartoon showing the difference between CsCl and CuAu structure. The CsCl structure consists of a cubic lattice of the large particles where the axes of the unit cell are all equal, while the CuAu structure has one prolonged axis. (e) AlB_2 structure (γ=0.61). (f) Cu_3Au (γ=0.47). (g) $CaCu_5$ structure (γ=0.83). (h) $NaZn_{13}$ structure (γ=0.57).

Chapter 3

Observation of a ternary nanocrystal superlattice and its structural characterization by electron tomography

Besides binary self-assembly it is also possible to include a larger complexity by performing self-assembly with more than two different materials. In this chapter, we investigate the formation of superlattice structures upon evaporation of the solvent from a suspension containing three differently sized semiconductor nanocrystals. We show the first genuine ternary colloidal crystal composed of PbSe nanocrystals of two different diameters, and CdSe nanocrystals. Electron tomography shows that the superlattice is isostructural with the atomic lattice $AlMgB_4$.

3.1 Introduction

The crystallization of nanometer-sized colloids and the three-dimensional (3D) structural characterization of the ensuing lattices is a relatively new field compared to that of micrometer-sized colloids being studied extensively since decades. Not much more than ten years ago, it was shown that colloidal CdSe nanocrystals, the work horse of the colloidal quantum dots, form a superlattice upon drying of the suspension.[1] Several years later, again in analogy with micrometer sized colloids, it was reported that gold nanocrystals of two different diameters form binary superlattices.[2] Since then, a plethora of different binary superlattices composed of metallic, magnetic and semiconductor nanocrystals have been demonstrated.[3-9] The research has been driven mostly by the aim of forming novel meta-materials, with collective properties that result from interactions between nanometer-sized semiconductors, metals and magnets, in close contact in a well-ordered 3-D geometry. Many of the known atomic binary lattices now have their counterpart both in colloidal crystals of micrometer[10] and nanometer-sized colloids.

Atomic lattices can also consist of three or more different types of atoms. However, the colloidal counterpart of a ternary atomic lattice has not been observed. Here, we report a genuine ternary nanocrystal (NC) superlattice ABC_4 composed of three different nanocrystals; i.e. A = PbSe NC of 12.1 (± 0.4 nm) in diameter, B = PbSe NC of 7.9 (± 0.3nm), C = CdSe NC of 5.8 (± 0.3 nm). We studied colloidal crystallization upon evaporation of the solvent from a suspension that contains these nanocrystals in relative concentration ratios [B]/[A]=1.3, [C]/[A]=10.9. We observe ternary domains ABC_4, iso-structural with the atomic lattice $AlMgB_4$, formed together with the binary superlattices AC_2 (iso-structural with AlB_2) and BC_2 (iso-structural with $MgZn_2$). The 3D structure of this genuine ternary nanocrystal superlattice has been studied in detail with electron tomography.

3.2 Experimental

PbSe Nanocrystals were synthesized by a method described by Houtepen *et al.*[11] The synthesis was performed in a water and oxygen free environment. (1) 1.9 gram of lead acetate tri hydrate (99.999% Aldrich), 4 mL of diphenyl ether (99% DPE, aldrich), 3 mL of oleic acid (OA, 90% Aldrich) and 16 mL trioctyl phospine (TOP, 90% Fluka) were heated to 100 °C under low pressure (10-3 bar) for ~3 hours. (2) A second mixture containg 0.31 g Se (99.999% Alfa Aesar) and 4 mL TOP was prepared. Subsequently 11.5 mL of solution (1) and 1.7 ml of solution (2) was injected into 10 mL 190 °C DPE. The reaction mixture was kept at a constant temperature of 145 °C. After 30 seconds to 10 minutes the reaction mixture was quenched with 20 mL butanol and 10 mL methanol. The crude synthesis

mixtures were washed twice by precipitating with methanol, centrifugation and redispersion of the sediment in toluene.

CdSe nanocrystals were synthesized by a method described by de Mello Donega *et al.*[12] The synthesis was performed in a water and oxygen free environment. 0.79 gram of Selenium (99.999% Alfa Aesar), 0.28 g of dimethylcadmium (99.99% ARC Technologies) and 10 mL of TOP (96% Aldrich) was prepared. The solution was injected into a mixture of 20 gram dried trioctylphospineoxide (TOPO, 99% Aldrich) and 10 g hexadecylamine (HDA) at a temperature of ~300 °C, resulting in a temperature drop to ~170 °C. The temperature was raised and stabilized to the desired growth temperature of 240 °C for 30 minutes, resulting in nanocrystals with a diameter of approximately 3 nm. The synthesis mixtures were washed twice by precipitating with methanol, centrifugation and redispersion of the sediment in toluene.

Superlattice formation was achieved by mixing the three colloidal suspensions to obtain a mixed suspension containing the PbSe nanocrystals (A and B) and the CdSe NC (C); the concentration ratio in this mixed suspension is approximately [B]/[A]=1.3, [C]/[A]=10.9 and [C]/[B]=8.2. Colloidal crystallization was achieved on a TEM grid that makes an angle of 30 degrees with the suspension surface, evaporating the solvent at a temperature of 70 °C under reduced pressure.

3.3 Results and discussion

Upon evaporation of the solvent from the ternary suspension, nanocrystal films are formed on the TEM grid. Some regions on the TEM grid display ordered domains (superlattices) with lateral dimensions in the 1 μm range. Besides a small percentage of single-component superlattices, three different crystal structures could be distinguished: domains of binary AC_2 and BC_2 superlattices (Figure 3.1), together with domains of a ternary superlattice that contains the large and medium-sized PbSe NC and the CdSe NC. Figure 3.2 shows a TEM projection of the ternary superlattice; the three different nanocrystals are clearly visible in the TEM projection, see also the overlay. We observed that the ternary domains are epitaxially connected to binary AC_2 domains (the dashed line in Figure 3.2 depicts such an epitaxial interface). The binary lattice on the top-right corner of Figure 3.2 is iso-structural with AlB_2. The ternary lattice can be derived from the binary lattice, by substituting every second vertical layer of large PbSe NC (blue in the overlay) by middle-sized PbSe NC (green in the overlay). In fact, Figure 3.2 shows the (100) plane of the ternary ABC_4 structure, identified as iso-structural with the atomic $AlMgB_4$ crystal. The ternary domains that we have analyzed always have the (100) plane parallel to the substrate surface. A 3-D model of this crystal as observed here (substrate on the bottom) is presented in Figure 3.3E. We note that in the ordered regions of the TEM grid also BC_2 binary superlattices (consisting of medium-sized PbSe NC and small CdSe NC) are observed, iso-structural with $MgZn_2$ (Figure 3.1).

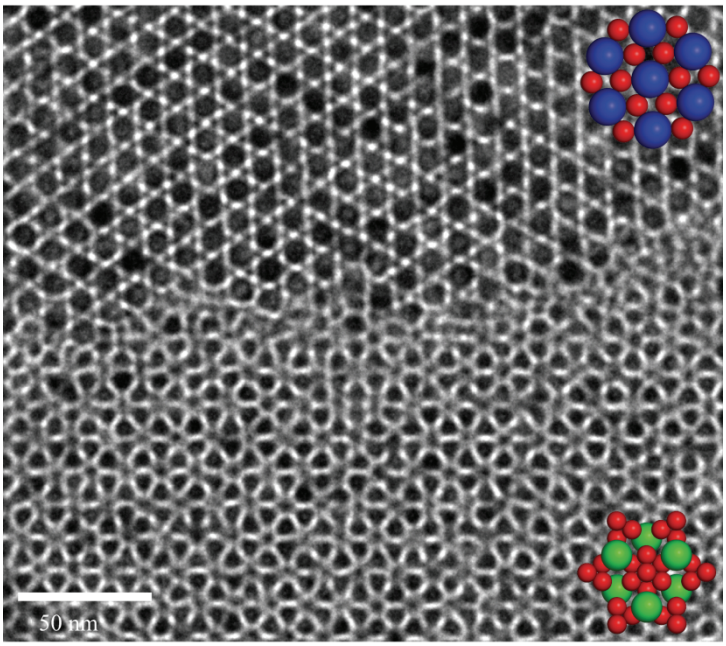

Figure 3.1: TEM projection of the AC_2 (top), iso-structural with AlB_2, and the BC_2 (bottom), iso-structural with $MgZn_2$. The cartoons show the corresponding structures in the (001) orientation.

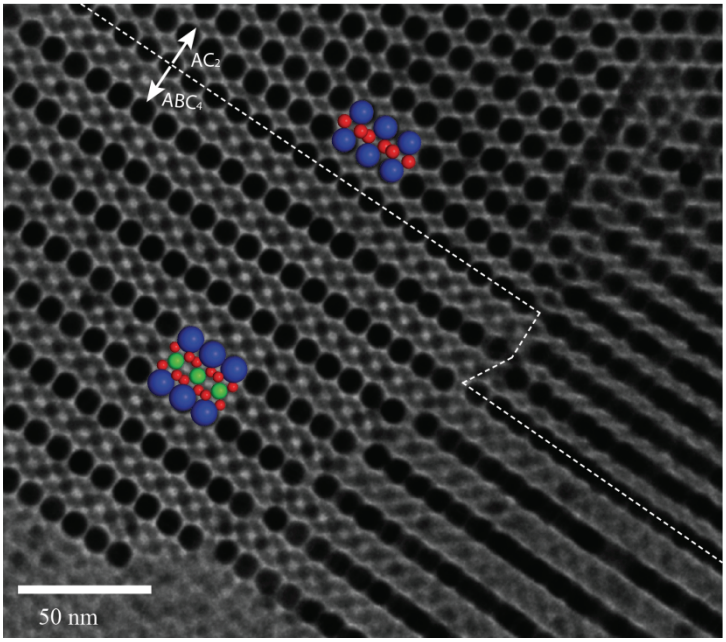

Figure 3.2: TEM projection of the ternary ABC_4, i.e. $[PbSe(l)][PbSe(m)][CdSe(s)]_4$ nanocrystal superlattice in epitaxial contact with the binary AC_2 superlattice $[PbSe(l)][CdSe(s)]_2$. The TEM picture and cartoon show the (100) plane of the ternary superlattice, where the large PbSe NC (blue spheres), middle-sized PbSe (green spheres) and small CdSe (red spheres) can be observed individually. The ternary nanocrystal superlattice is isostructural with $AlMgB_4$.

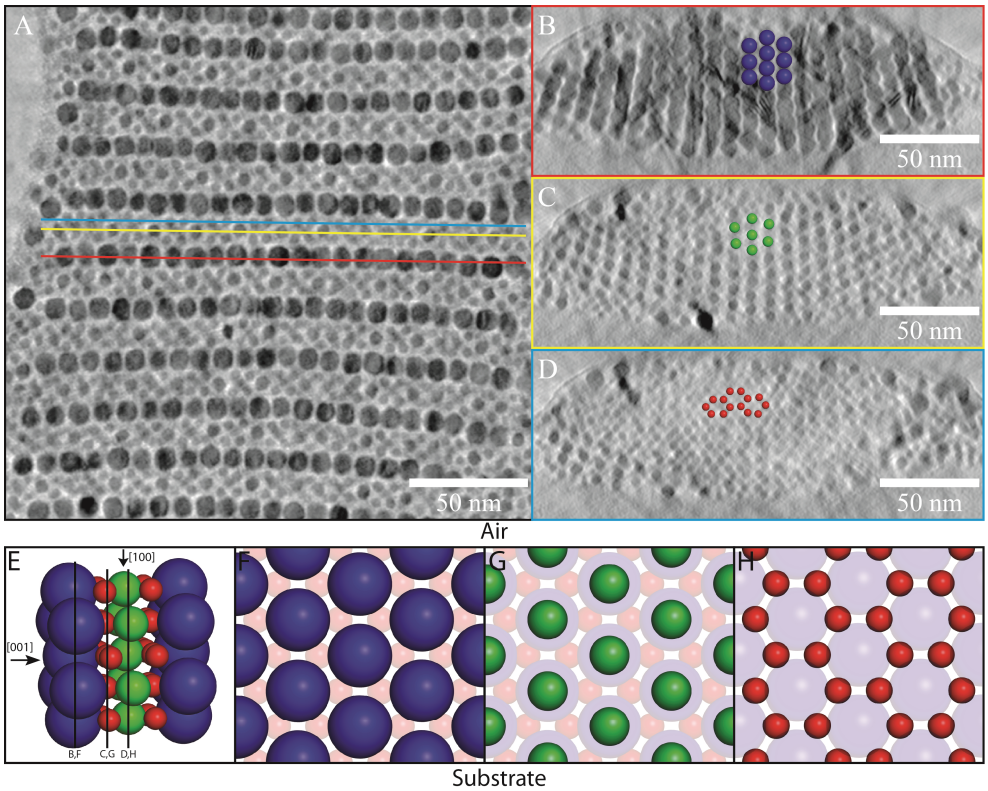

Figure 3.3: Tomographic analysis of the ternary ABC_4 structure. A shows a horizontal cross section through the center of the large PbSe NC lying in the [100] plane of the 3 D reconstructed lattice. The cross section cuts also through half of the middle-sized PbSe and small CdSe nanocrystals. The colored lines show the positions of the vertical cross sections through the center of the large PbSe NC (red), middle-sized PbSe NC (yellow) and small CdSe NC (blue) displayed in panels B, C, D, respectively. E shows a model of the ternary structure as observed with the substrate on the bottom side; F,G,H display models of the vertical cross sections through the large PbSe (blue), medium-sized PbSe (green), and small CdSe (red), corresponding to the experimental cross sections B-D.

We performed electron tomography of the ternary domains by acquiring TEM projections over an angular range of 140 degrees at two degrees increments, followed by alignment of the data set by fiducial markers and reconstruction of the 3-D lattice by weighted backprojection.[8] Tomography was performed in collaboration with Dr. H. Friedrich. Figure 3.3 shows numerical cross-sections through a reconstructed ternary lattice; Figure 3.3A shows a horizontal cross section taken through the center of the larger PbSe nanocrystals of the ternary structure that has the [100] planes parallel with the substrate (see Figure 3.3E). The cross section also cuts through the center of half of the medium-sized PbSe and small CdSe NC. It can be seen that the cores of the larger PbSe NC are separated by the organic capping. The colored lines indicate the positions of vertical cross sections, displayed in Figure 3.3 B-D. Figure 3.3 B presents the vertical cross section through the center of the large nanocrystals. Strikingly, the PbSe cores seem to touch each other in the

vertical direction; hence at these specific positions the organic capping disappeared. Note the difference with a cross-section through the model lattice displayed in Figure 3.3F. The center-to-center distance in the vertical direction is about 8.0 nm on average, which is equal to the core diameter. This lattice contraction is similar to what is observed with AlB_2 binary superlattices of PbSe and CdSe[8]; we attribute this to drying effects. Very probably, drying effects are also causing the bending deformation of the ternary lattice visible in Figure 3.3B and C. Figure 3.3C presents a vertical cross-section through the center of the medium-sized PbSe NC. Note that the center-to-center distance is identical to that in the planes of the large PbSe nanocrystals. In fact, the medium-sized PbSe nanocrystals are positioned on the same sites as their larger counterparts (see also the model cross sections Figure 3.3F and G). Figure 3.3D shows a vertical numerical cross-section through the center of the small CdSe (model displayed in Figure 3.3F); the fact that at the boundaries also large and middle-sized nanocrystals are displayed is due to a slight bending of the overall lattice. We note that the $AlMgB_4$ structure that we observe is very similar to the AlB_2 binary structure. Hence, epitaxial boundaries between the ternary and binary lattices are no surprise (Figure 3.4).

Finally, we discuss the possible reasons that genuine ternary structures are formed spontaneously in this system. At present, the driving force for the formation of *binary* nanocrystal superlattices is under discussion[6]; some authors explain the stability of these crystal structures by entropy alone using packing arguments, others speculate that the structures are stabilized by the interactions between the nanocrystals. Since we have already proved in the previous chapter that the entropy is the main driving force in binary self-assembly of a binary mixture of semiconductor nanocrystals, we limit the discussion to the entropic contribution to the free energy of formation of the binary AlB_2[13], and $MgZn_2$[14] and ternary $AlMgB_4$ NC superlattices. This is also rationalized by the fact that we have performed the colloidal crystallization at a relative high temperature (70 °C) where the entropy contribution to the free energy should be prevailing.

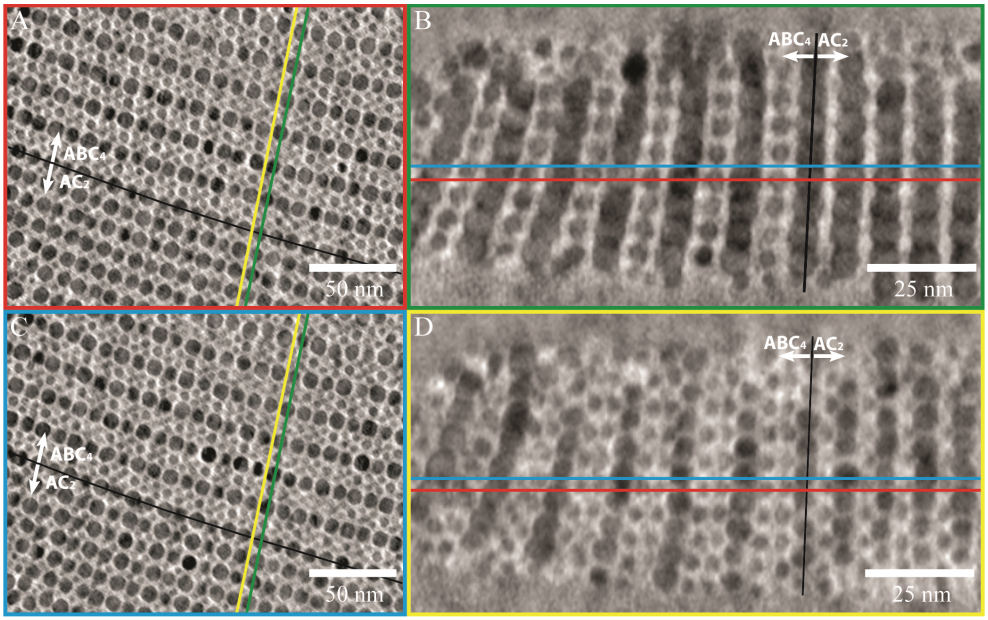

Figure 3.4: Reconstruction slices of the ternary superlattice ABC_4 (isostructural with $AlMgB_4$) epitaxially connected to a binary superlattice AC_2 (isostructural with AlB2). A and C show horizontal cross sections separated by half a monolayer in height as is indicated in figures B and D. The green en yellow lines indicate the positions of the vertical cross sections displayed in B, D. B and D present the epitaxy of the ternary structure (left hand side) to the binary AlB_2 structure. The cross section B cuts the large and medium sized PbSe NC; the cross section D cuts also the small CdSe NC.

Since we have three different sizes in the mixed suspension, we have to consider three size ratios: γ_1 = diameter CdSe NC /diameter large PbSe NC = 0.48, γ_2 = diameter CdSe NC /diameter medium-sized PbSe NC = 0.73, and γ_3 = diameter PbSe medium-sized/diameter large PbSe NC = 0.65. For a size ratio of 0.48, the phase diagram of a binary mixture of hard spheres displays a stable binary superlattice AC_2, i.e. PbSe(largeNC)/$[CdSeNC]_2$, isostructural with AlB_2.[13, 15] Furthermore, recently calculated phase diagrams for binary hard-sphere mixtures using computer simulations show that the $MgZn_2$ lattice is stable for a size ratio between 0.76 and 0.84[14], hence just above γ_2. In agreement with this, we observed that the ordered regions on the TEM grid are dominated by AlB_2-type AC_2 structures (about 65% of the film) and $MgZn_2$-type BC_2 superlattices (about 25% of the ordered film). An advanced calculation is needed to calculate the free energy of the ternary $AlMgB_4$ colloidal crystal that we observe (occupying about 5 % of the ordered regions) and to predict the phase behavior of the three component system. As a start, we have calculated the maximum filling fraction of the $AlMgB_4$ lattice as a function of the size ratios γ_1, γ_2 and γ_3 (Figure 3.5). There is a considerable region where the filling fraction exceeds 0.74 suggesting that the ternary lattice might be thermodynamically stable. The corresponding coordinates γ_1

and γ_2 point also to stable AlB_2 and $MgZn_2$ superlattices, as observed. We conclude that the occurrence of binary AlB_2 and $MgZn_2$ superlattices agrees with the phase

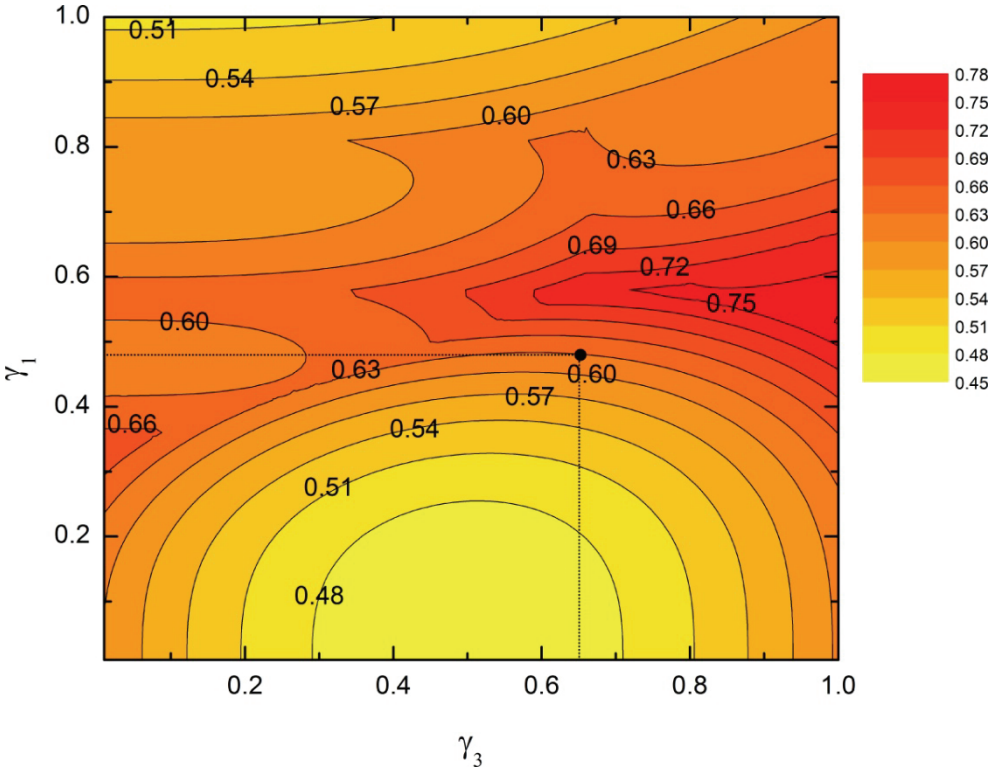

Figure 3.5: Contour plot of the maximum packing fraction of the ternary structure $AlMgB_4$ as a function of the size ratio's γ_1 = diameter small particle / large particle, and γ_3 = diameter medium sized particle / large particle. The maximum packing fraction was determined using Monte Carlo simulated annealing.[16] Notice that there is a considerable region in which the maximum packing fraction of the ternary structure is similar to that of a fcc single component lattice, indicating that the ternary structure $AlMgB_4$ might be stable. The point in which the $AlMgB_4$ structure was observed is indicated.

diagrams of binary hard-sphere mixtures; since the ternary $AlMgB_4$ lattice has a very similar structure to that of AlB_2, it is suggested that its formation is also driven by an increase in entropy.

3.4 Conclusion

We have presented the first genuine ternary colloidal crystal, being a ternary superlattice composed of PbSe nanocrystals of two different diameters, and CdSe nanocrystals. TEM

and electron tomography shows that its structure is iso-structural with the $AlMgB_4$ atomic lattice.

References

1. Murray, C. B.; Kagan, C. R.; Bawendi, M. G. *Science (Washington, D. C.)* **1995,** 270, (5240), 1335-8.
2. Kiely, C. J.; Fink, J.; Brust, M.; Bethell, D.; Schiffrin, D. J. *Nature* **1998,** 396, (6710), 444-446.
3. Redl, F. X.; Cho, K.-S.; Murray, C. B.; O'Brien, S. *Nature* **2003,** 423, 968-971.
4. Shevchenko, E. V.; Talapin, D. V.; Kotov, N. A.; O'Brien, S.; Murray, C. B. *Nature* **2006,** 439, (7072), 55-59.
5. Chen, Z. Y.; Moore, J.; Radtke, G.; Sirringhaus, H.; O'Brien, S. *Journal of the American Chemical Society* **2007,** 129, (50), 15702-15709.
6. Chen, Z.; O'Brien, S. *Acs Nano* **2008,** 2, (6), 1219-1229.
7. Overgaag, K.; Evers, W.; de Nijs, B.; Koole, R.; Meeldijk, J.; Vanmaekelbergh, D. *Journal of the American Chemical Society* **2008,** 130, (25), 7833.
8. Friedrich, H.; Gommes, C. J.; Overgaag, K.; Meeldijk, J. D.; Evers, W. H.; de Nijs, B.; Boneschanscher, M. P.; de Jongh, P. E.; Verkleij, A. J.; de Jong, K. P.; van Blaaderen, A.; Vanmaekelbergh, D. *Nano Letters* **2009,** 9, (7), 2719-2724.
9. Rogach, A. L. *Angewandte Chemie-International Edition* **2004,** 43, (2), 148-149.
10. Leunissen, M. E.; Christova, C. G.; Hynninen, A. P.; Royall, C. P.; Campbell, A. I.; Imhof, A.; Dijkstra, M.; van Roij, R.; van Blaaderen, A. *Nature* **2005,** 437, (7056), 235-240.
11. Houtepen, A. J.; Koole, R.; Vanmaekelbergh, D.; Meeldijk, J.; Hickey, S. G. *Journal of the American Chemical Society* **2006,** 128, (21), 6792-6793.
12. de Mello Donegá, C.; Hickey, S. G.; Wuister, S. F.; Vanmaekelbergh, D.; Meijerink, A. *The Journal of Physical Chemistry B* **2003,** 107, (2), 489-496.
13. Eldridge, M. D.; Madden, P. A.; Pusey, P. N.; Bartlett, P. *Molecular Physics* **1995,** 84.
14. Hynninen, A. P.; Filion, L.; Dijkstra, M. *The Journal of Chemical Physics* **2009,** 131, (6), 064902-9.
15. Trizac, E.; Eldrigde, M. D.; Madden, P. A. *Molecular Physics* **1997,** 90, (4), 675 - 678.
16. Filion, L.; Dijkstra, M. *Physical Review E* **2009,** 79, (4), 046714.

Chapter 4

Electron tomography as a tool to study binary self-assembled nanocrystal superlattices

Self-assembly of colloidal nanocrystals is considered as an inexpensive and versatile route for the synthesis of functional materials with synergetic properties. In this respect, identification and classification of the sometimes complex crystal structures and their polymorphs is a key aspect in the quest for a reliable structure-function relationship. A first example of the use of electron tomography in the characterization of superlattice structures was presented in chapter 3. Here, we show that with electron tomography a comprehensive, quantitative, three-dimensional characterization of these systems down to the single nanocrystal level can be achieved, which is crucial in understanding the emerging materials properties. We performed two case studies to show the merits of tomography for classification of binary superlattices. In the first example, we illustrate for four binary lattices composed of PbSe, CdSe, and Au nanocrystals, that ambiguous interpretations based on two-dimensional transmission electron microscopy can be prevented, nanocrystal sizes and superlattice parameters accurately determined, individual crystallographic point and plane defects studied, and the order/disorder at the top and bottom surfaces imaged. Furthermore, our results suggest that superlattice nucleation and growth occurred at the suspension/air interface and that the unit cells of some lattices are anisotropically deformed upon drying. In the second case, we show that two-dimensional electron transmission images can lead to misunderstanding when the structure is complex. Using three-dimensional electron tomography, we found that three different electron transmission images of unknown stoichiometry originate from the same crystal structure. Furthermore, three-dimensional reconstruction enabled us to find the correct crystal structure A_6B_{19} of this assembly, which has no analogue in atomic lattices.

4.1 Introduction

As technology's demand for more sophisticated materials with versatile properties remains increasing, the interest for nanocrystal-based materials has grown rapidly over the recent years. An inexpensive and versatile route for the preparation of these structures is the bottom-up approach. The versatility is related to the two-step approach of first preparing colloidal nanocrystals (NCs) from atomic precursors, and secondly, combining any conceivable combination of metallic, magnetic and semiconductor nanocrystals, achieving nanocrystal superlattices (NCSL) by self-assembly.[1-3] In these systems, new properties can emerge from the quantum mechanical and dipolar interactions between the building blocks[4-8]. An example has been published showing that NCs that are inherently insulating, when assembled in a binary superlattice, led to a material with strongly enhanced conductivity.[9] To understand these properties it is essential to know the superlattice structure in detail, including the deformations and crystal defects.

Previous studies have already shown that NCSL can be formed in a plethora of different crystals structures that are also known from the atomic world.[10] However, NCSL often show slight variations and distortions depending on the details of the self-assembly conditions.[7, 11-13] This feature is very different from atomic lattices where even slight modulations referred to the ideal lattice structure are energetically forbidden, due to the nature of the covalent and ionic bonding. The deformations and polymorphs present in self-assembled NCSL, though interesting from a purely scientific viewpoint, hamper the identification and classification of NCSL crystal structures. They, for instance, result in blurring of both transmission images and of characteristic spots in scattering techniques. It is thus a tremendous task to analyze complex NCSL and find the correct crystal structure as this will entail the recognition of different crystal orientations and the effects of deformations and extended defects.

Structural analysis based on Transmission Electron Microscopy (TEM) has proven to be an important tool for progress in this field. For instance, by careful analysis of the superlattice structures formed by two types of semiconductor NC with different size and comparing these structures with the predictions of the hard-sphere model, it could be concluded that entropy can be an important driving force for the NC self-assembly (chapter 2).[14] Another example: the understanding of self-doping in a binary NCSL of PbTe and Ag_2Te NCs also required a detailed structural analysis.[9] Being a technique that provides direct and local information, TEM is the first choice for structural characterization of such systems. It has, however, the inherent drawback of being a projection method. This first of all means that (nearly) all information along the beam axis is lost, making it very difficult to study information about buried lattice defects and distortions. This information is important, since the van der Waals forces between the NC building blocks are more forgiving for crystal distortions and defects than the stronger and more directional forces in atomic lattices.

Furthermore, the TEM projections of self-assembled NCSL are, though astoundingly beautiful, often very complex and variable. As a consequence, the direct determination of the crystal structure and the recognition of different projection patterns as originating from one crystal structure has proven to be challenging.

In order to further increase our understanding of self-assembled NCSL and the design of new nanostructured metamaterials, a complete 3D structural characterization with a method that provides local information is highly desirable. A tool for complete 3D structural analysis is electron tomography, a technique based on the reconstruction of a 3D object from a series of 2D TEM projections obtained at different angles between the incoming electron beam and the 3D object.[15, 16] The advantage of this technique with respect to scattering techniques is its ability to provide local information about e.g. defects and boundaries. Electron tomography has already shown its potency for full 3D characterization of several binary as well as ternary (chapter 3) NCSLs including the defects and recently even of atomic lattices.[17-20]

In the first part of this chapter, we present a study on four binary superlattices of AB_2 and AB_{13} (PbSe and CdSe NCs) and of AB_2 and AB stoichiometry (PbSe and Au NCs) and show how electron tomography enabled us to do a comprehensive structural analysis of binary NC superlattice by quantifying individual NC coordinates, sizes, unit cell parameters and furthermore characterizing point and planar defects. Furthermore, our results suggest that superlattice nucleation and growth occurred at the suspension/air interface and that the unit cells of some lattices are anisotropically deformed upon drying.

In the second part of this chapter, we present how electron tomography enabled us to resolve a complex (unknown) crystal structure formed by self assembly of PbSe and CdSe NCs. We will show that different unresolved TEM projections reflect, in fact, the same complex crystal structure, whereby a straightforward analysis was hindered by planar rotations and misorientations. To the best of our knowledge, the observed superlattice crystal structure with a stoichiometry PbSe:CdSe of 6:19 has no reported analogue in atomic lattices.

4.2 Experimental

The oleic acid capped PbSe and trioctylphosphine oxide/hexadecylamine capped CdSe NCs were prepared according to methods reported in the literature.[21, 22] For more details see chapter 2.

The binary superlattices of AB_2 (with effective size ratio γ_{eff} of 0.53) and AB_{13} (γ_{eff} 0.56)and the “unknown” A_6B_{19} stoichiometry (γ_{eff} 0.61-0.67) (PbSe and CdSe NCs) and of

AB_2 (γ_{eff} 0.53) and AB stoichiometry (γ_{eff} 0.64) (PbSe and Au NCs) crystal structures were prepared as discussed in chapter 2.[4] TEM images of the obtained structures are given in Figure 4.1("known" stoichiometry) and Figure 4.6 ("unknown" stoichiometry). In short, mixed suspensions of trioctylphosphine oxide (TOPO)/hexadecylamine (HDA) capped-CdSe and oleic acid (OA)-capped PbSe nanocrystals (NCs) were prepared in tetrachloroethylene (TCE), while suspensions of dodecanethiol-capped gold NCs and OA-capped PbSe NCs were prepared in toluene in an oxygen and water-free environment. By varying the NC size ratio and/or concentrations in suspension different binary superlattices could be prepared. Colloidal crystallization proceeded by evaporating the solvent under reduced pressure (~10 mbar) at 70 °C with the substrate kept at an angle of 30° to the horizontal. Carbon-coated Formvar films supported on Cu TEM grids were used as substrates. PbSe/ CdSe NC structures of AB_2 and AB_{13} stoichiometry were mainly formed at a particle concentration ratio of C_{CdSe}/C_{PbSe} of 5 and 12, respectively. PbSe/ Au structures of AB and AB_2 stoichiometry were formed at a C_{Au}/C_{PbSe} ratio between 1 and 5. The "unkown" crystal structures were prepared with a concentration ratio of 1:4 C_{PbSe}/C_{CdSe}. The particle concentration ratios were determined from absorption measurements using a Lambda 950 UVvis spectrometer and according the sizing curves described by Moreels et al. (PbSe)[23] , Yu et al. (CdSe)[24] and Liu et al. (Au)[25].

Electron tomography was performed in bright-field mode using a Tecnai 20 electron microscope with a LaB_6 electron source (FEI Company, Eindhoven). Images of the tilt-series were acquired over an angular range of (~70° at 2° increments on a Tietz 2k × 2k charge-coupled device camera (TVIPS Gmbh, Gauting) using Inspect3D software (FEI Company, Eindhoven). The defocus was set to -200 to -300 nm (nominal) to keep the entire object in underfocus throughout the tilt-series and an objective aperture of 40 µm was inserted in the beam path. Images of the tilt-series were aligned with respect to a common origin and rotation axis using the PbSe or Au particles as fiducial markers. The aligned tilt-series was binned to 0.54 or 0.23 nm pixel size, which is approximately the interpretable resolution at the experimental imaging conditions prior to reconstruction of the three-dimensional (3D) volume. An example is provided online[17] (SImovie1.mpg) showing an aligned tilt series of the AB_{13} lattice acquired over an angular range of 70°-65° at 2° increments. This data acquisition scheme is commonly referred to as single-axis tilting.[26] The 3D intensity map of the object is reconstructed by weighted backprojection.[27] The corresponding reconstruction of the AB_{13} lattice is displayed online[17], SImovie2.mpg by sequential numerical cross sections parallel to the imaging plane at different heights (see also cartoon in Figure 4.2a). SImovie2 starts at the back side of the support film, moving upward through the support film and the superlattice and then back downward. A comprehensive description of electron tomography can be found in refs [16, 26, 28] and [27]. Alignment and reconstruction by weighted backprojection was performed in IMOD.[29]

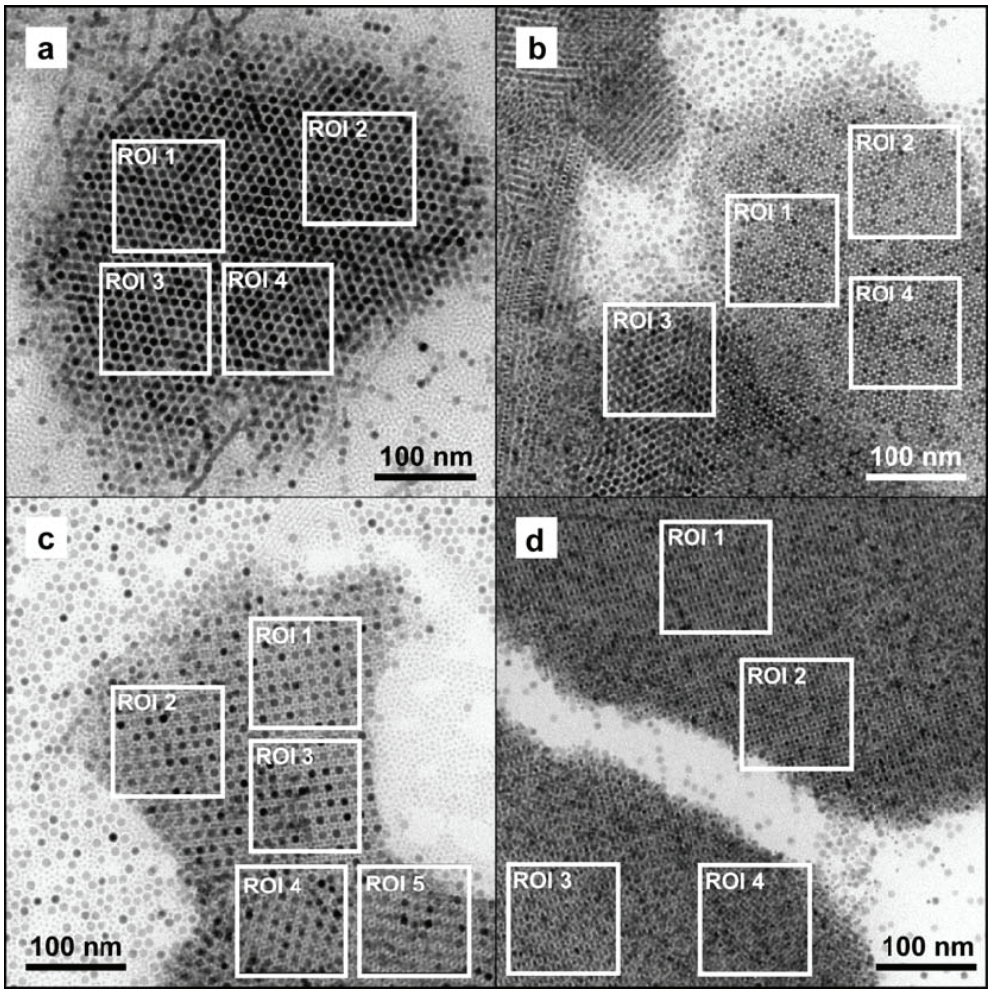

Figure 4.1: TEM images of the examined "known" superlattices at zerotilt and regions of interest (ROI) which were analyzed in terms of particle size, soft shell thickness, unit cell vectors and angles, and underlying crystallographic lattice. (a) AB_2 consisting of PbSe and CdSe NCs, (b) AB_2 consisting of PbSe and Au NCs, (c) AB_{13} consisting of PbSe and CdSe NCs and (d) AB consisting of PbSe and Au NCs.

Particle detection was done using template matching in Matlab as described by Friedrich et al.[17] Following on the particle detection a statistical analysis of the unit cell was performed. The unit vectors were determined by averaging over the nearest neighbor distances that were determined by a Voronoi analysis. Particle positions were then expressed as a distance from the origin of their respective unit cells. Averaging over these distances resulted in the final coordinates. Since the spread in the CdSe positions was very large we used an additional detection criterion. This was to only include positions that were separated over at least one CdSe diameter (inorganic core diameter) from other CdSe positions within the same unit cell.

4.3 Results and discussion

In this paragraph the result and discussion of the two cases will be given. We will start with the results of the analysis of the electron tomograms of the "known" AB, AB_2 and AB_{13} stoichiometry composed out of PbSe and CdSe or PbSe and Au NCs. In the second part of this paragraph we present how electron tomography enabled us to resolve a complex (unknown) crystal structure formed by self assembly of PbSe and CdSe NCs.

4.3.1 Quantitative Structural Analysis of Binary Nanocrystal Superlattices of AB, AB_2 and AB_{13} composition by Electron Tomography

The crystallographic analysis of the AB_2 superlattice containing PbSe and CdSe NCs is summarized in Figure 4.2b-e (see Figure 4.1a and Table A4.1 in the appendix for more details). The lattice parameters varied less than 5% between different subregions, NC core diameters were constant (9 nm PbSe; 3.4 nm CdSe), and a thickness of 4 to 5 unit cells was observed. The relative positions of the NCs in the unit cell confirmed ordering isostructural with AlB_2 (space group 191), however, with a strong contraction perpendicular to the substrate plane (C-vector). While in the [001] plane (Figure 4.2c) the PbSe NC are well separated by the organic ligand shell, in the [1-10] plane (Figure 4.2d) no gap between the NC cores is visible. The absence of a visible gap in the [1-10] plane results from a compression of the organic ligand shell perpendicular to the support and from blurring by the reconstruction point spread function. The reason for the strong anisotropic contraction will be discussed below in context of superlattice formation. More details on the second AB_2 lattice (7.1 nm PbSe; 3.7 nm Au; thickness 2-4 unit cells) also exposing AlB_2 ordering and contraction are provided in Figure 4.1b, Figure 4.3d-g, and appendix Table A4.2.

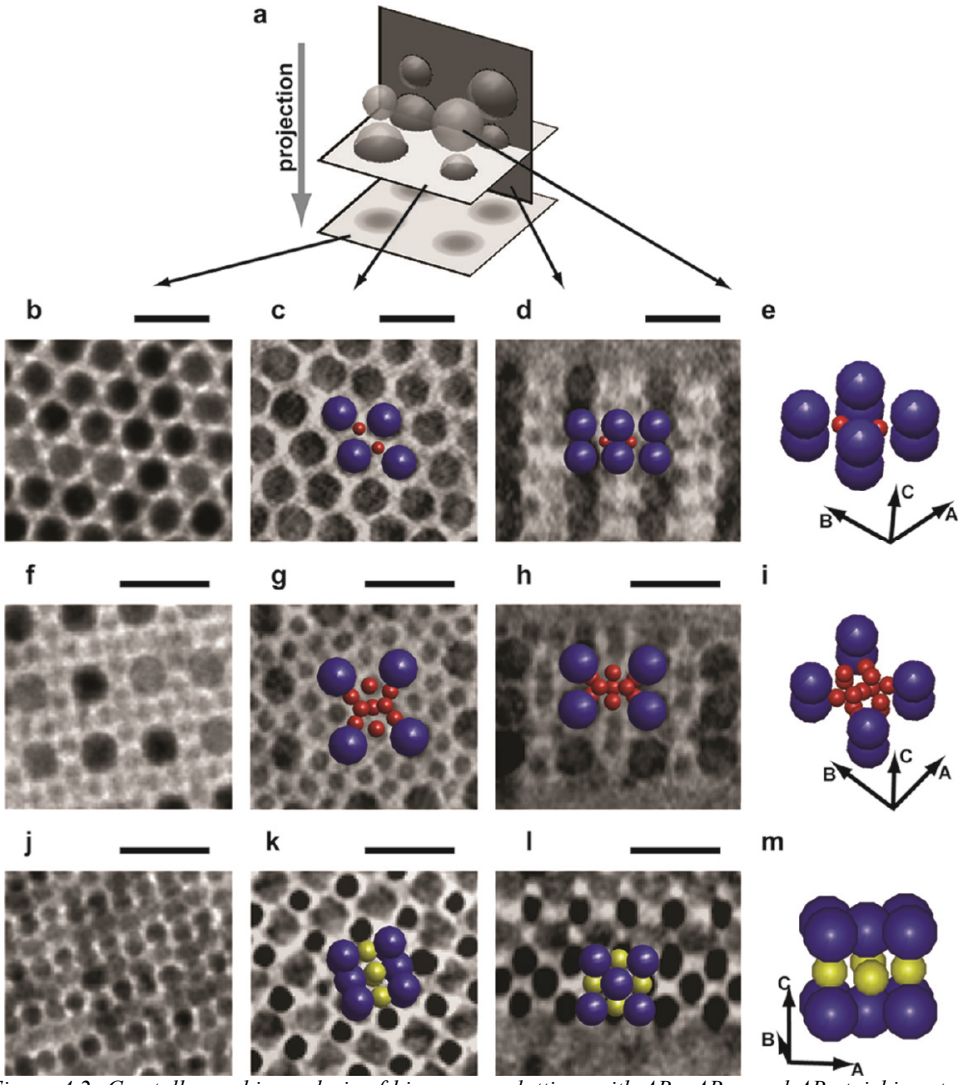

Figure 4.2: Crystallographic analysis of binary superlattices with AB_2, AB_{13}, and AB stoichiometry. (a) Cartoon explaining the relationship between the panels below. TEM image (left), numerical cross section through 3D reconstruction (3D intensity map) parallel to imaging plane (left center), numerical cross section perpendicular to imaging plane (right center), and unit cell showing the nanocrystal cores with lattice vectors (right). (b-e) AB_2 superlattice of 9 nm PbSe (blue) and 3.4 nm CdSe NCs (red) with (b) TEM image interpolated from 0.54 nm/px along (001) direction at zero tilt, (c) cross section through [001] plane of PbSe NCs, the CdSe NCs are 1/2 unit cell higher, (d) cross section through [1-10] plane of PbSe and CdSe NCs, and (e) AB_2 unit cell. (f-i) ico-AB_{13} superlattice of 8.8 nm PbSe (blue) and 3.8 nm CdSe (red) NCs (1/8th unit cell) with (f) TEM image interpolated from 0.54 nm/px along (001) direction at zero tilt, (g) cross section parallel to [001] plane through PbSe (dark gray) and four nearest CdSe (light gray), (h) cross section parallel to [010] plane through PbSe and two nearest CdSe, and (i) 1/8th of ico-AB_{13} unit cell. (j-m) AB superlattice of 6.8 nm PbSe (blue) and 4.6 nm Au (yellow) NCs with (j) TEM image interpolated from 0.54 nm/px along (010) direction at zero tilt, (k) cross section through [010] plane of PbSe (dark gray) and Au (black), (l) cross section through [001] plane of PbSe and Au NCs, (m) and AB unit cell. The scale bars represent 20 nm.

Furthermore, we investigated lattices with AB_{13} stoichiometry (8.8 nm PbSe; 3.7 nm CdSe), which are most intriguing as two isomorphs exist. Previous TEM studies reported the occurrence of the cub-octahedral AB_{13} structure.[4, 7] Since this particular arrangement has a considerably lower filling fraction than the icosahedral AB_{13} isomorph, the suitability of the hard-sphere model[30] for the studied systems has been put into question. As in the previous reports, the TEM image (Figure 4.2f) may equally give the impression that the structure is cub-octahedral. In contrast, the numerical cross section in Figure 4.2g reveals that the four CdSe closest to the [001] lattice plane do not form a square. Instead, the CdSe quadrangle is elongated in one direction, alternating by 90° degrees between neighboring cells. The numerical cross section in Figure 4.2h slices through the PbSe and the two CdSe closest to the [010] lattice plane. The relative location of the CdSe NCs alternates by 90° between neighboring cells, as the CdSe are either being visible side by side or above each other. The observation of a 90° rotation in the CdSe arrangement between neighboring cells reveals without any doubt the icosahedral configuration. ET analysis on all other subregions shows that the densest AB_{13} structure, that is, the icosahedral isomorph, prevails. A flawed analysis based on TEM images may arise from the complexity of the ico-AB_{13} lattice with a layer-wise rotation of the CdSe "cross motif" along the projection axis. The structure depicted in Figure 4.2f is one ico-AB_{13} unit cell thick (Figure 4.2h), which corresponds to the projection of two by 90° rotated cells. Analogous to the AB_2 examples, the AB_{13} lattices are strongly contracted perpendicular to the support resulting in a distance of 1-2 nm between the PbSe NC cores in this direction. More details are provided in Figure 4.1c and appendix Table A4.3.

The last example presented in Figure 4.2j-m summarizes the crystallographic analysis of an AB superlattice formed by 6.9 nm PbSe and 4.6 nm Au NCs. Again, the TEM image (Figure 4.2j) is complex and prone to misinterpretation. The numerical cross sections parallel (Figure 4.2k, [010] plane) and perpendicular (Figure 4.2l, [001] plane) to the support film illustrate that a superlattice isostructural with CuAu (space group 123) is present. Most notably, the stacking perpendicular to the support film contains a 90 degree rotation between the first and second unit cell layer (Figure 4.2l) responsible for the complex TEM projection pattern. The examined AB superlattice was 2 to 3 unit cells thick. The lattice parameter did not vary by more than 4% between different regions. Interestingly, we find no contraction perpendicular to the support film as for the superlattices discussed above (see Figure 4.1d and appendix Table A4.1 for more details).

In NC superlattices, as in atomic crystals, entropy dictates and gives a lower bound on the number and types of crystallographic defects, such as NC vacancies and substitutions. Kinetic effects during the superlattice growth can, however, significantly increase their number. In Figure 4.3 and Figure 4.4 we illustrate that ET is, in contrast to 2D TEM and scattering methods, also extremely valuable to discern crystal defects. While the TEM images in Figure 4.3a,d,g suggest defect-free AB_2 superlattices, ET analysis reveals that

each region contains one or more crystallographic defects. For example, the 3D representations in Figure 4.3b,c show PbSe NC vacancies occupied by multiple CdSe NCs and a surface-adsorbed PbSe NC attached between the superlattice and the support film. Likewise, a numerical cross section through an AB_2 structure composed of PbSe and Au NCs (Figure 4.3e) and the corresponding 3D representation (Figure 4.3) clearly reveal a substitutional defect, almost invisible in the TEM image (Figure 4.3d) of the 3 unit cell thick specimen. Contrary to the fact that a PbSe NC has been replaced by a smaller Au NC, the lattice appears to be stretched around the point defect. The magnitude of displacement for the PbSe NCs is represented in Figure 4.3f as a color change from blue (on lattice) to green (~2.5 nm of lattice). One can envision that developments toward strain field mapping could bridge the gap between the 3D micro-colloidal[31] and 2D atomic[32] equivalent. Furthermore, quantifying defect densities by visual inspection (e.g., 3.6% Au NC vacancies were found in the AB_2 lattice), or even better by automated routines, seems an obvious extension for the future.

Besides point defects, plane defects and order/disorder transitions could also be inferred by ET. For example Figure 4.3h,i displays 3D representations of a grain boundary parallel to the support surface, characterized by a horizontal shift by half a unit cell. Likewise, in AB lattices the above-mentioned rotation of the unit cell over 90° from layer to layer (Figure 4.2l) was detected. Moreover, NCs randomly adsorbed on the top or bottom surface can significantly obstruct TEM imaging of an underlying lattice. This situation is exemplified in Figure 4.3j, presenting a TEM image that suggests a disordered NC film. ET slices reveal, however, that this is due to one layer of surface adsorbed NCs (Figure 4.3k) on the bottom surface of a defect-free AB superlattice (Figure 4.3l). Alternatively, electron diffraction or analysis of the TEM image by fast Fourier transform will expose the underlying lattice periodicity but not the disordered layer as shown in Figure 4.3k. Additional examples of crystallographic defects can be found in Figure 4.4. Figure 4.4a-c present the transition from a disordered to ordered region in three layers of PbSe NCs in an AB_2 lattice. The propensity for the PbSe to form single component lattices is evident in Figure 4.4d-e. The PbSe in the AB_2 lattice of PbSe and Au NCs show a demixed PbSe pyramid inside the lattice. Figure 4.4g-l shows intracrystalline and surface adsorbed PbSe NCs on an AB_{13} lattice. The final defect observed is grain boundaries between individual AB_{13} crystallites composed out of PbSe and CdSe NCs as given in Figure 4.4m-n.

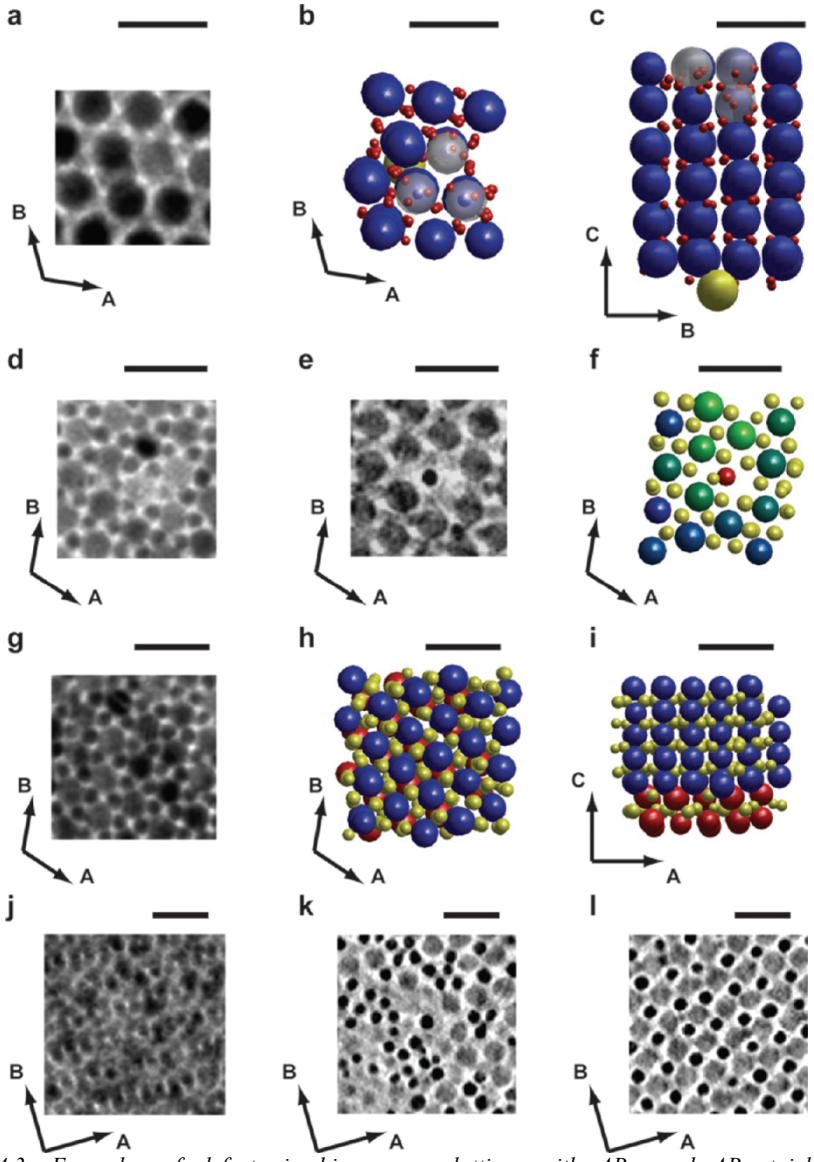

Figure 4.3: Examples of defects in binary superlattices with AB_2, and AB stoichiometry. Corresponding panels show TEM image interpolated from 0.54 nm/px (left) and ET analysis (center and right) of same region. (a) TEM image AB_2 of PbSe and CdSe along (001) direction at zero tilt, (b,c) ET analysis with PbSe in blue, CdSe in red, substituted PbSe in semitransparent white, and surface adsorbed PbSe in yellow. (d) TEM image AB2 of PbSe and Au along (001) direction at zero tilt, (e) numerical cross section through reconstruction parallel to imaging plane with Au substitution in black and stretched PbSe lattice in dark gray, (f) ET analysis with PbSe color coded relative to displacement from lattice (blue) on lattice, green) 2.5 nm of lattice), Au on lattice in yellow and PbSe substitution in red. (g) TEM image AB_2 of PbSe and Au along (001) direction at zero tilt, (h,i) ET analysis with PbSe in blue, red and Au in yellow showing grain boundary parallel to support. (j) TEM image AB of PbSe and Au along (010) direction at zero tilt, (k) numerical cross section parallel to the imaging plane through first layer from support, (l) second layer from support with Au in black and PbSe in dark gray. The scale bars represent 20 nm.

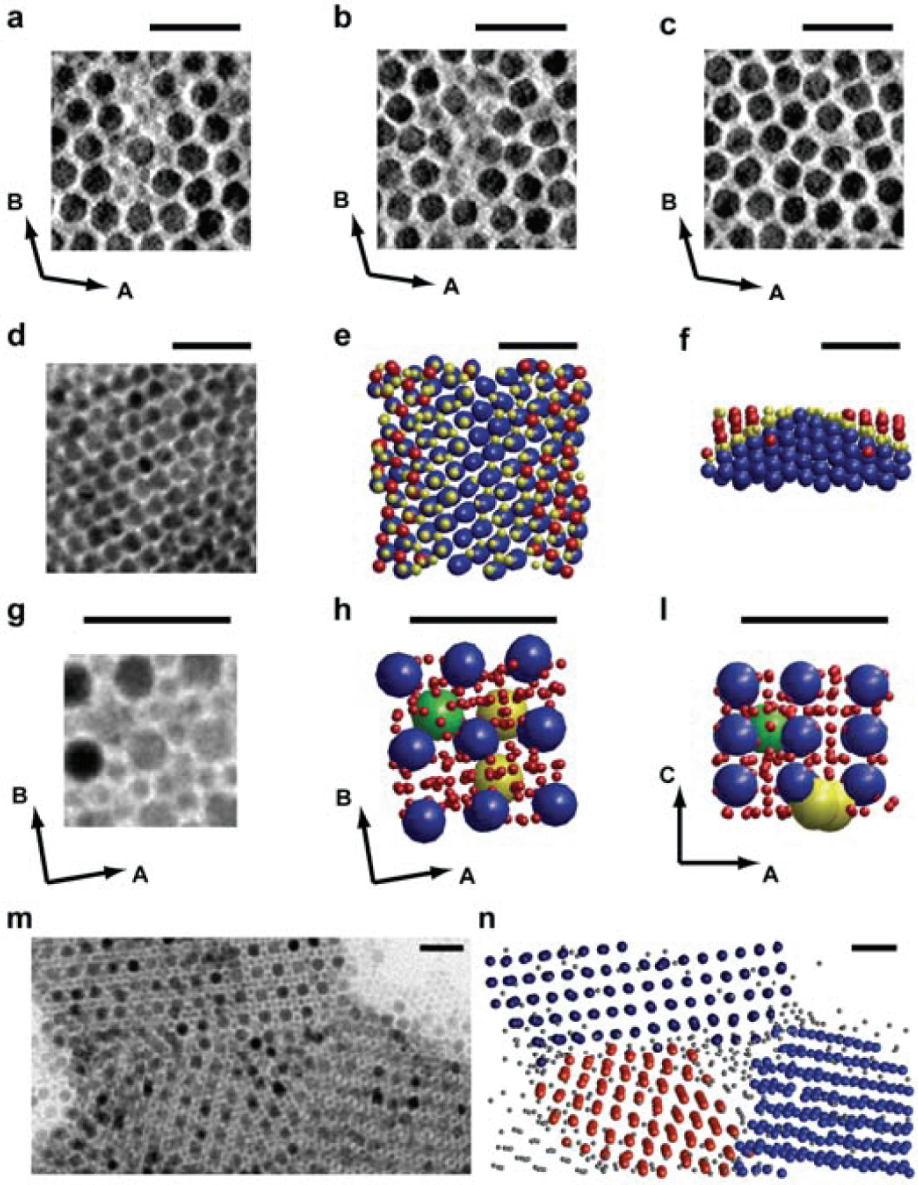

Figure 4.4: Examples of lattice defects in binary nanoparticle superlattices with AB_2, AB_{13} an AB stoichiometry. (a-c) ET slices through AB_2 consisting of PbSe and CdSe NCs showing disorder/order transition between first (a), second (b) and third (c) PbSe layer from surface. (d-f) demixed region (ROI4 in Figure 4.1d) in AB_2 of PbSe and Au NCs with (d) TEM image, (e,f) ET analysis showing demixed PbSe pyramid in blue, additional PbSe in red and Au in yellow. (g-l) AB_{13} of PbSe and CdSe NCs with (g) TEM image, (h,l) ET analysis showing PbSe blue, CdSe in red, intracrysalline PbSe in green and surface-adsorbed PbSe in yellow. (m,n) intergrowth of multiple AB_{13} crystallites consisting of PbSe and CdSe NCs with (m) TEM image, (n) ET analysis showing three PbSe lattices in black, blue, orange and PbSe off lattice in gray. The scale bars represent 30 nm.

Furthermore, being able to study the top and bottom surfaces by ET can give important information regarding the nucleation and growth mechanism. Figure 4.5 shows a TEM image of the AB_{13} and a TEM image of the AB_2 superlattice together with three numerical cross sections perpendicular to the support film each. The top of each cross section (Figure 4.5b-d, f-h) corresponds to the suspension/air interface, the bottom to the suspension/support boundary. It can be seen that the top region of the sections is mainly well ordered, while the bottom displays surface-adsorbed NCs (Figure 4.5c) and unfinished NC layers (Figure 4.5d). An unfinished layer means in this context that PbSe NCs are present in crystallographic positions in the fourth layer from the top while not all positions in the fourth layer are occupied by PbSe NCs. Similar observations can be made for the AB_2 lattices given in Figure 4.5e-h. Overall the top crystal layers are mainly well-ordered and continuous while step edges and disordered layers are found toward the bottom of the lattices. This provides strong evidence that the nucleation of the binary NC superlattices was not initiated at the support/suspension interface. A very recent study concluded that superlattices crystallize at the suspension/air interface and then deposit as a floating interfacial layer onto the substrate.[33] Reports of experiments with casted drops of NC suspensions support this notion.[34] Likewise, microcolloid crystallization induced by evaporating the solvent can also be initiated at the solvent/air interface.[35] The superlattice most likely has grown laterally along the interface and downward during further evaporation of the solvent. Superlattice growth becomes “confined” when the bottom surface gets close to the support film. In this view, the bottom lines of the perpendicular intersections provide indications of the superlattice growth close to a wall when the NCs were depleted. The contraction of the superlattice in the direction perpendicular to the support film is then tentatively explained by an anisotropic response to forces of the evaporating solvent retracting through the superlattice during drying.[33, 36] Regarding the possible use of NC superlattices, we anticipate that, for example, anisotropic lattice contractions and layer-wise rotations of the unit cell must have a dramatic effect on charge carrier generation and transport.

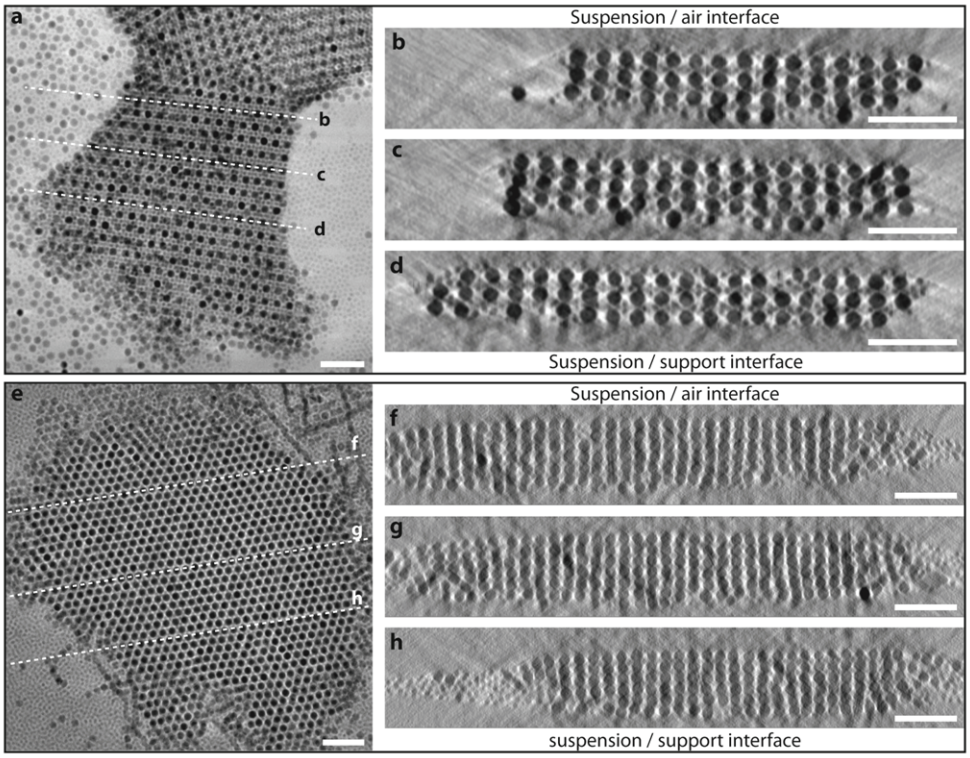

Figure 4.5: Structure of top and bottom surfaces in an AB_{13} and an AB_2 superlattice consisting of PbSe and CdSe NCs. (a) TEM image of the AB_{13} superlattice along the (001) direction at zero tilt with positions of numerical cross sections perpendicular to the imaging plane indicated by the dashed b, c and d lines. (b-d) Numerical cross sections perpendicular to the support. The top surface, that is, the suspension/air interface, is well ordered, while the bottom surface, that is, the suspension/support interface, shows surface-adsorbed PbSe (c) and unfinished NC layers (d). (e) TEM image of the AB_2 superlattice along the (001) direction at zero tilt with positions of numerical cross sections perpendicular to the imaging plane indicated by the dashed f, g and h lines. (f-h) Numerical cross sections perpendicular to the support. The scale bars represent 50 nm.

4.3.2 Electron tomography resolves a complex and novel crystal structure in a nanocrystal assembly

Previous work on the combination of PbSe and CdSe NCs showed that the driving force behind the NCSL formation can be understood in terms of the hard-sphere model, i.e. crystal structure formation driven by entropy only (see chapter 2).[14] According to this hard-sphere model there is a size ratio range ($0.63 \leq R_{CdSe}/R_{PbSe} \leq 0.75$) where only the single-component NCSL are stable, and no binary crystal structures are expected. However, we observed small areas of binary NCSL in this range, showing complex and variable TEM patterns (some of them being displayed in Figure 4.6) that could not be assigned to any known crystal structure. Thus, already from a purely crystallographic viewpoint, the determination of the crystal structures found here is of interest. Moreover, resolving these

structures will also show if there are binary NCSLs - stable in the hard-sphere framework - that due to their complexity escaped the attention of theoreticians. We will show that three different unresolved TEM projections reflect, in fact, the same complex crystal structure, whereby a straightforward analysis was hindered by planar rotations and misorientations. To the best of our knowledge, the observed superlattice crystal structure with a stoichiometry PbSe:CdSe of 6:19 has no reported analogue in atomic lattices.

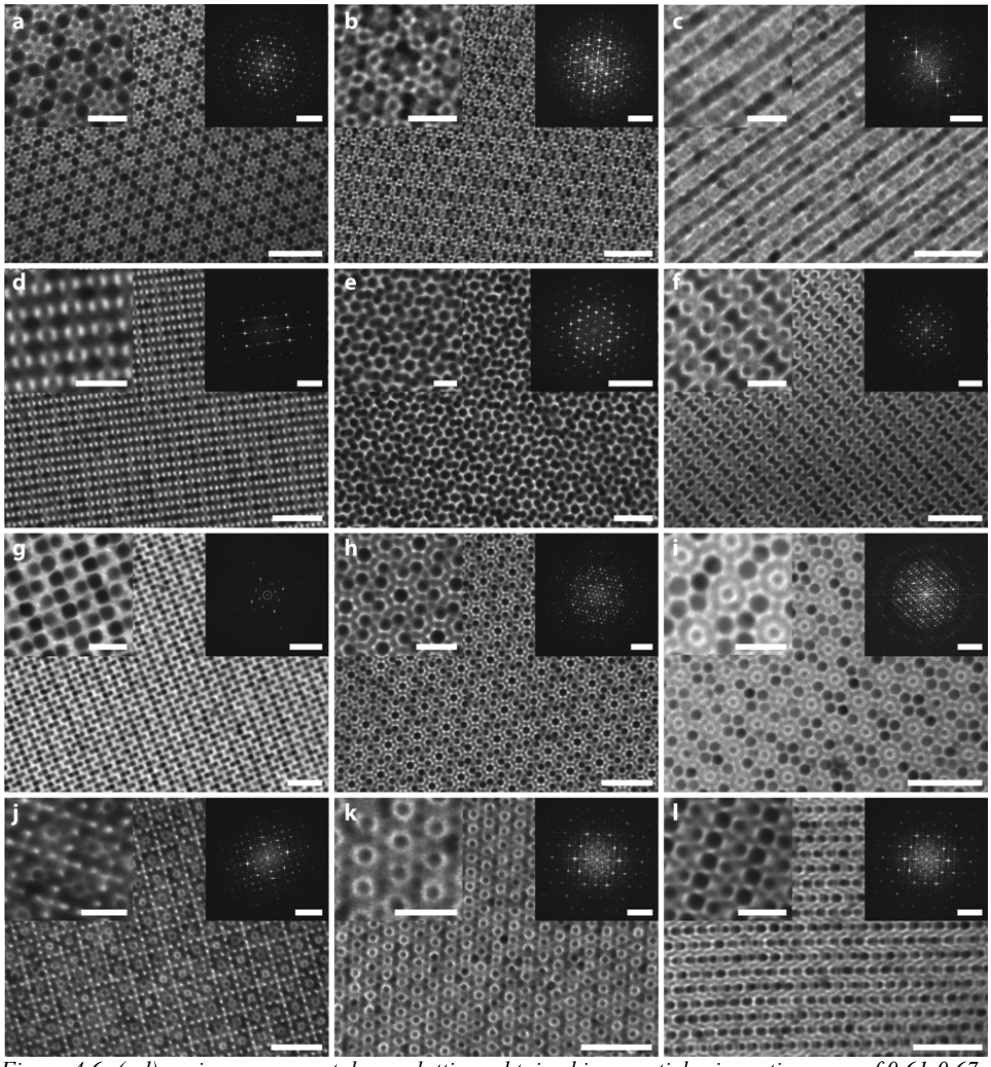

Figure 4.6: (a-l) various nanocrystal superlattices obtained in a particle size ratio range of 0.61-0.67. (a-c)are analysed using electron tomography and are further discussed in this section. (a) structure showing clear hexagonal symmetry. (b) structure showing less clear hexagonal symmetry and (c) showing repetitions in 2 direction, no sign of hexagonal symmetry. (d-l) as of yet unknown lattices or projections. The inset on the top left corners of the overview images represent zoomed-in images, while the insets on the top right show FFT transforms. The scale bars of the overview images, zoomed in insets and FFT transforms represent 50 nm, 20 nm and 0.2 nm^{-1} respectively.

Different TEM images of binary nanocrystal superlattices formed by the PbSe and CdSe NCs at a size-ratio range of 0.61-0.67 are given in Figure 4.6 of which Figure 4.6a-c are analyzed with electron tomography and are further discussed in this chapter. Figure 4.6a shows a clear hexagonally symmetric structure (hence forth labeled as structure 1), as is also confirmed by the clear pattern in the FFT (inset). The image in Figure 4.6b (structure 2) shows features that are less sharp, resulting in a much more diffuse FFT. However, still a hexagonal symmetry is observed. Figure 4.6c shows a superlattice (structure 3) that is under such an angle with the surface that almost no information about the structure can be extracted from the TEM image. From these TEM images it should be concluded that at this size-ratio, PbSe and CdSe form many different superlattices showing that the superlattice formation at these size ratios is very different from our findings in other size-ratio regions where the same system of nanocrystals leads to one or two binary crystal structures which are in accordance with the hard-sphere model. Furthermore, we should realize that these complex TEM images on themselves do not allow assigning a trustful crystal structure to the self-assembled arrays.

Using electron tomography and computer-aided particle detection the average unit cell vectors for structure 1 can be estimated. The position of the larger PbSe NCs is relatively easy to find since the strong electron scattering of the heavy Pb atoms results in high image contrast. The large size of the PbSe NCs further facilitates the particle detection. Using the particle detection method as described in the experimental section, the positions of 466 individual PbSe NCs were determined. The unit vector distance between each of them was calculated and used to transpose all particles into one unit cell (Figure 4.7). This unit cell was then used to determine the relative positions of the smaller CdSe NCs. For the CdSe NCs 1852 positions were determined. The relative distance to the unit cell's origin was used to transpose all determined positions into one unit cell. After this their average position within the unit cell was calculated. The CdSe NCs are much harder to detect due to their smaller size and lower contrast in TEM – Cd is a much weaker electron scatterer than Pb. This results into a wider spread in the detected Cd positions. The final crystal structure is presented in Figure 4.7, the coordinates are given in the appendix 4.2. The structure has the remarkable stoichiometry of PbSe:CdSe 6:19. Looking at the structure in more detail (Figure 4.7), it is seen that the PbSe NCs form an ABA stacking of equivalent kagome-like lattices with the A and B layers rotated 30^{o} with respect to each other. The CdSe NCs form an ABCBA stacking of three different hexagonally symmetric layers. Here A and C are in the same plane as the PbSe layers, and B occupies both fcc and hcp positions in between A and C. The total volume of the unit cell is 5365 nm^3. Using the inorganic core radius of the NCs this results in a packing fraction of 23%. However, when using the effective radius of the NCs we find a packing fraction of 85%. This dense stacking suggests that the crystal structure might be stable in the hard-sphere framework. Initial attempts to test the stability of the crystal structure in the hard-sphere model by Monte-Carlo methods were hampered by the large number of particles in one unit cell. However, statistical analysis of a large

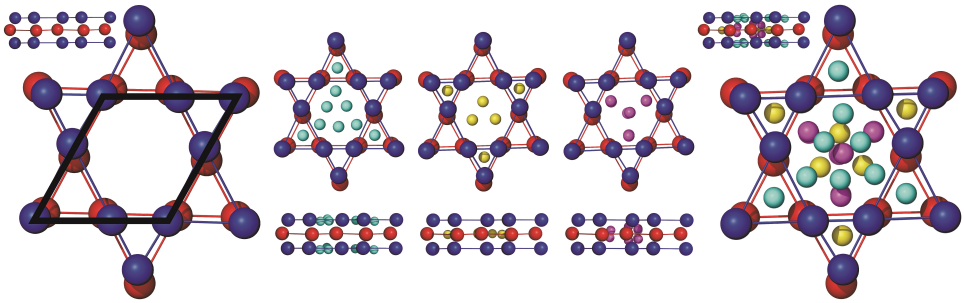

Figure 4.7: The A_6B_{19} unicell. Left: The PbSe positions form an ABA stacking of a kagome-like structure with layer B rotated 30° w.r.t. layer A. The primitive unit cell is indicated by the black trapezoid. Centre: The CdSe positions form three different layers. The first layer is in the same plane as the PbSe NCs positions indicated in blue, with one position inside the large blue triangles and 6 positions forming a triangle inside the blue hexagon. The second layer is in plane with the PbSe positions indicated in red, with one position inside the large red triangles and 3 positions forming a triangle inside the red hexagon. The third layer is located in between the PbSe layers and consists of 4 positions, with the middle one in an fcc position with respect to the layer below and above, and the other three positions arranged triangular around it occupying hcp positions with respect to the layers below and above. Right: The total structure. Note that the spheres are not drawn to scale for better visibility.

number of simulation cycles shows the predominant formation of a jammed phase with a packing fraction of 66.5% closely resembling the crystal structure.

Analyzing the electron tomogram of structure 2 (Figure 4.6b) directly shows the added value of electron tomography: a comparison of the reconstruction slices of the electron tomograms of structure 1 and structure 2 readily shows that they are actually the same structure in disguise (Figure 4.8). What makes the TEM images so different however (compare Figure 4.6a and b), is that a planar defect runs through the middle of structure 2. This planar defect is in fact a stacking fault where the next kagome structure of PbSe NCs was rotated over 180° (rather than 30°) and translated by the small PbSe-PbSe distance over both the in-plane unit cell axes. Since the planar defect is located roughly in the middle of the crystal, both parts contribute equally to the scattering of the electron beam. This results in a TEM picture showing a complicated pattern misleadingly pointing to two different crystal structures in Figure 4.6a and b.

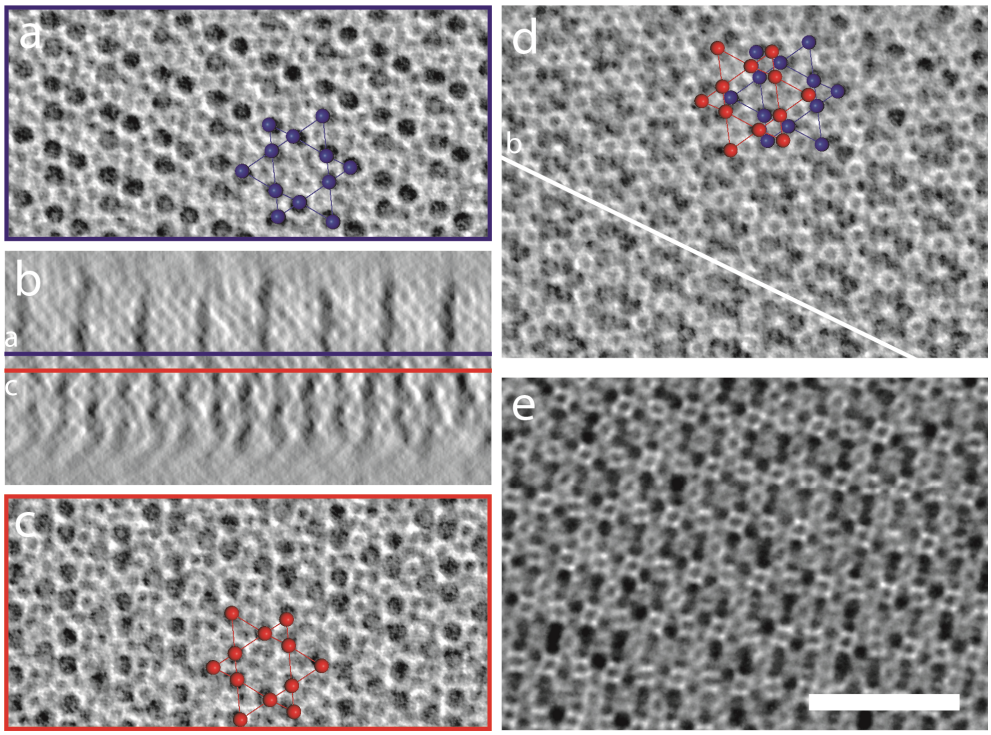

Figure 4.8: Reconstruction slices of structure 2. a,c Horizontal slices taken from the reconstruction along the first PbSe layer (a, blue) and (b, red) the planar defect, with the PbSe kagome structure indicated. b, Shows the positions of the horizontal slices indicated in a vertical slice through the reconstruction in d. d, An average of the two horizontal slices with the two different oriented and displaced PbSe layers shown. The white line indicates the direction along which the vertical slice for panel b was taken. e, Shows the original TEM image of structure 2. The scale bar represent 50 nm.

The thirds structure analyzed (Figure 4.6c) was also identified to be of the same crystal lattice as the previous two structures. The structure found was built up from the same kagome-like layers of PbSe, with the difference that these layers are stacked under an angle of 43° with respect to the substrate. Figure 4.9 shows the difference in the orientation of structure 1 and 3 where red indicates the orientation of structure 1 while the blue structure represents the lattice found for structure 3. In earlier work by Smith *et al.*[33] and Friedrich *et al.*[17] (see part of section 4.3.1) drying forces resulting in strong compression in the direction of the surface normal were observed. In the present case however, it seems that the drying forces resulted in a lamellar offset of the different PbSe layers, hinting towards stronger intra-layer interactions than interlayer interactions, something that could also account for the stacking fault in structure 2. The lamellar distortion does not significantly influence the unit cell's volume, which is only 5.8% larger than the unit cell volume for structure 1. However, combined with the difference in orientation with respect to the electron beam it makes a trustful interpretation of the TEM image (Figure 4.6c) impossible.

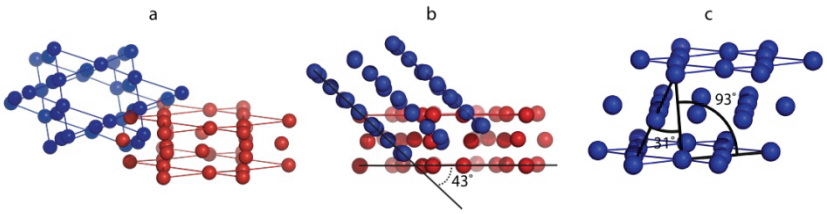

Figure 4.9: Reconstructuion of strucure 3. a, Comparison of the distorted structure 3 (blue) with structure 1 (red). b, The same layered kagome structure of the PbSe NCs is formed, but the layer stacking direction is rotated 43° with respect to the stacking direction of structure 1. c, Drying forces acting on the crystal resulted in a lamellar displacement of the different PbSe layers.

4.4 Conclusion

In conclusion, we have shown that electron tomography and image analysis can achieve single NC detection and, thus, is an indispensable method for a quantitative in depth real space study of (binary) nanocrystal superlattices. ET provides accurate lattice parameters of a given superlattice, unambiguously revealing the crystal structure including possible distortions. Moreover, for mixtures of PbSe and CdSe nanoparticles with a size ratio of 0.67, which form many complex crystal structures with unknown stoichiometry, we identified three different and complex TEM images to be of the same A_6B_{19} stoichiometry. In addition, real space analysis already has given clues to crystal nucleation and growth mechanisms. We believe that, the ability to detect defects and their effect on the surrounding lattice will be instrumental in a microscopic understanding of emerging materials properties.[9, 37, 38] We also anticipate that, as for the microcolloid equivalent where quantitative 3D optical microscopy on a single particle level has led to new insights into fundamental problems such as the glass transition,[39-41] crystallization[31] and determination of interparticle potentials,[42] electron tomography will be instrumental in providing similar insights in superlattices with nanometer scale periodicity.

References

1. Talapin, D. V.; Lee, J.-S.; Kovalenko, M. V.; Shevchenko, E. V. *Chemical Reviews* **2010,** 110, 389-458.
2. Rogach, A. L.; Talapin, D. V.; Shevchenko, E. V.; Kornowski, A.; Haase, M.; Weller, H. *Advanced Functional Materials* **2002,** 12, (10), 653-664.
3. Vanmaekelbergh, D. *Nano Today* **2011,** 6, (4), 419-437.
4. Overgaag, K.; Evers, W.; de Nijs, B.; Koole, R.; Meeldijk, J.; Vanmaekelbergh, D. *Journal of the American Chemical Society* **2008,** 130, (25), 7833-7835.
5. Redl, F. X.; Cho, K. S.; Murray, C. B.; O'Brien, S. *Nature* **2003,** 423, (6943), 968-971.
6. Kiely, C. J.; Fink, J.; Brust, M.; Bethell, D.; Schiffrin, D. J. *Nature* **1998,** 396, (6710), 444-446.
7. Shevchenko, E. V.; Talapin, D. V.; O'Brien, S.; Murray, C. B. *Journal of the American Chemical Society* **2005,** 127, (24), 8741-8747.
8. Chen, Z.; Moore, J.; Radtke, G.; Sirringhaus, H.; O'Brien, S. *Journal of the American Chemical Society* **2007,** 129, (50), 15702-15709.
9. Urban, J. J.; Talapin, D. V.; Shevchenko, E. V.; Kagan, C. R.; Murray, C. B. *Nature materials* **2007,** 6, (2), 115-121.
10. Shevchenko, E. V.; Talapin, D. V.; Kotov, N. A.; O'Brien, S.; Murray, C. B. *Nature* **2006,** 439, (7072), 55-59.
11. Talapin, D. V.; Shevchenko, E. V.; Bodnarchuk, M. I.; Ye, X.; Chen, J.; Murray, C. B. *Nature* **2009,** 461, 964-7.
12. Ye, X.; Chen, J.; Murray, C. B. *Journal of the American Chemical Society* **2011,** 133, 2613-20.
13. Bodnarchuk, M. I.; Shevchenko, E. V.; Talapin, D. V. *Journal of the American Chemical Society* **2011,** 133, 20837-49.
14. Evers, W. H.; Nijs, B. D.; Filion, L.; Castillo, S.; Dijkstra, M.; Vanmaekelbergh, D. *Nano Letters* **2010,** 10, (10), 4235-4241.
15. Midgley, P. A.; Weyland, M. *Ultramicroscopy* **2003,** 96, 413-31.
16. Friedrich, H.; de Jongh, P. E.; Verkleij, A. J.; de Jong, K. P. *Chemical Reviews* **2009,** 109, 1613-29.
17. Friedrich, H.; Gommes, C. J.; Overgaag, K.; Meeldijk, J. D.; Evers, W. H.; de Nijs, B.; Boneschanscher, M. P.; de Jongh, P. E.; Verkleij, A. J.; de Jong, K. P.; van Blaaderen, A.; Vanmaekelbergh, D. *Nano Letters* **2009,** 9, 2719-24.
18. Evers, Wiel H.; Friedrich, H.; Filion, L.; Dijkstra, M.; Vanmaekelbergh, D. *Angewandte Chemie International Edition* **2009,** 48, (51), 9655-9657.
19. Florea, I.; Demortière, A.; Petit, C.; Bulou, H.; Hirlimann, C.; Ersen, O. *ACS Nano* **2012,** 6, 2574-81.
20. Bals, S.; Casavola, M.; van Huis, M. A.; Van Aert, S.; Batenburg, K. J.; Van Tendeloo, G.; Vanmaekelbergh, D. *Nano Letters* **2011,** 11, 3420-4.
21. Houtepen, A. J.; Koole, R.; Vanmaekelbergh, D.; Meeldijk, J.; Hickey, S. G. *Journal of the American Chemical Society* **2006,** 128, (21), 6792-6793.
22. de Mello Donegá, C.; Hickey, S. G.; Wuister, S. F.; Vanmaekelbergh, D.; Meijerink, A. *The Journal of Physical Chemistry B* **2003,** 107, (2), 489-496.
23. Moreels, I.; Lambert, K.; De Muynck, D.; Vanhaecke, F.; Poelman, D.; Martins, J. C.; Allan, G.; Hens, Z. *Chemistry of Materials* **2007,** 19, (25), 6101-6106.
24. Yu, W. W.; Qu, L.; Guo, W.; Peng, X. *Chemistry of Materials* **2003,** 15, (14), 2854-2860.
25. Liu, X.; Atwater, M.; Wang, J.; Huo, Q. *Colloids and Surfaces B: Biointerfaces* **2007,** 58, (1), 3-7.
26. Frank, J., *Electron Tomography: Three dimensional imaging with the transmission electron microscope*. Plenum Press: New York, 1992.
27. Deans, S. R., *The radon transform ans some of its applications*. Wiley & Sons: New York, 1983.
28. Midgley, P. A.; Ward, E. P. W.; Hungria, A. B.; Thomas, J. M. *Chemical Society reviews* **2007,** 36, (9), 1477-1494.

29. Kremer, J. R.; Mastronarde, D. N.; McIntosh, J. R. *Journal of Structural Biology* **1995,** 116, 71-76.
30. Eldridge, M. D.; Madden, P. A.; Frenkel, D. *Nature* **1993,** 365, (6441), 35-37.
31. Schall, P.; Cohen, I.; Weitz, D. A.; Spaepen, F. *Nature* **2006,** 440, (7082), 319-323.
32. Hytch, M. J.; Snoeck, E.; Kilaas, R. *Ultramicroscopy* **1998,** 74, 131-146.
33. Smith, D. K.; Goodfellow, B.; Smilgies, D.-M.; Korgel, B. A. *Journal of the American Chemical Society* **2009,** 131, (9), 3281-3290.
34. Bigioni, T. P.; Lin, X.-M.; Nguyen, T. T.; Corwin, E. I.; Witten, T. A.; Jaeger, H. M. *Nature materials* **2006,** 5, (4), 265-270.
35. Li, W.; Fu, T.; He, S. *Materials Science and Engineering: A* **2006,** 441, (1-2), 239-244.
36. Klotz, M.; Albouy, P.-A.; Ayral, A.; Ménager, C.; Grosso, D.; Van der Lee, A.; Cabuil, V.; Babonneau, F.; Guizard, C. *Chemistry of Materials* **2000,** 12, (6), 1721-1728.
37. Gur, I.; Fromer, N. A.; Geier, M. L.; Alivisatos, A. P. *Science* **2005,** 310, (5747), 462-465.
38. Talapin, D. V.; Murray, C. B. *Science* **2005,** 310, (5745), 86-89.
39. van Blaaderen, A.; Wiltzius, P. *Science* **1995,** 270, (5239), 1177-1179.
40. Weeks, E. R.; Crocker, J. C.; Levitt, A. C.; Schofield, A.; Weitz, D. A. *Science* **2000,** 287, (5453), 627-631.
41. Kegel, W. K.; van Blaaderen, A. *Science* **2000,** 287, (5451), 290-293.
42. Royall, C. P.; Leunissen, M. E.; Blaaderen, A. v. *Journal of Physics: Condensed Matter* **2003,** 15, S3581-S3596.

Appendix 4.1 ET tables of the ROI of the AB, AB_2 and AB_{13} lattices

Table A4.1: ET analysis of AB_2 consisting of PbSe and CdSe NCs.

Particle size distribution and shell thickness (normal distribution) in nm

Region	PbSe d_{core}	PbSe t_{min}	PbSe t_{3NN}	CdSe d_{core}	CdSe t_{min}	CdSe t_{3NN}
ROI 1	9.0 ± 0.3	-0.3 ± 0.7*	0.5 ± 0.5	3.4 ± 0.5	1.1 ± 0.4	1.4 ± 0.3
ROI 2	9.0 ± 0.3	-0.4 ± 0.9*	0.5 ± 0.6	3.4 ± 0.5	1.2 ± 0.4	1.5 ± 0.3
ROI 3	9.0 ± 0.3	-0.4 ± 0.7*	0.5 ± 0.5	3.4 ± 0.5	1.1 ± 0.3	1.5 ± 0.2
ROI 4	9.0 ± 0.3	-0.4 ± 0.7*	0.5 ± 0.6	3.4 ± 0.5	1.1 ± 0.4	1.4 ± 0.3

Unitcell vector length and average displacement (rms) from lattice in nm

Region	A (nm)	B (nm)	C (nm)	Volume
ROI 1	11.2 ± 0.8	11.7 ± 0.6	8.4 ± 1.0	956
ROI 2	11.6 ± 0.7	11.4 ± 0.7	8.4 ± 0.9	982
ROI 3	11.2 ± 0.7	11.5 ± 0.6	8.4 ± 0.9	970
ROI 4	11.4 ± 0.6	11.7 ± 0.6	8.0 ± 1.1	928

Unit cell vector angles in degrees

Region	AB (°)	BC (°)	CA (°)
ROI 1	119.9	91.7	88.8
ROI 2	117.8	90.0	90.5
ROI 3	116.2	91.1	88.5
ROI 4	118.4	86.4	90.3

Unit cell filling fraction (ρ) and size ratio (γ)

Region	ρ (d_{core})	ρ ($d_{core} + t_{min}$)	ρ ($d_{core} + t_{3NN}$)	γ (d_{core})	γ ($d_{core} + t_{min}$)	γ ($d_{core} + t_{3NN}$)
ROI 1	0.439	0.451	0.586	0.379	0.517	0.508
ROI 2	0.428	0.439	0.584	0.376	0.533	0.512
ROI 3	0.436	0.448	0.587	0.374	0.520	0.507
ROI 4	0.458	0.466	0.614	0.368	0.512	0.497

CdSe postion (mean ± std) in unit cell of ROI2 expressed in multiples A, B, C

	A	B	C
CdSe1	0.34 ± 0.05	0.69 ± 0.06	0.51 ± 0.11
CdSe 2	0.63 ± 0.05	0.28 ± 0.06	0.49 ± 0.09

* A negative minimum neighbour distance (t_{min}) which could be interpreted as penetration of the NC hard cores is unphysical. Instead it results from analyzing NC as spherical objects which only approximates the actual shape of a facetted crystallite.

Table A4.2: ET analysis of AB_2 consisting of PbSe and Au NCs.

Particle size distribution and shell thickness (normal distribution) in nm

Region	PbSe d_{core}	PbSe t_{min}	PbSe t_{3NN}	CdSe d_{core}	CdSe t_{min}	CdSe t_{3NN}
ROI 1	7.1 ± 0.4	0.2 ± 0.7*	0.8 ± 0.5	3.7 ± 0.4	0.9 ± 0.3	1.2 ± 0.2
ROI 2	7.1 ± 0.4	-0.2 ± 0.7*	0.5 ± 0.5	3.7 ± 0.4	0.9 ± 0.3	1.2 ± 0.2
ROI 3	7.1 ± 0.4	0.1 ± 0.7*	0.7 ± 0.5	3.7 ± 0.4	0.9 ± 0.3	1.2 ± 0.3

Unitcell vector length and average displacement (rms) from lattice in nm

Region	A (nm)	B (nm)	C (nm)	Volume
ROI 1	9.8 ± 0.4	10.1 ± 0.4	7.2 ± 0.4	630
ROI 2	10.2 ± 1.1	10.3 ± 0.9	6.5 ± 0.7	594
ROI 3	9.9 ± 0.4	10.0 ± 0.4	6.7 ± 0.8	581

Unit cell vector angles in degrees

Region	AB (°)	BC (°)	CA (°)
ROI 1	117.5	90.1	91.9
ROI 2	119.6	90.1	91.2
ROI 3	117.8	90.4	90.4

Unit cell filling fraction (ρ) and size ratio (γ)

Region	ρ (d_{core})	ρ (d_{core} + t_{min})	ρ (d_{core} + t_{3NN})	γ (d_{core})	γ (d_{core} + t_{min})	γ (d_{core} + t_{3NN})
ROI 1	0.388	0.502	0.616	0.524	0.633	0.628
ROI 2	0.408	0.469	0.593	0.525	0.662	0.641
ROI 3	0.410	0.506	0.626	0.522	0.645	0.634

CdSe postion (mean ± std) in unit cell of ROI2 expressed in multiples A, B, C

	A	B	C
CdSe1	0.33 ± 0.05	0.68 ± 0.05	0.52 ± 0.08
CdSe 2	0.65 ± 0.05	0.32 ± 0.05	0.51 ± 0.09

* A negative minimum neighbour distance (t_{min}) which could be interpreted as penetration of the NC hard cores is unphysical. Instead it results from analyzing NC as spherical objects which only approximates the actual shape of a facetted crystallite.

Table A4.3 ET analysis of AB_{13} consisting of PbSe and CdSe NCs.

Particle size distribution and shell thickness (normal distribution) in nm

Region	PbSe d_{core}	PbSe t_{min}	PbSe t_{3NN}	CdSe d_{core}	CdSe t_{min}	CdSe t_{3NN}
ROI 1	8.8 ± 0.3	0.1 ± 0.7*	0.5 ± 0.4	3.8 ± 0.4	0.6 ± 0.5	0.9 ± 0.3
ROI 2	8.8 ± 0.3	0.2 ± 0.4*	0.5 ± 0.3	3.8 ± 0.4	0.6 ± 0.4	0.9 ± 0.3
ROI 3	8.8 ± 0.3	0.1 ± 0.4*	0.4 ± 0.3	3.8 ± 0.4	0.5 ± 0.4	0.9 ± 0.3
ROI 4	8.7 ± 0.4	0.2 ± 0.7*	0.6 ± 0.4	3.6 ± 0.4	0.7 ± 0.5	1.1 ± 0.3
ROI 5	8.7 ± 0.3	0.2 ± 0.8*	0.7 ± 0.4	3.7 ± 0.4	0.6 ± 0.4	1.0 ± 0.3

Unitcell vector length and average displacement (rms) from lattice in nm

Region	A (nm)	B (nm)	C (nm)	Volume
ROI 1	14.0 ± 0.5	14.4 ± 0.6	10.2 ± 0.7	2059
ROI 2	13.7 ± 0.5	14.7 ± 0.4	9.8 ± 0.7	1978
ROI 3	13.7 ± 0.6	15.2 ± 0.4	10.0 ± 0.6	2081
ROI 4	13.9 ± 0.5	14.2 ± 0.6	11.1 ± 0.9	2187
ROI 5	13.8 ± 0.5	13.9 ± 0.7	11.2 ± 0.7	2053

Unit cell vector angles in degrees

Region	AB (°)	BC (°)	CA (°)
ROI 1	92.3	89.9	93.4
ROI 2	88.8	89.7	89.7
ROI 3	91.8	90.4	88.2
ROI 4	93.8	92.3	87.4
ROI 5	86.2	90.9	106.1

Unit cell filling fraction (ρ) and size ratio (γ)

Region	ρ (d_{core})	ρ ($d_{core} + t_{min}$)	ρ ($d_{core} + t_{3NN}$)	γ (d_{core})	γ ($d_{core} + t_{min}$)	γ ($d_{core} + t_{3NN}$)
ROI 1	0.358	0.459	0.555	0.433	0.491	0.512
ROI 2	0.373	0.488	0.583	0.432	0.486	0.510
ROI 3	0.347	0.437	0.530	0.433	0.488	0.514
ROI 4	0.307	0.413	0.513	0.416	0.479	0.502
ROI 5	0.331	0.435	0.543	0.422	0.483	0.500

* A negative minimum neighbour distance (t_{min}) which could be interpreted as penetration of the NC hard cores is unphysical. Instead it results from analyzing NC as spherical objects which only approximates the actual shape of a facetted crystallite.

Table A4.4: ET analysis of AB consisting of PbSe and Au NCs.

Particle size distribution and shell thickness (normal distribution) in nm

Region	PbSe d_{core}	PbSe t_{min}	PbSe t_{3NN}	CdSe d_{core}	CdSe t_{min}	CdSe t_{3NN}
ROI 1	6.8 ± 0.5	0.5 ± 0.6*	1.0 ± 0.5	4.6 ± 0.4	1.3 ± 0.3	1.6 ± 0.3
ROI 2	6.8 ± 0.4	0.5 ± 0.6*	1.0 ± 0.5	4.6 ± 0.4	1.3 ± 0.3	1.6 ± 0.3
ROI 3	6.9 ± 0.4	0.2 ± 0.4*	0.6 ± 0.3	4.6 ± 0.4	1.3 ± 0.3	1.6 ± 0.2
ROI 4	6.9 ± 0.4	0.6 ± 0.6*	1.0 ± 0.5	4.6 ± 0.5	1.2 ± 0.4	1.6 ± 0.4

Unitcell vector length and average displacement (rms) from lattice in nm

Region	A (nm)	B (nm)	C (nm)	Volume
ROI 1	10.9 ± 0.6	10.4 ± 0.5	10.5 ± 0.6	1187
ROI 2	10.6 ± 0.6	10.5 ± 0.5	10.6 ± 0.7	1175
ROI 3	10.7 ± 0.4	10.8 ± 0.4	10.5 ± 0.4	1222
ROI 4	10.4 ± 0.7	10.4 ± 0.4	11.0 ± 0.6	1174

Unit cell vector angles in degrees

Region	AB (°)	BC (°)	CA (°)
ROI 1	90.2	89.6	88.0
ROI 2	91.3	86.6	88.8
ROI 3	91.1	91.3	90.0
ROI 4	91.5	91.2	97.4

Unit cell filling fraction (ρ) and size ratio (γ)

Region	ρ (d_{core})	ρ ($d_{core} + t_{min}$)	ρ ($d_{core} + t_{3NN}$)	γ (d_{core})	γ ($d_{core} + t_{min}$)	γ ($d_{core} + t_{3NN}$)
ROI 1	0.224	0.353	0.420	0.682	0.824	0.808
ROI 2	0.226	0.352	0.420	0.670	0.797	0.791
ROI 3	0.224	0.332	0.384	0.662	0.824	0.813
ROI 4	0.221	0.345	0.410	0.647	0.765	0.768

PbSe and Au in face centred positions (mean ± std) in unit cell of ROI 3 expressed in multiples A, B, C

	A	B	C
Au1	0.02 ± 0.04	0.50 ± 0.03	0.53 ± 0.04
Au2	0.48 ± 0.05	0.49 ± 0.03	1.00 ± 0.05
Au3	0.98 ± 0.05	0.49 ± 0.03	0.53 ± 0.05
Au4	0.49 ± 0.04	0.50 ± 0.03	0.05 ± 0.05
PbSe 1	0.50 ± 0.05	1.00 ± 0.03	0.51 ± 0.05
PbSe 2	0.50 ± 0.05	0.01 ± 0.03	0.51 ± 0.03

* A negative minimum neighbour distance (t_{min}) which could be interpreted as penetration of the NC hard cores is unphysical. Instead it results from analyzing NC as spherical objects which only approximates the actual shape of a facetted crystallite.

Appendix 4.2: Unit cell parameters of the A_6B_{19} crystal structure

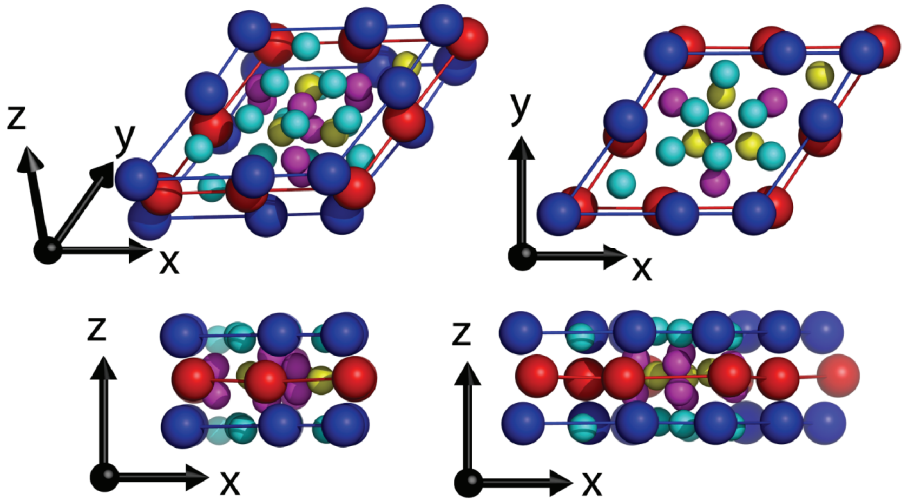

*Figure A4.1: Three dimensional, top and different side views of the detected unit cell. Balls with the same color depict nanocrystals within the same layer. PbSe nanocrystals are displayed in blue and red, CdSe nanocrystals in cyan, magenta and yellow. The unit vectors are defined as **a** along the x-axis, **b** in the xy plane and **c** along the z-axis.*

Table A4.5 The unit vectors a, b and c given in Cartesian coordinates.

Unit vector	x (nm)	y (nm)	z (nm)
a	22.4 ± 0.7	2.3 ± 0.8	-0.3 ± 0.7
b	9.4 ± 0.7	22.3 ± 0.6	0.2 ± 0.8
c	0.3 ± 0.9	-0.4 ± 0.9	11.2 ± 0.7

Table A4.6: The 25 unique nanocrystal positions within the unit cell given in both Cartesian coordinates and fractions of the unit vectors. Color coding refers to Figure A4.1.

Nanocrystal	x (nm)	y (nm)	z (nm)	**a**	**b**	**c**
PbSe (blue)	0.0 ± 0.7	0.0 ± 0.6	0.0 ± 0.8	0.00 ± 0.04	0.00 ± 0.03	0.00 ± 0.08
PbSe (blue)	13.0 ± 0.7	1.4 ± 0.7	-0.2 ± 0.6	0.58 ± 0.04	0.00 ± 0.03	0.00 ± 0.05
PbSe (red)	11.5 ± 0.7	2.0 ± 0.8	5.6 ± 0.8	0.49 ± 0.04	0.05 ± 0.04	0.51 ± 0.08
PbSe (blue)	5.7 ± 0.6	13.5 ± 0.9	0.2 ± 0.5	0.00 ± 0.03	0.61 ± 0.04	0.01 ± 0.05
PbSe (red)	5.7 ± 0.8	11.0 ± 1.0	5.5 ± 0.9	0.04 ± 0.04	0.50 ± 0.05	0.48 ± 0.08
PbSe (red)	1.4 ± 1.0	1.0 ± 1.1	5.8 ± 1.0	0.03 ± 0.05	0.05 ± 0.05	0.52 ± 0.09
CdSe (cyan)	6.1 ± 0.8	4.9 ± 0.9	0.6 ± 0.9	0.18 ± 0.03	0.20 ± 0.04	0.06 ± 0.08
CdSe (cyan)	11.4 ± 0.5	8.8 ± 0.8	0.5 ± 0.9	0.35 ± 0.03	0.36 ± 0.04	0.04 ± 0.08
CdSe (cyan)	17.1 ± 0.5	8.8 ± 0.9	-0.4 ± 0.5	0.62 ± 0.03	0.34 ± 0.04	-0.02 ± 0.04
CdSe (cyan)	22.9 ± 0.5	10.1 ± 0.7	0.3 ± 0.7	0.86 ± 0.03	0.37 ± 0.04	0.04 ± 0.06
CdSe (cyan)	13.9 ± 0.5	15.0 ± 1.1	-0.1 ± 0.6	0.34 ± 0.03	0.65 ± 0.05	-0.02 ± 0.06
CdSe (cyan)	20.1 ± 0.7	15.4 ± 0.8	0.1 ± 0.6	0.63 ± 0.04	0.63 ± 0.04	0.01 ± 0.06
CdSe (cyan)	16.8 ± 0.5	20.0 ± 1.0	0.3 ± 1.0	0.38 ± 0.03	0.87 ± 0.05	0.02 ± 0.09
CdSe (magenta)	16.7 ± 0.7	13.0 ± 0.7	2.6 ± 0.4	0.52 ± 0.03	0.53 ± 0.03	0.24 ± 0.04
CdSe (magenta)	11.3 ± 0.6	16.2 ± 0.8	3.5 ± 0.9	0.20 ± 0.03	0.71 ± 0.04	0.30 ± 0.07
CdSe (magenta)	17.5 ± 0.6	6.1 ± 0.8	3.9 ± 0.9	0.69 ± 0.03	0.21 ± 0.04	0.36 ± 0.08
CdSe (magenta)	22.3 ± 0.7	17.3 ± 0.9	3.9 ± 0.9	0.69 ± 0.03	0.71 ± 0.04	0.35 ± 0.08
CdSe (yellow)	27.7 ± 0.9	21.4 ± 0.9	5.6 ± 1.1	0.86 ± 0.05	0.88 ± 0.04	0.50 ± 0.10
CdSe (yellow)	13.7 ± 0.6	10.5 ± 0.6	5.5 ± 0.4	0.42 ± 0.02	0.44 ± 0.03	0.49 ± 0.04
CdSe (yellow)	16.6 ± 0.5	16.5 ± 0.9	5.4 ± 0.3	0.44 ± 0.03	0.70 ± 0.04	0.48 ± 0.04
CdSe (yellow)	20.9 ± 0.9	11.3 ± 0.8	4.9 ± 0.7	0.74 ± 0.05	0.44 ± 0.04	0.45 ± 0.06
CdSe (magenta)	17.5 ± 0.8	13.0 ± 0.9	8.0 ± 0.5	0.54 ± 0.04	0.54 ± 0.04	0.72 ± 0.05
CdSe (magenta)	11.3 ± 0.9	16.3 ± 1.2	7.6 ± 0.8	0.19 ± 0.04	0.72 ± 0.05	0.67 ± 0.07
CdSe (magenta)	17.6 ± 0.6	5.7 ± 0.8	6.8 ± 0.7	0.69 ± 0.03	0.19 ± 0.04	0.62 ± 0.06
CdSe (magenta)	22.4 ± 0.6	17.0 ± 0.8	7.3 ± 0.6	0.70 ± 0.03	0.70 ± 0.04	0.65 ± 0.05

Chapter 5

Dimensional control over oriented attachment of semiconductor nanocrystals

Oriented attachment, the process in which nanometre-sized crystals fuse by atomic bonding of specific crystal facets, is expected to be more difficult to control than nanocrystal self-assembly that is driven by entropic factors or weak van der Waals attractions. Here, we present a study of oriented attachment of PbSe nanocrystals contradict this intuitive prediction. The reaction was studied in a thin film of the suspension casted on an immiscible liquid at a given temperature. We report that attachment can be controlled such that it occurs with one type of facets exclusively. By control of the temperature and particle concentration we obtain one- or two-dimensional PbSe single crystals, the latter with a honeycomb or square super-imposed periodicity in the nanometer range. We demonstrate the ability to convert these PbSe superstructures into other semiconductor compounds with preservation of crystallinity and geometry.

5.1 Introduction

Oriented attachment, the connection of a nanometre sized crystal to another crystal via the atomic matching of opposing crystal facets, is an intriguing process that is important in crystal growth and bio-mineralization.[1-3] In bottom-up approaches that aim to produce extended and highly ordered nanostructures using wet chemistry, oriented attachment is increasingly employed to grow highly anisotropic semiconductor nanostructures.[4-9] This is enabled by the recent progress to synthesize colloidal nanocrystals with uniform size and shape and, hence, with well-defined crystal facets. The adsorption-desorption equilibria of the nanocrystal surfactant molecules, which are responsible for the colloidal stability, are specific for different nanocrystal facets.[10-12] This facet-specific surfactant adsorption can play a decisive role in which facet(s) becomes reactive in nanocrystal attachment, determining in this way the geometry of the resulting structures. In this respect, nanocrystals of the lead chalcogenide family have been studied extensively. By adding specific surfactant molecules or co-solvents to the nanocrystal suspension, specific crystallographic facets can be "activated" resulting in 1-D semiconductor nanowires in some cases, and 2-D sheets in other cases. Cho et al. reported the formation of μm-long PbSe wires at elevated temperature, formed by consecutive attachment of PbSe nanocrystals via their opposite {100} facets.[4] More recently, the formation of ultra-thin single crystalline PbS sheets initiated by addition of a Cl-containing co-solvent to the suspension was reported.[7] Since the resulting structures are either 1-D wires or 2-D sheets that are highly crystalline, oriented attachment could become a new approach for the fabrication of 1-D and 2-D semiconductors with importance for nanophysics and opto-electronic applications.

Oriented attachment of colloidal nanocrystals is different from nanocrystal self-assembly in the strength of the driving forces, being inter-atomic bonding in the first and van der Waals interactions or entropic factors in the second case.[13] It can hence be expected that oriented attachment is an irreversible aggregation process that is more difficult to control by the reaction conditions than nanocrystal self-assembly. Here we present results that counteract this intuitive assumption. We studied the oriented attachment of PbSe nanocrystals in a thin film of a suspension casted on an immiscible liquid at temperatures whereby the solvent evaporates. We show that, by variation of the nanocrystal concentration and the temperature, the symmetry of attachment can be varied from linear to two-dimensional and even to three-dimensional. In the two-dimensional case we are able to prepare ultra-thin sheets with a square and honeycomb superlattice structure. The resulting structures are suspended on the immiscible substrate liquid and can thus be transferred to any substrate of choice, which enables their incorporation in opto-electronic devices. Moreover, we demonstrate the ability to convert these rods and sheets to other compounds such as CdSe and $Cu_{2-x}Se$, opening the pathway to two-dimensional superlattices of a variety of semiconductor compounds.

5.2 Experimental

PbSe nanocubes: PbSe nanocubes were synthesized by a method described by Houtepen *et al.*[14] The synthesis was performed in a water and oxygen free environment. (1) 1.9 gram of lead acetate tri hydrate (99.999% Aldrich), 4 mL of diphenyl ether (99% DPE, aldrich), 3 mL of oleic acid (OA, 90% Aldrich) and 16 mL trioctyl phospine (TOP, 90% Fluka) were heated to 100 °C under low pressure (10^{-3} bar) for ~3 hours. (2) A second mixture containing 0.31 g Se (99.999% Alfa Aesar) and 4 mL TOP was prepared. Subsequently 11.5 mL of solution (1) and 1.7 ml of solution (2) was injected into 10 mL 190 °C DPE. The reaction mixture was kept at a constant temperature of 145 °C. After 30 seconds to 10 minutes the reaction mixture was quenched with 20 mL butanol and 10 mL methanol. The crude synthesis mixtures were washed twice by precipitating with methanol, centrifugation and redispersion of the sediment in toluene.
PbSe stars: In order to obtain PbSe "stars", the synthesis procedure was adapted as follows: During the first step in the PbSe nanocrystal synthesis, i.e. the preparation of Pb-oleate precursor, the precursor was only allowed to react for ~30 minutes. Hence a small amount of acetic acid remained in the precursor mixture. The acetic acid facilitates the growth of PbSe nanostars.[14]
PbSe rods: rods were prepared as follows: the Pb-oleate and TOP-Se precursors were prepared as described above. 9 ml of the Pb-oleate precursor solution was injected into 13 mL DPE at 190 °C. After one minute, 0.6 ml of the TOP-Se solution was injected and the reaction was allowed to proceed for 20 minutes at a constant temperature of 140 °C. Both quenching of the reaction and purification of the NCs were performed as described above.[15]

Oriented attachment was achieved by slow evaporation of the solvent from the nanocrystal suspension placed on top of ethylene glycol as an immiscible liquid substrate, at a given temperature (called the reaction temperature). In a typical experiment, 1 mL of ethylene glycol was placed in a glass vial (Ø 10 mm). After the desired temperature (between 20 and 140 °C) was reached, 50 µL of nanocrystal suspension was injected after which the solvent was allowed to evaporate, as depicted in Figure 5.1. The evaporation takes from 90 to 10 minutes. After evaporation a sample was taken from the ethylene glycol layer at the center of the vial and placed under vacuum to evaporate the residual ethylene glycol. All experiments were performed in a nitrogen purged glovebox.

The nanocrystals have been imaged using high angle annular dark field scanning transmission electron microscopy (HAADF-STEM) performed using a double aberration corrected FEI TITAN operated at 300kV. The semi convergence angle of the electron probe used during acquisition was 21.4 mrad. The TEM images were obtained with a FEI Tecnai 12.

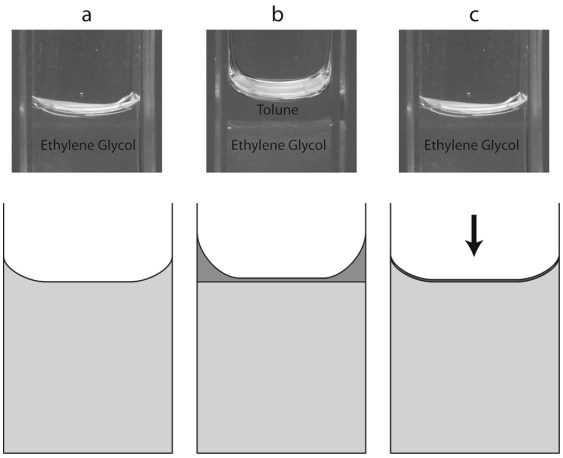

Figure 5.1: Cartoon of the evaporation process. Ethylene glycol is placed in a vial (A) after which the PbSe nanocrystal suspension is deposited on top of it (B). To illustrate the effect the amount of suspension has been increased tenfold in figure B. After the solvent is evaporated, a sample is taken in the centre of the vial at the air/liquid interface. The entire experiment takes place in a nitrogen purged glovebox.

5.3 Results and discussion

In the study of oriented attachment of PbSe nanocrystal, we have used suspensions of truncated PbSe nanocubes, nanorods and stars that are nearly uniform in size and shape. The only three parameters that we varied in the oriented attachment of PbSe NC were (i) the initial nanocrystal concentration in the suspension, (ii) the temperature at which the solvent was evaporated, and (iii) the concentration of oleic acid capping molecules that we added into the ethylene glycol substrate liquid. The shape and facets of the PbSe nanocubes and nanorods were investigated in detail with High Angle Annular Dark Field Scanning Transmission Electron Microscopy (HAADF-STEM). In Figure 5.2, two HAADF-STEM images are presented, obtained from PbSe nanocrystals with a diameter of 9.9 nm. Figure 5.2a and Figure 5.2b present images acquired with the electron beam oriented along the [110] axis and the [100] axis respectively. The edges of the projection can be identified as {100}, {011} and {111} facets. Figure 5.2c and d present intensity profiles taken along the direction indicated by the arrows in Figure 5.2a, showing a {100} → {110} → {100} sequence of facets in Figure 5.2 c and a {111} → {110} → {111} sequence in Figure 5.2d. These results are in line with a truncated nanocube model (see inset) with 6 {100} initial planes, 12 {110} planes and 8 {111} planes. The size of the nanocubes varied between 4 and 10 nm, where the truncation of the smaller NCs is more pronounced then the truncation of the larger NCs. In appendix 5.3 a model for the NC geometry is presented. A similar study was performed for PbSe nanorods as shown in Figure 5.3. It was found that the tips of the nanorods yield a smooth {100} termination whereas the long facets are roughened {100} and {110} facets.

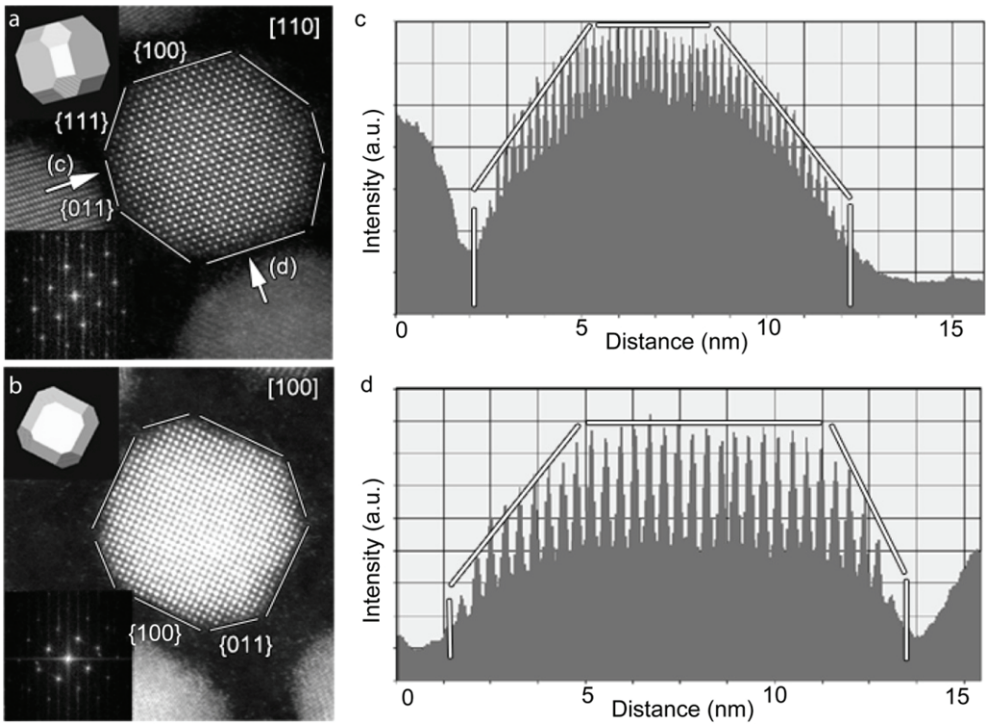

Figure 5.2: High resolution HAADF-STEM image of PbSe nanoparticle oriented along the [110] zone axis a, and along the [100] zone axis b. Both the outer shapes of the 2-D projection images and the intensity profiles c,d corresponds to our model of a cube with truncated {110} and {111} facets.

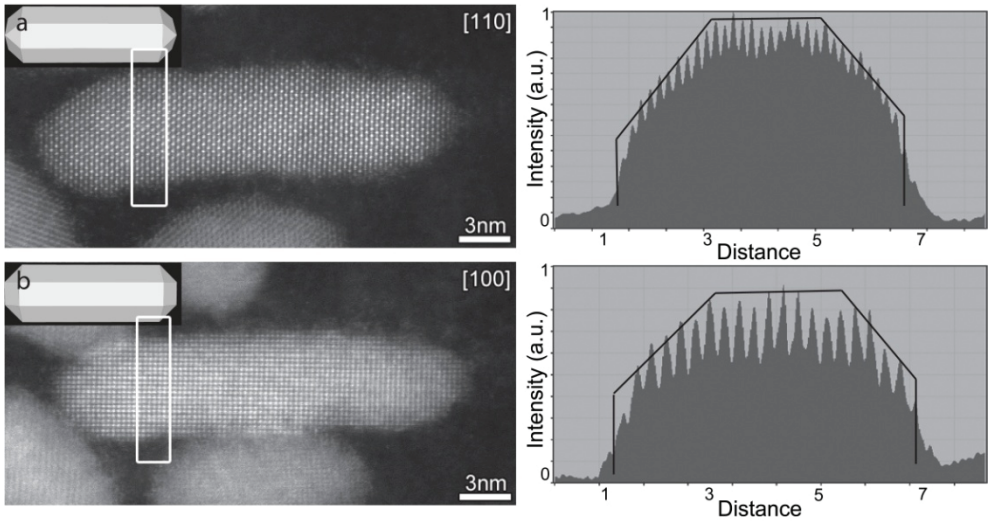

Figure 5.3: High resolution HAADF-STEM image of PbSe nanorod oriented along the [110] zone axis a, and along the [100] zone axis b. Both the outer shapes of the projection and the intensity profiles corresponds to our model of a nanorod with truncated {100} and {110} facets along the long facets and {100} termination along the short facets.

It has been reported that solvent evaporation in a similar reactor system induces the self-assembly of colloidal nanocrystals into well-ordered and self-supported nanocrystal membranes held together by van der Waals attractions between the capping molecules[16]. In line with this, we observed hexagonally ordered monolayers of PbSe nanocrystals if we used PbSe nanocrystals protected with an inactive CdSe shell (Figure 5.4a). However, when we used the oleic acid capped PbSe nanocrystals, the nanocrystal ordering in the structures formed by solvent evaporation changed dramatically and is accompanied by oriented attachment of the crystals, instead of self-assembly driven by van der Waals attractions.

We first review the effect of the three reaction parameters on the structures obtained by nanocrystal attachment, see Figure 5.5, panels a, b and c. More complete data sets are presented in the appendix in Figure A5.1. Figure 5.5a, shows the effect of the initial nanocrystal concentration for nanocrystals of 5.4 nm in size, when the reaction is carried out at a temperature of 50 °C. Notice that, at low particle concentrations, attachment of the nanocrystals lead to disordered aggregates; an examples is given in Figure 5.4b. However, above a given nanoparticle concentration, the attachment leads to ordered structures with a well-defined geometry being determined by the nanoparticle concentration. This means that under given conditions, only one type of facet is active in the crystal bonding, and that there is a directional control in the nanocrystal attachment. The TEM pictures in Figure 5.5a show that the crystal attachment leads to nanocrystal wires, a 2-D honey-comb lattice, and finally a 2-D square lattice by simply increasing the particle concentration. Figure A5.1 presents the structures formed by 9.9 nm PbSe cubes treated at 100 °C: rod-like systems are observed at ~$2*10^{-7}$ mol/L, perfect planar sheets with square nanocrystal ordering at ~$11*10^{-7}$ mol/L, and 3-D sheets at particle concentrations larger then ~$21*10^{-7}$ mol/L. We remark that the previously reported formation of linear structures or 2-D sheets by attachment of Pb-chalcogenide nanocrystals demands different crystals (PbSe and PbS) and reaction conditions. Here, however, we show that in one colloidal system, the particle concentration can control the dimensionality and the nanoscale geometry (2-D honeycomb and 2-D square) of the formed structures.

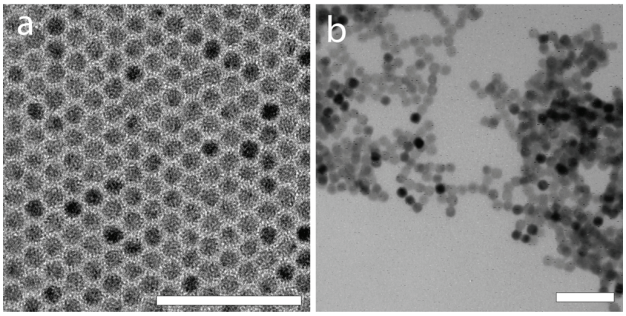

Figure 5.4: Structures formed of 'protected' PbSe|CdSe core|Shell particles (a). Disordered aggregates observed at low concentration (b). The scale bars represent 50 nm.

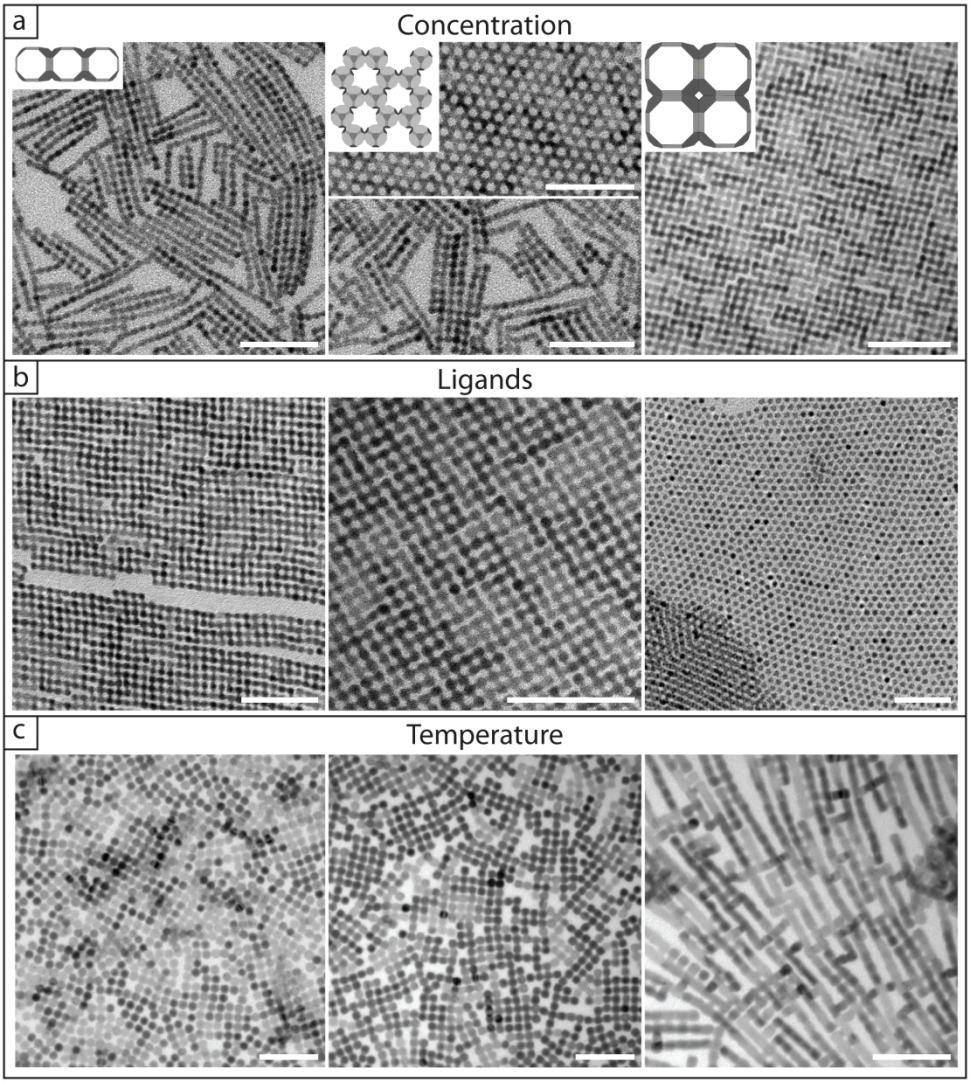

Figure 5.5: Effects of the reaction parameters on the structures formed by oriented attachment of PbSe nanocrystals. The structural characterization was performed by TEM. a, Effect of the initial particle concentration in the NC suspension. The colloidal building blocks were truncated PbSe cubes with a size of 5.4 nm capped with oleic acid, the reaction temperature was 50 °C. The initial particle concentrations are: left: 7.0 10^{-7}, centre 11.3 10^{-7}, right 28 10^{-7} mol/L. The insets show cartoons of the linear structures, honeycomb superlattices and ultra-thin sheets with square nanostructuring. b, Effect of oleic acid ligand addition to the ethylene glycol liquid substrate. The building blocks were truncated PbSe cubes with a size of 5.4 nm capped with oleic acid, the reaction temperature was 50 °C and the initial particle concentration was 28 10^{-7} mol/L. The concentrations of added oleic acid in the ethylene glycol are: left; no additional ligands added, centre: 4.10^{-5} mol/L, right:4.10^{-4} mol/L. Fig 1c: Effect of reaction temperature. The building blocks were truncated PbSe cubes with a size of 7.5 nm capped with oleic acid, the initial particle concentration in the suspension was 14 10^{-7} mol/L. The reaction temperature was left: 45, centre: 100 and right: 140 C. All scale bars represent 50 nm.

The findings above suggest that the detachment of the capping molecules from specific facets and dissolution of these in the ethylene glycol drives crystal attachment. To further investigate this, we monitored the effect of addition of capping molecules to the ethylene glycol (Figure 5.5b and Figure 5.6). From the results it becomes clear that the addition of sufficient capping molecules to the ethylene glycol stabilizes all facets of the particles, prevents oriented attachment, and leads to the formation of self-assembled hexagonal (mono) layers of stable particles for any starting configuration of the nanocrystals (Figure 5.6). This shows that the equilibria involving the capping molecules in the suspension (free and attached to the NC facets) and the glycol phase are of primary importance in the controlled reactions that we observe. In this view, the disordered NC aggregation that we observe at low particle concentration can be understood as being the effect of a very low concentration of free ligands in the suspension and the glycol liquid substrate resulting in the stripping of the capping molecules from different NC facets and random crystal attachment. The effect of the temperature at a given particle concentration can be followed via the horizontal panels of Figure 5.5C; more examples are presented in the appendix in Figure A5.1. At a sufficiently high particle concentration, square 2-D sheets form at lower temperature (45 °C), whereas at higher temperatures (branched) rods are favored.

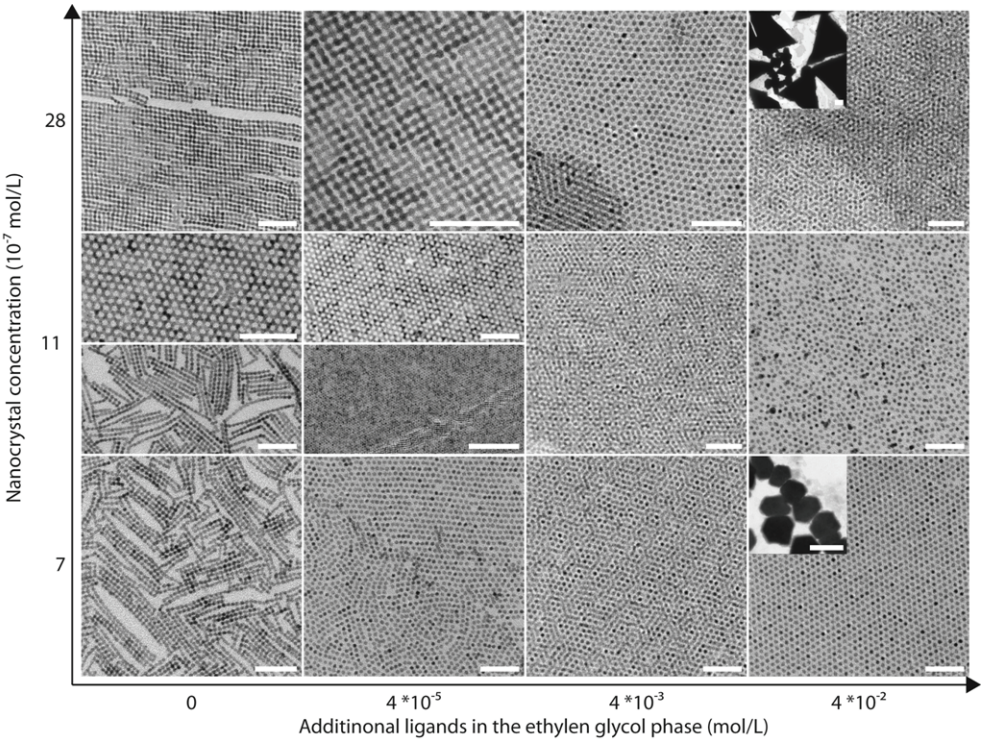

Figure 5.6: Effect of additional oleic acid capping ligands in the glycol phase as function of the nanocrystal concentration for 5.4 nm PbSe nanocrystals The scale bars represent 50 nm except for the insets were they represent 1 μm.

The results so far showed that the reaction parameters can control the geometry of the formed structures. With the smaller 5.4 nm PbSe particles, there are even two different planar geometries: the honeycomb superlattice and the square sheets. The striking uniformity of the resulting structures show that only one type of facet is involved in the reaction under given conditions. The atomic details of crystal attachment were further elucidated by a detailed HAADF-STEM[17] study, see Figure 5.7, Figure 5.10 and Figure 5.11. Figure 5.7 a and b show typical HAADF-STEM images of the linear attachment of two nanocrystals. The atomic columns of Pb and Se can be observed separately along the [110] viewing axis in Figure 5.7a, while along the [100] viewing axis (Figure 5.7b), the atomic columns contain both Pb and Se (see atomic overlays). Panel c shows a 3-D illustrative model of how two cubes attached in a linear fashion. For the PbSe wires and square sheets it was observed that crystal attachment occurred mostly via <100>/<100> connections, while <100>/<110> and <110>/<110> connections, breaking the overall square symmetry, are infrequent. Anomalous attachments and defects in the structures can be characterized by HAADF-STEM, defects will be discussed below. It is clear that in the example presented in Figure 5.7, the attachment occurs with full atomic matching of the {100} planes. The connection plane contains columns with considerably less atoms, which is directly related to the shape of the truncated nanocubes involved. The XRD patterns of 2-D sheets formed by oriented attachment indicate that the nanocrystals are uniformly oriented with their [100] axis perpendicular to the substrate, in agreement with attachment involving exclusively the four vertical {100} facets. Further evidence for nearly exclusive attachment via {100} planes follows from the use of PbSe nanorods and stars, see Figure 5.8 and Figure 5.9. HAADF-STEM shows that the nanorods that we used have a smooth {100} facet termination at both tips, while the long sides are {100} facets that are considerably roughened (Figure 5.3). In this case, attachment results in the formation of wires only, formed by linear connection of the rods without 2-D branching. Possibly, the roughness of the {100} facets at the long sides prevents the formation of 2-D structures. The PbSe stars can be seen as cubes with a pyramid grown on each of the {100} facets. These crystals do not display {100} facets, except for presumably small facets at the tip ends. Strikingly, solvent evaporation at increased temperature leads to the formation of attached stars displaying a linear or planar square symmetry; the connections occur only via the sharp tips. This demonstrates the astounding dominance of the {100} facets in the attachment process. In contrast, however, the remarkable honeycomb superlattices cannot be understood by attachment of the {100} facets. The atomic details of the honeycomb superstructures investigated by HAADF-STEM are presented in Figure 5.7d-f. It is observed that the nanocrystals are all oriented with the [111] direction perpendicular to the 2-D sheet plane. Using models for truncated nanocubes, it became clear that this specific orientation is the only way to form a honeycomb lattice and that the {110} facets are exclusively involved in atomic bonding. Three of the twelve {110} facets of each nanocrystal are used, as shown in Figure 5.7e,f. Theoretical work shows that the {100} facets have a somewhat lower surface energy than the {110} facets, and much lower in

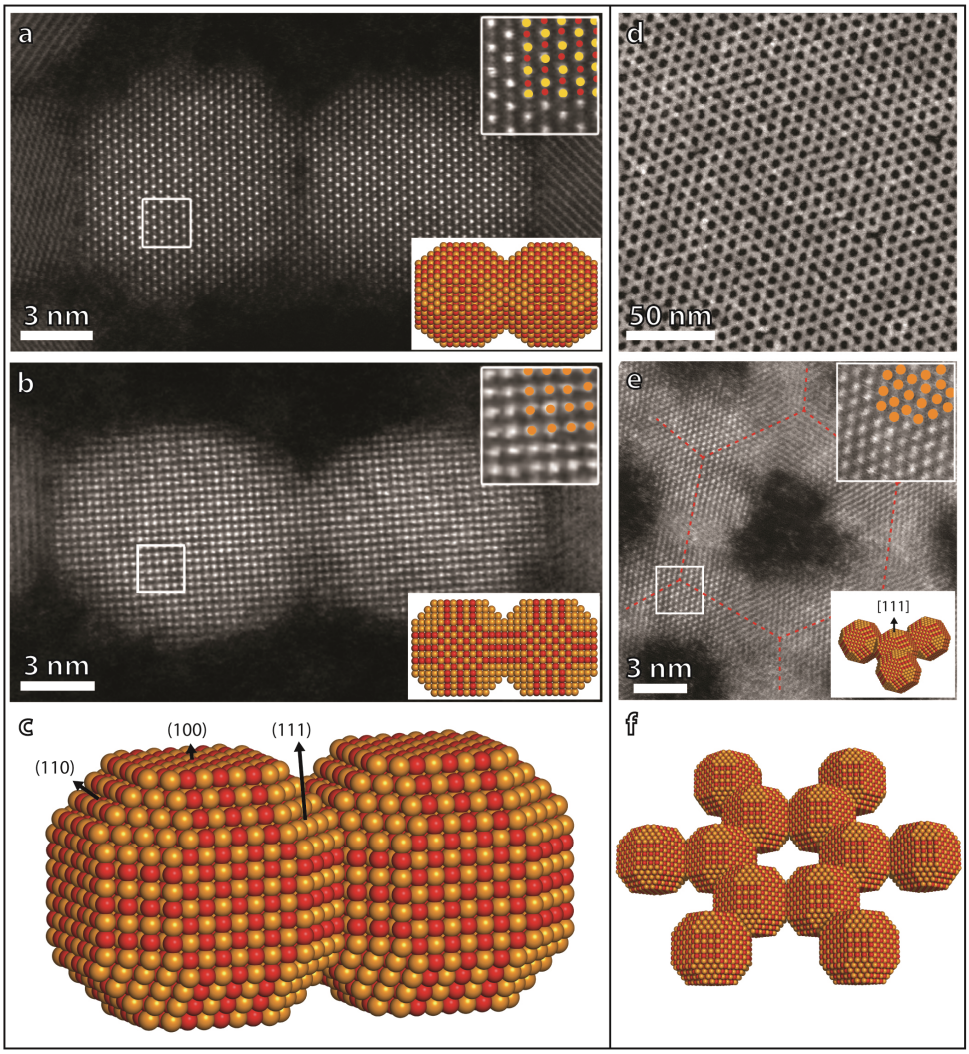

Figure 5.7: Atomic details of the oriented attachment of PbSe nanocrystals as revealed by HAADF-STEM. Left panel: oriented attachment via {100} facets leading to wires or ultra-thin sheets. a, HAADF-STEM image of two fusing NCs along the [110] projection. b, HAADF-STEM image of two fusing NCs along the [100] projection. In the inset of a and b a detailed zoom in is given with atomic overlay of the atomic columns (yellow Pb, red Se, orange Pb and Se). The PbSe NCs are attached along the {100} facets. c, model of the two fused NCs. Right panel: Oriented attachment via the {110} facets resulting in a honeycomb superlattice. d, overview of the honey-comb lattice, e, detailed HAADF-STEM picture showing the [111] projection of the original building blocks, f: 3-dimensional model with atomic resolution showing how the building blocks are attached via the {110} facets, while the [111] projection is vertical.

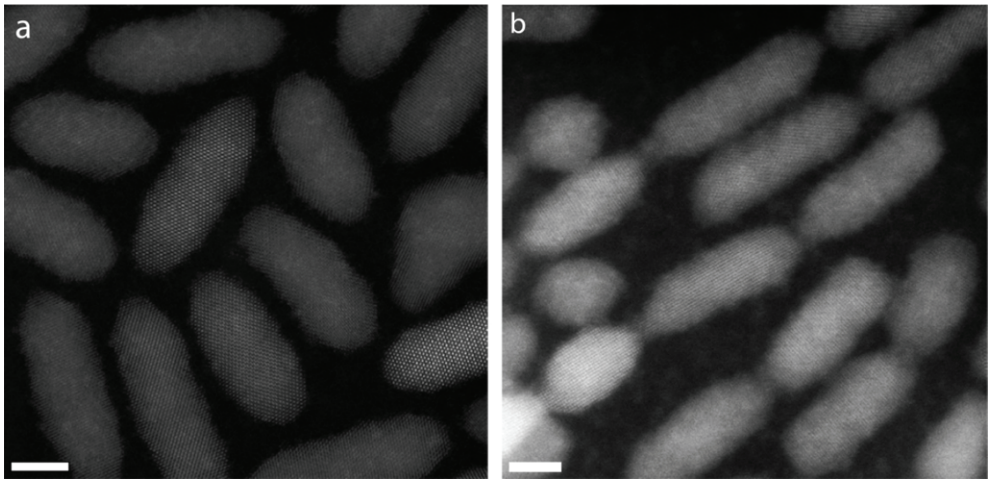

Figure 5.8: Linear oriented attachment of PbSe nanorods. a, drop casted nanorods, and b, a picture after solvent evaporation at a temperature of 20 °C, leading to attachment via the {100} tips.

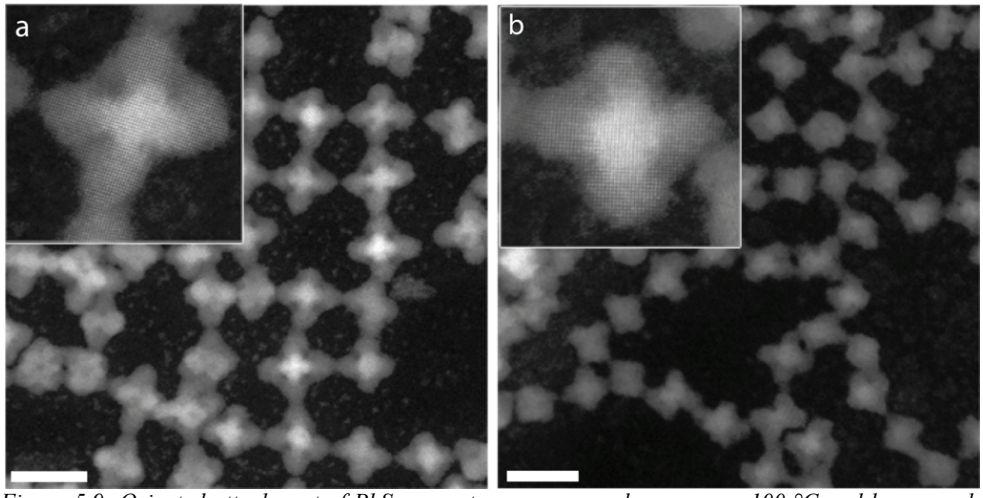

Figure 5.9: Oriented attachment of PbSe nanostars. a, a sample grown on 100 °C and b, a sample grown on 150 °C.

energy than the {111} facets.[18] This suggest that the dominance of the {100} facets in attachment is due to the fact that at this facet the adsorption equilibrium is shifted the most in the direction of free capping molecules in the suspension and the underlying glycol liquid. The higher energy {110} and the Pb-terminated {111} facets remain better protected by the oleic acid capping molecules. That such adsorption/desorption equilibria are a key for further understanding is shown by the fact that addition of a small amount of capping molecules in the glycol liquid substrate prevents oriented attachment. However, we should remark that the sudden transition from the linear attachment via {100} facets to the honeycomb lattice via {110} facets to the square sheets again via {100} facets cannot be explained intuitively.

The irreversible strong bonding of the nanocrystals by oriented attachment leads inherently to imperfect attachment events. Imperfect attachment induces crystal defects during the growth.[19] In the case reported here, oriented attachment does not always occur by connection of two perfectly aligned {100} facets. Figure 5.10a shows two attached nanocubes, their opposed {100} planes were, however, not completely parallel resulting in an edge dislocation. Figure 5.10b shows another defective way of attachment: the nanocubes in the linear structure have parallel {100} bonding facets; they are, however, all differently rotated in the plane perpendicular to the bond axis.

When the structures formed by oriented attachment are thermally treated under nitrogen, remarkable atomic reconfigurations are observed in which the effects of misorientations are annealed, and the original shape of the building blocks is gradually washed out. A part of a nearly perfectly smooth PbSe sheet obtained by oriented attachment and thermal annealing is presented in Figure 5.10c; only a small trace of the early connection of two nanocrystals is still visible. The results of oriented attachment of small PbSe nanocubes at 50 °C, and further annealing are presented in Figure 5.11. Panel A shows a planar sheet formed by oriented attachment of PbSe nanocubes 5.4 nm in diameter; the structure that constitutes an atomic PbSe rocksalt single crystal still shows the signature of the original building blocks. If oriented attachment is followed by a thermal treatment at 80 °C, a further atomic smoothening is observed leading to a two-dimensional network in which the original nanocubes cannot anymore be recognized.

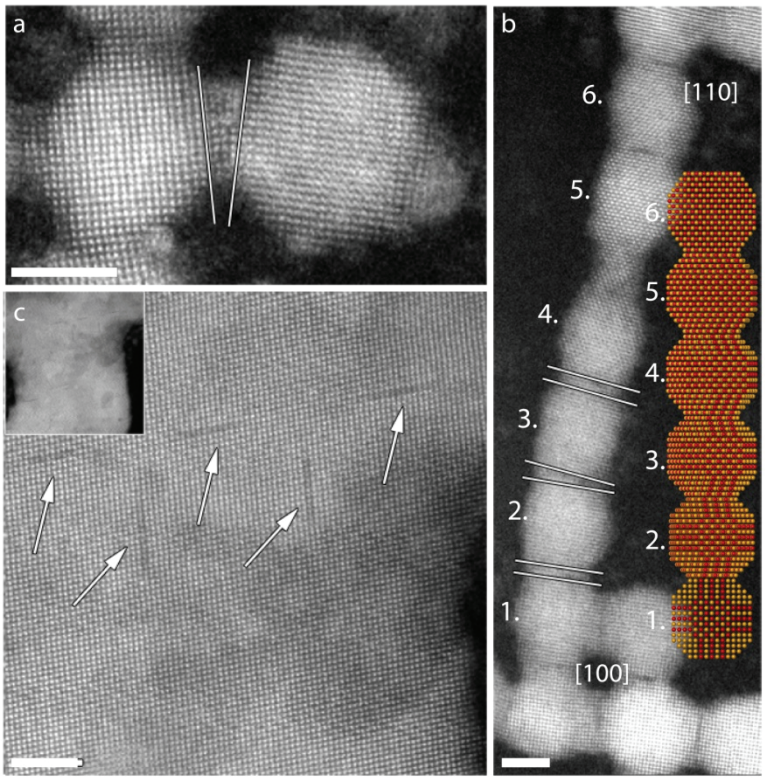

Figure 5.10: Imperfect oriented attachment of PbSe nanocrystals. a) Two attached NC with their {100} planes being not completely parallel, resulting in an edge dislocation. b) The NCs are rotated over 45° over 6 particles in respect to the bonding axis, resulting in a screw dislocation. c) Nearly defect free single-crystalline sheet with a nearly homogenous thickness and lateral dimensions in the µm range. The arrow indicates missing rows where the original particles were situated. The particles used in a and b are 7.5 nm PbSe NCs while in c 9.9 nm PbSe NCs were used. The scale bars represent 4 nm.

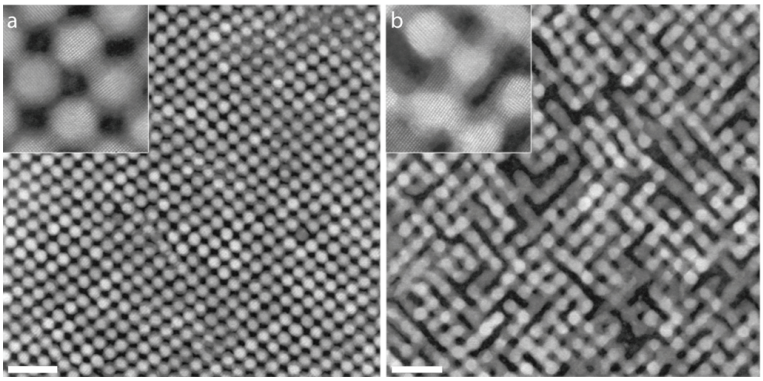

Figure 5.11: Oriented attachment and further atomic reconstructions in a square PbSe superlattice. Both samples a and b were grown under identical conditions at 50 °C, resulting in a single crystalline square lattice such as depicted in a. b Presents the atomic reconfigurations taking place by further annealing at 80 °C. The scale bars represent 20 nm.

The exclusive use of one type of crystal facets, i.e. {100} or {110}, together with the control over the dimensions and the nanoscale geometry by the particle concentration and temperature is remarkable and non-trivial. Here, we attempt to present the main factors that will be required for further understanding. The formation of extended low-dimensional PbSe crystals, i.e. wires and square sheets from cubic building blocks that have 6 equivalent {100} facets must be the result of symmetry breaking. This indicates that oriented attachment in our reactor system takes place at an interface. In recent theoretical work performed by J. de Graaf, the adsorption of cubic and truncated cubic nanocrystals at the air-toluene interface was investigated; more details are given in appendix 5.3. It was observed that for limited levels of truncation (e.g. for the 9.9 nm PbSe nanocubes) there are two preferred geometries associated to the adsorption, i.e., configurations which minimize the free energy. One of the two corresponds to the PbSe nanocube adsorbed at the interface via a {100} facet (Figure 5.12a,b), while the other one is absorbed via the {110} facet, which implies that respectively the four adjacent or two opposite {100} facets are standing perpendicular to the interface, leaving these free to be involved in oriented attachment in a square or rod like fashion in the direction parallel to the plane of the interface, in the way sketched in Figure 5.7a-c. Alternatively, Cho et al. argued that linear attachment is mediated by a residual electric dipole resulting from the uneven distribution of the {111} Pb and Se facets; once two nanocrystal are attached, the electrical dipole is enhanced leading to further elongation of the rod by new linear attachment events.[4] It should however be remarked that, according to Molecular Dynamics simulations, the {111} Se planes are considerably reconstructed leading to a charge reduction.[20] Another point that needs further attention is the formation of the honeycomb superstructures in which each nanocrystal uses three {110} facets. Our calculations show that attachment of the PbSe nanocubes with a [111] direction perpendicular to the interface is one of the three possible adsorption configurations (see Figure 5.12c-d) that minimize the free energy in case the nanocrystals are considerably truncated (for the 5.4 nm nanocubes). In this adsorption configuration, the truncated {110} planes have an angle of 0.6π with the interface and are available for oriented attachment in the way sketched in Figure 5.7e-f, resulting in the honeycomb superstructure. It is however, not easy to understand why the adsorption geometry changes from perpendicular [111] to [100] by simply increasing the particle concentration.

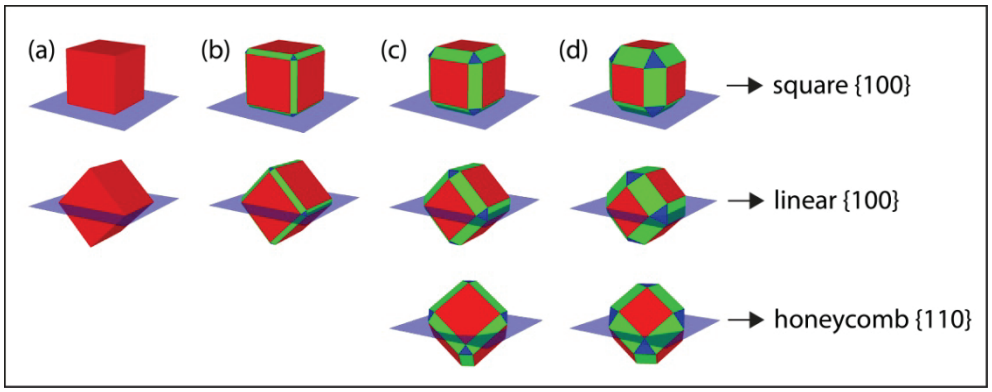

Figure 5.12: The prototypical equilibrium configurations for truncated PbSe nanocubes adsorbed to a flat toluene-air interface as determined by our theoretical approach: see appendix 5.3 for more information. The level of truncation increases from left to right and the various crystal facets are indicated using three colours: (red) {100} facets, (green) {110} facets, and (blue) {111} facets. The interface is given by a translucent blue square. (a) For a cube we find exactly two possible adsorption equilibria: one with the normal to one of the {100} facets pointing towards the z-axis and one where the normal to one of the {110} 'facets' is pointing upward. (b) For slightly greater levels of truncation we again find these two configurations. (c-d) For even greater levels of truncation a third configuration appears, for which the normal to one of the {111} facets is pointing upward.

The two-step bottom-up method that we present here, i.e. synthesis of well-defined nanocrystals from atomic precursors, followed by oriented attachment under mild conditions in a thin film of suspension casted on an immiscible liquid holds promise for the fabrication of one and two dimensional semiconductors with applications in nanophysics and opto-electronic devices.[16, 21, 22] The work presented above shows that with PbSe nanocube building blocks, simple reaction parameters such as the temperature and particle concentration can be used to prepare 1-D rods and 2-D nanostructured sheets at will. Moreover, the reaction can be moderated by controlled addition of oleic acid capping molecules to the ethylene glycol substrate. The use of a liquid ethylene glycol substrate has another important asset: the products of oriented attachment are suspended on a liquid substrate and can, in this way, be transferred to a solid substrate or an electrical device or be used in soft printing techniques. Some examples of two-dimensional ultra-thin sheets with a honeycomb and square nanostructuring are presented in Figure 5.13. The electro-diffractograms presented in the insets of Figure 5.13a,b show that overall the structures are single crystalline (rocksalt PbSe) with an added superstructure periodicity in the nanometer range. This is in line with HAADF-STEM results displayed in Figure 5.7 that show smooth atomic connections between the nanocrystals. There is recently much attention to the effects of a super-periodicity on the electronic properties of semiconductors and confined two-dimensional electron gases.[23-26] It has, for instance, been shown that when a two-dimensional fermion gas is subject to a honey-comb periodic potential, this results in the emergence of an electronic sub-band with a linear energy-wave vector relationship, in a similar way as for graphene. A honeycomb nanometer periodicity opens thus the possibility

to engineer Dirac Fermions in various semiconductor compounds. Tight-binding calculations are under way to reveal the electronic sub-bands of the two-dimensional PbSe sheets with a square and honeycomb structure a shown in Figure 5.13.

While we demonstrate geometric control with nanocrystals of the lead-chalcogenide family, we should remark that the formed one- and two-dimensional semiconductors can be further transformed to other semiconductor compounds by means of ion exchange while the overall geometry and crystallinity is preserved. For instance, in Figure 5.13c we show that the ultra-thin PbSe rocksalt sheets can be converted into CdSe zinc blende sheets while preserving the square nanostructuring. In the appendix, Figure A5.2 we show the conversion of the CdSe sheets to $Cu_{2-x}Se$ sheets. The latter compound opens the gate to use cation exchange in order to obtain low-dimensional superlattices of various semiconductor compounds.[27-30] Hence, we showed that the low-dimensional PbSe structures prepared by oriented attachment can be transformed to many other compounds while the overall superlattice geometry is preserved. Although many 2-D semiconductors can also be prepared by precious gas-phase methods, the latter methods often do not allow obtaining a superlattice structure with periodicity in the nanometer region, such as the ones we present in Figure 5.13.

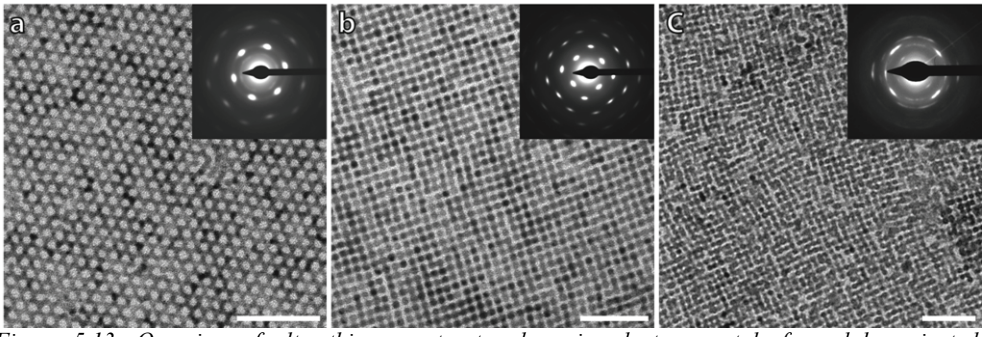

Figure 5.13: Overview of ultra-thin nanostructured semiconductor crystals formed by oriented attachment of 5.4 nm PbSe nanocrystals. a, Ultrathin PbSe rocksalt semiconductor sheet with a honeycomb nanostructuring. The periodicity of the honeycomb structure is 6.5 nm. Inset: electro-diffractogram showing the PbSe rocksalt lattice in the [111] projection. b,: Ultrathin PbSe rocksalt semiconductor sheet with a square nanostructuring. The periodicity of superlattice structure is 6.6 nm. Inset: electro-diffractogram showing the PbSe rocksalt lattice in the [100] projection. c, Ultrathin CdSe semiconductor with a compressed zincblende atomic structure and slightly distorted square nanostructuring. Inset: electro-diffractogram showing the CdSe zincblende lattice in the [100] projection. All scale bars represent 50 nm.

5.4 Conclusion

In summary, we have presented results that show that the process of oriented attachment of PbSe nanocrystals can be controlled by variation of simple reaction parameters, resulting in single-crystalline PbSe nanostructures with dimensions between one and three. The ultra-thin 2-D sheets are single crystalline and show a super periodicity with planar square or honeycomb geometry. The structures can be picked up on a substrate of choice and even be transformed to other semiconductor compounds preserving the overall geometry.

References

1. Banfield, J. F.; Welch, S. A.; Zhang, H. Z.; Ebert, T. T.; Penn, R. L. *Science* **2000**, 289, (5480), 751.
2. Niederberger, M.; Colfen, H. *Physical Chemistry Chemical Physics* **2006**, 8, (28), 3271.
3. Zheng, H.; Smith, R. K.; Jun, Y.-w.; Kisielowski, C.; Dahmen, U.; Alivisatos, A. P. *Science* **2009**, 324, (5932), 1309.
4. Cho, K. S.; Talapin, D. V.; Gaschler, W.; Murray, C. B. *Journal of the American Chemical Society* **2005**, 127, (19), 7140.
5. Yu, Z.; Liu, B.; Ye, B.; Kong, W.; Weng, J.; Wang, Z.; Wang, H. *Rare Metal Materials and Engineering* **2010**, 39, 133.
6. Pacholski, C.; Kornowski, A.; Weller, H. *Angewandte Chemie-International Edition* **2002**, 41, (7), 1188.
7. Schliehe, C.; Juarez, B. H.; Pelletier, M.; Jander, S.; Greshnykh, D.; Nagel, M.; Meyer, A.; Foerster, S.; Kornowski, A.; Klinke, C.; Weller, H. *Science* **2010**, 329, (5991), 550.
8. Xu, F.; Ma, X.; Gerlein, L. F.; Cloutier, S. G. *Nanotechnology* **2011**, 22, (26).
9. Koh, W. K.; Bartnik, A. C.; Wise, F. W.; Murray, C. B. *Journal of the American Chemical Society* **2010**, 132, (11), 3909.
10. Manna, L.; Milliron, D. J.; Meisel, A.; Scher, E. C.; Alivisatos, A. P. *Nature Materials* **2003**, 2, (6), 382.
11. Yin, Y.; Alivisatos, A. P. *Nature* **2005**, 437, (7059), 664.
12. Zhang, J.; Huang, F.; Lin, Z. *Nanoscale* **2010**, 2, (1), 18.
13. Evers, W. H.; De Nijs, B.; Filion, L.; Castillo, S.; Dijkstra, M.; Vanmaekelbergh, D. *Nano Letters* **2010**, 10, (10), 4235.
14. Houtepen, A. J.; Koole, R.; Vanmaekelbergh, D.; Meeldijk, J.; Hickey, S. G. *Journal of the American Chemical Society* **2006**, 128, (21), 6792.
15. Casavola, M.; van Huis, M. A.; Bals, S.; Lambert, K.; Hens, Z.; Vanmaekelbergh, D. *Chemistry of Materials* **2011**, 24, (2), 294.
16. Dong, A. G.; Chen, J.; Vora, P. M.; Kikkawa, J. M.; Murray, C. B. *Nature* **2010**, 466, (7305), 474.
17. Bals, S.; Casavola, M.; van Huis, M. A.; Van Aert, S.; Batenburg, K. J.; Van Tendeloo, G.; Vanmaekelbergh, D. *Nano Letters* **2011**, 11, (8), 3420.
18. Fang, C. M.; van Huis, M. A.; Vanmaekelbergh, D.; Zandbergen, H. W. *ACS Nano* **2010**, 4, (1), 211.
19. Penn, R. L.; Banfield, J. F. *Science* **1998**, 281, (5379), 969.
20. Schapotschnikow, P.; van Huis, M. A.; Zandbergen, H. W.; Vanmaekelbergh, D.; Vlugt, T. J. H. *Nano Letters* **2010**, 10, (10), 3966.
21. Talapin, D. V.; Black, C. T.; Kagan, C. R.; Shevchenko, E. V.; Afzali, A.; Murray, C. B. *Journal of Physical Chemistry C* **2007**, 111, (35), 13244.
22. Talapin, D. V.; Murray, C. B. *Science* **2005**, 310, (5745), 86.

23. Akhmerov, A. R.; Beenakker, C. W. J. *Physical Review B* **2008**, 77, (8), 085423.
24. Park, C.-H.; Yang, L.; Son, Y.-W.; Cohen, M. L.; Louie, S. G. *Physical Review Letters* **2008**, 101, (12).
25. Park, C.-H.; Louie, S. G. *Nano Letters* **2009**, 9, (5), 1793.
26. Gomes, K. K.; Mar, W.; Ko, W.; Guinea, F.; Manoharan, H. C. *Nature* **2012**, 483, (7389), 306.
27. Li, H.; Brescia, R.; Krahne, R.; Bertoni, G.; Alcocer, M. J. P.; D'Andrea, C.; Scotognella, F.; Tassone, F.; Zanella, M.; De Giorgi, M.; Manna, L. *ACS Nano* **2012**, 6, (2), 1637.
28. Jain, P. K.; Amirav, L.; Aloni, S.; Alivisatos, A. P. *Journal of the American Chemical Society* **2010**, 132, (29), 9997.
29. Li, H.; Zanella, M.; Genovese, A.; Povia, M.; Falqui, A.; Giannini, C.; Manna, L. *Nano Letters* **2011**, 11, (11), 4964.
30. Jain, P. K.; Beberwyck, B. J.; Fong, L.-K.; Polking, M. J.; Alivisatos, A. P. *Angewandte Chemie International Edition* **2012**, 51, (10), 2387.
31. Pieranski, P. *Physical Review Letters* **1980**, 45, (7), 569.
32. Young, T. *Philosophical Transactions of the Royal Society of London* **1805**, 95, 65.
33. de Graaf, J.; Dijkstra, M.; van Roij, R. *Physical Review E* **2009**, 80, (5), 051405.
34. de Graaf, J.; Dijkstra, M.; van Roij, R. *The Journal of Chemical Physics* **2010**, 132, (16), 164902.
35. Graaf, J. d. Anisotropic nanocolloids: Self-assembly, interfacial adsorption, and electrostatic screening, PhD thesis. Utrecht Univeristy, Utrecht, **2012**.
36. Friedrich, H.; Gommes, C. J.; Overgaag, K.; Meeldijk, J. D.; Evers, W. H.; de Nijs, B.; Boneschanscher, M. P.; de Jongh, P. E.; Verkleij, A. J.; de Jong, K. P.; van Blaaderen, A.; Vanmaekelbergh, D. *Nano Letters* **2009**, 9, 2719.
37. Smith, D. K.; Goodfellow, B.; Smilgies, D.-M.; Korgel, B. A. *Journal of the American Chemical Society* **2009**, 131, (9), 3281.
38. Adamson, A. W.; Gast, A. P., *Physical chemistry of surfaces*. 6th ed.; Wiley-Interscience: New-York, **1997**.

Appendix 5.1 Overview of the obtained structures

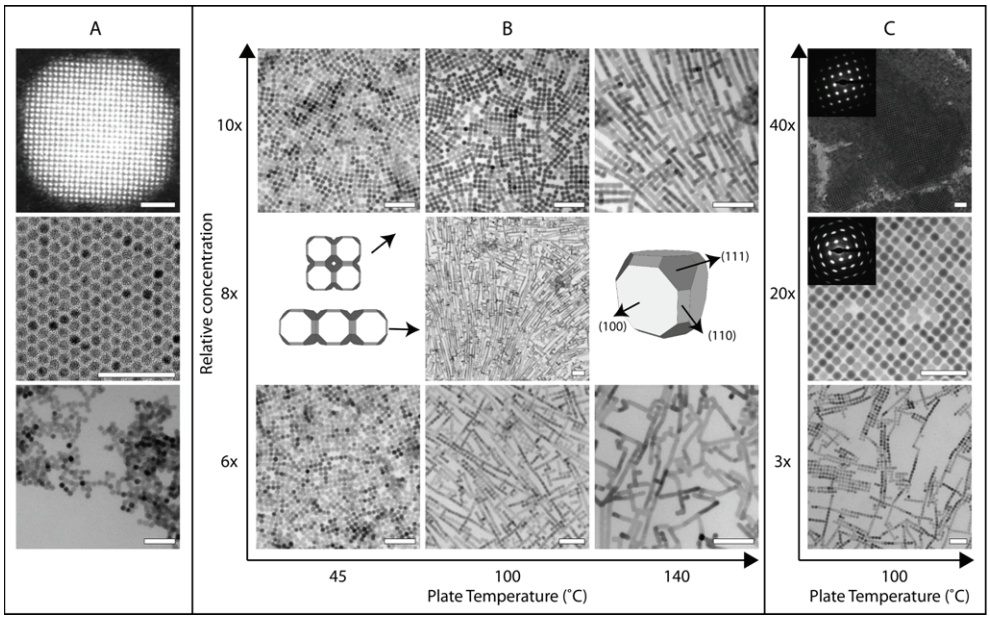

Figure A5.1: Overview of the obtained structures. Panel A from top to bottom; Top; 9.9 NC showing the truncation along the {110} planes. Middle; Hexagonal ordering of 7.0 nm PbSe|CdSe core shell structures on ethylene glycol at 100 °C. The CdSe acts as protection, hence no oriented attachment is observed. Bottom; Aggregates of 7.5 nm NC observed when low concentrations were used (<2x C_{Ref} = 140 nM for the 7.5 nm particles). Panel B: PbSe NCs with a diameter of 7.5 nm, Panel C: PbSe NCs with a diameter of 9.9 nm. From bottom to top increasing concentration with respect to the lowest concentration used in the sequences. From left to right, for panel B, increasing temperature of the reaction. At low concentrations predominately linear aggregation with two bonding sites is observed. With increasing concentration square ordering occurs with oriented attachment that involves 4 bonding sites. By increasing the temperature of the reaction the reversed trend can be observed, at low temperature square arrangement occurs while at high temperature linear attachment is predominant. From the electron difractogram in the inset in the 2-D and 3-D structures in panel C it can be concluded that the particles are not only oriented on the NC scale but also on the atomic scale. The scale bar in the top image of panel A represents 2 nm, all other scale bars represent 50 nm.

Appendix 5.2 Conversion of PbSe sheets to CdSe and $Cu_{2-x}Se$ sheets by ion exchange

The conversion of a PbSe sheet into a CdSe sheet was realized by placing the PbSe sheet on a substrate (TEM-grid or silicon (100) wafer), which was then brought in contact with a 0.1 M Cd-oleate solution in 1-octadecene and heated up to 130 °C for 2 hours. The results presented in Figure A5.2a provide evidence that the sheets preserve their sqaure particle symmetry, while from the electron diffraction patterns and SEM-EDX results it follows that the atomic lattice is changed completely from rocksalt to zinc blende. SEM-EDX spectra show that the sheets are transformed from a PbSe to a CdSe composition.
The conversion of PbSe sheets into $Cu_{2-x}Se$ was obtained by first converting the PbSe sheet to a CdSe sheet as described above and a similar Cd to Cu cation exchange as performed by Jain *et al.*[28] After the CdSe exchange the TEM grids were placed in a 2 mL 0.03M solution of tetrakis(acetonitrile)copper(I) hexafluorophosphate in methanol for 1 min. After which they were rinsed with toluene and methanol subsequently. The results in Figure A5.2b provide evidence that the sheets preserved their square particle symmetry, while the TEM-EDX results it follows that the atomic lattice is changed to $Cu_{2-x}Se$.

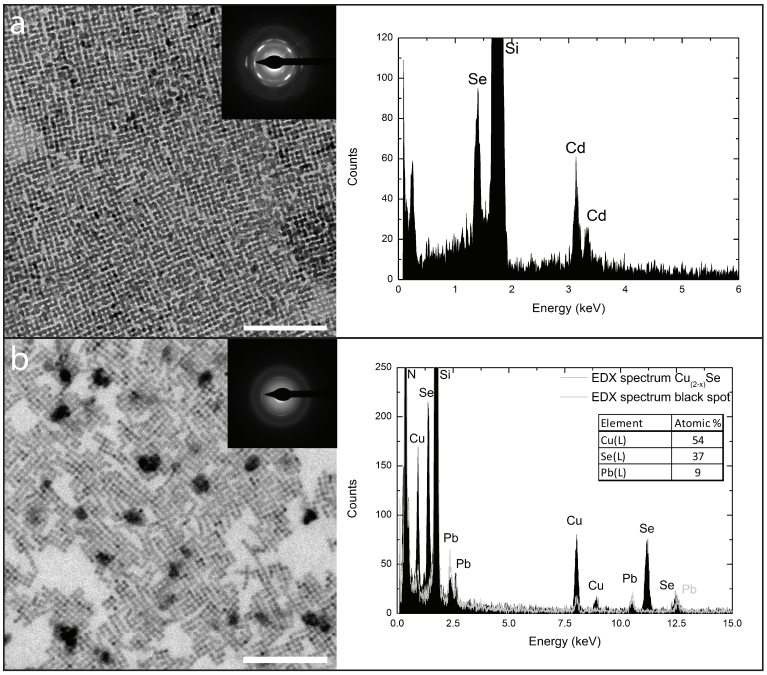

Figure A5.2: TEM image, electron diffractograms and TEM or SEM -EDX spectrum of the obtained structures after cation exchange. a, a CdSe sheet resulting from a Cd-for-Pb cation exchange reaction starting from a PbSe sheet and the corresponding SEM-EDX measurement. b, a $Cu_{2-x}Se$ sheet resulting from a Cu-for-Cd cation exchange reaction starting from a CdSe sheet. The EDX spectrum of the NC (black) shows both Cu, Se and some residual Pb ions while the black spots in the TEM image are composed out of Pb and Cu (grey). The scale bars represent 100 nm.

Appendix 5.3 Theoretical study on the interfacial adsorption of a truncated cube

The theoretical study was performed by Joost de Graaf working in the group of Marjolein Dijkstra and René van Roij, Soft Condensed Matter, Utrecht University and put in this thesis with permission prior to publication in the supporting information file of a joint paper; "low dimensional semiconductor superlattices formed by geometric control over nanocrystal attachment".

In this section we consider the adsorption of a single truncated (nano) cube at a flat toluene-air interface using a theoretical model based on surface-tension arguments. We apply a model similar to that of P. Pieranski, who analyzed the strength of adsorption of spherical colloids at liquid-gas and liquid-liquid interfaces.[31]

To describe the experimental system, we consider a truncated cube which, in its initial configuration, is given by the set of vertices

$$\{v(q)\} = \frac{\mathrm{P_D}\left((\pm 1, \pm(1-\mathrm{q}), \pm(1-\mathrm{q}))^{\mathrm{T}}\right)}{\sqrt{4(\sqrt{3}q^2+6\sqrt{2}q(1-q)+6(1-q)^2)}} \qquad (1)$$

where q ∈ [0, 1] is the truncation parameter, 'T ' indicates transposition, P_D is a permutation operation that generates all permutations of each element in the set of 8 vertices spanned by the ±-operations (which are allowed to act independently of each other). By letting P_D act we obtain 48 vertices. Subsequent deletion of all duplicates reduces this set to the desired total of 24 vertices for a truncated cube with 6 {100}, 12 {110}, and 8 {111} facets. The expression in the denominator ensures that the truncated cube is normalized to unit surface area. By changing the value of q the truncated cube deforms smoothly from a cube (q = 0) to an octahedron (q = 1) via a cuboctahedron ($q = \sqrt{2}/(\sqrt{2}+1) \approx 0.586$), also see Figure A5.3, which shows our model for various levels of truncation. We restrict ourselves to q ∈ [0, 0.6] in the following.

In its initial configuration the truncated cube has the normals of its {100} facets aligned with the axes of a standard Cartesian coordinate frame and its centre coincides with the origin. When this truncated cube is brought into contact with a flat undeformed liquid-gas or liquid-liquid interface, the system can be described by four parameters: (i) the size of the particle, which is given by the multiplicative factor s that acts on the vertices in Eq. (1); (ii) the height z of the particle with respect to the interface (as measured along the z-axis), which we locate at z =0 (xy-plane); (iii) rotation by the azimuthal angle ψ (around the z-axis); and (iv) rotation by the polar angle φ (around the y-axis). The angles are indicated in

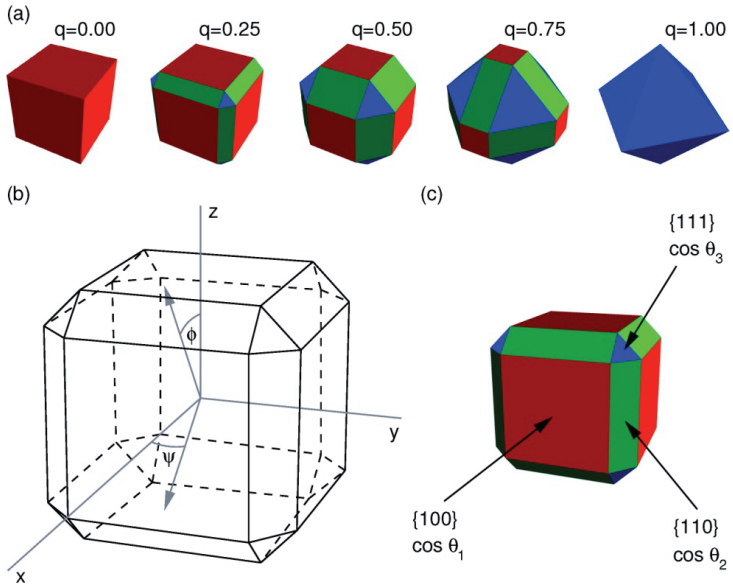

Figure A5.3: The truncated cube model for several values of the truncation parameter q ∈ [0, 1]. (b) A schematic representation of the model for q =0.30 which shows the truncated cube in its initial configuration, i.e., the normals of the {100} facets are axis-aligned and its centre coincides with the origin. We also indicated the azimuthal angle ψ and the polar angle φ. To keep the picture clear, we did not show the interface or the height z, which is zero in this case. (c) The three types of facets: (red) a {100} facet, (green) a {110} facet, and (blue) a {111} facet. The figure also shows the corresponding cosine of the contact angle cos θ_i, with i = 1, 2, 3, that is used to describe the surface properties of the respective facets.

Figure A5.3a. We assume that the truncated cube is first scaled by s, then rotated by ψ and subsequently by φ, and finally it is translated by z. Due to the symmetry properties of the truncated cube we can restrict ourselves to $\psi \in [0, \pi/4]$ and $\varphi \in [0, \pi/2]$. Even for this restricted range there are several instances of duplicate orientations, e.g., $\psi \in [0, \pi/4]$ and $\varphi = 0$ gives essentially the same configuration as $\psi = 0$ and $\varphi = \pi/2$. These duplicate configurations are taken into account via congruence in our analysis.

The free energy of adsorption

In the experiments there is an indication that the surface properties of the different facets can vary with the particle concentration, see the main text. Effectively, the ligand covering of the various facets is influenced by the ligand concentration in the ethylene glycol via adsorption-desorption equilibria. To describe this in our model, we assume that the different crystal planes, i.e., the {100}, {110}, and {111} facets, have surface properties that can vary independently of each other, but are otherwise the same for facets of the same type. In this system the free energy of adsorption F can be written as

$$F'(z, \psi, \phi) = \gamma_{12}(A - S_{12}) + \gamma_{1t}S_{1t} + \gamma_{1b}S_{1b} + \gamma_{2t}S_{2t} + \gamma_{2b}S_{2b} + \gamma_{3t}S_{3t} + \gamma_{3b}S_{3b} \quad (2)$$

where γ_{12} is the liquid-air interfacial tension, A is the total surface area of the interface, S_{12} is the surface area excluded from the interface by the presence of the colloid, γ_{it} is the surface tension between facets of type i $(i = 1, 2, 3)$ and the top medium, S_{it} is the total surface area of the facets of type i in contact with the top medium, γ_{ib} is the surface tension between facets of type i and the bottom medium, and S_{ib} is the total surface area of the facets of type i in contact with the bottom medium. Note that we have made the dependence of S_{12}, S_{it}, and S_{ib} on (z, ψ, ϕ) implicit. In this model the microscopic degrees of freedom of the solvent molecules were integrated out to give surface tensions. We further assumed that the interface is not deformed by the presence of the particle: capillary deformation by gravity, electrostatic effects, or contact-angle requirements. These are strong simplifications, but there are too many unknowns regarding the experimental system to justify a more extended model. In this light, the results obtained in the next section should be seen as an indication of the possible behaviour of a truncated cube at a liquid-air or liquid-liquid interface, rather than a full theoretical description of the phenomenology in the experimental system. We will come back to the quality of these results in the discussion.
To simplify the calculations we can reduce Eq. (2) by subtracting a constant contribution to the free energy of adsorption

$$F'(z,\psi,\phi) = F(z,\psi,\phi) - [\gamma_{12}A + \gamma_{1b}(S_{1t} + S_{1b}) + \gamma_{2b}(S_{2t} + S_{2b}) + \gamma_{3b}(S_{3t} + S_{3b})]; \quad (3)$$

$$= (\gamma_{1t} - \gamma_{1b})S_{1t} + (\gamma_{2t} - \gamma_{2b})S_{2t} + (\gamma_{3t} - \gamma_{3b})S_{3t} - \gamma_{12}S_{12}; \quad (4)$$

$$= \gamma_{12}[\cos\theta_1 S_{1t} + \cos\theta_2 S_{2t} + \cos\theta_3 S_{3t} - S_{12}] \quad (5)$$

where we set the shifted free energy F' to zero when the colloid is completely immersed in the bottom medium. In the last step [Eq. (5)] we used Young's equation[32]

$$\gamma_{it} = \gamma_{12}\cos\theta_i + \gamma_{ib}, \quad (6)$$

with θ_i the contact angle corresponding to the (type i facet -top medium -bottom medium) three-phase contact. Figure A5.3c shows the correspondence between the different contact angles and the various facets: the surface properties of the {100} facets are described by θ_1, those of {110} facets by θ_2, and those of the {111} facets by θ_3. Note that the θ_i are determined by material properties, whereas ψ and φ are variables in our theory. Using the above equations we can now write the dimensionless free energy of adsorption as

$$f(z,\psi,\phi) \equiv \frac{F'(z,\psi,\phi)}{\gamma_{12}S} \quad (7)$$

$$= \cos\theta_1 r_{1t} + \cos\theta_2 r_{2t} + \cos\theta_3 r_{3t} - r_{12} \quad (8)$$

with $r_{it} \equiv S_{it}/S$ and $r_{12} \equiv S_{12}/S$. Note that the dependence of f on the level of truncation q and the surface properties and media (via the contact angles θ_i) is implicit in Eq. (7). Moreover, Eq. (7) is independent of the size s of the particle.

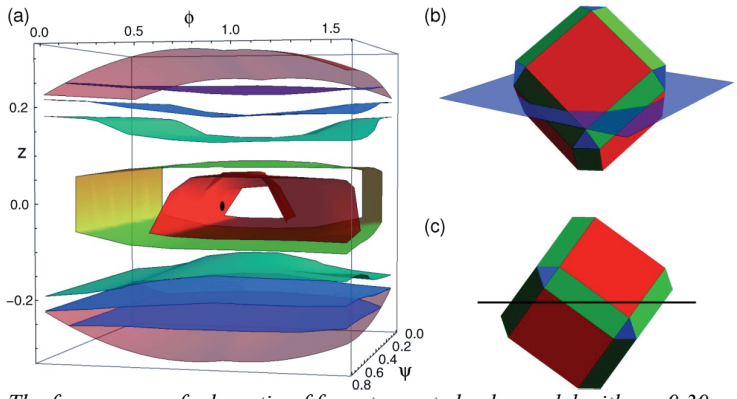

Figure A5.4: The free energy of adsorption f for a truncated cube model with q =0.30 and cos θ_i = 0, for i = 1, 2, 3. Note that this choice for the contact angles ensures that adsorption is completely determined by excluded surface area considerations, also see Eq. (7). (a) A contour plot of the three-dimensional (3D) free-energy landscape: f as a function of the adsorption depth z, the azimuthal angle ψ, and the polar angle φ. The top and bottom red surface indicate for which z value the truncated cube just touches the interface, for a given ψ and φ. From blue to red the contours give f = −0.05, −0.10, −0.15, −0.20, and −0.22. The location of the free-energy minimum is indicated using a black dot. For this particular system we find that f(z, ψ, φ)min ≈−0.24 and that (z, ψ, φ)min ≈ (0.00, 0.25π, 0.30π). (b) The truncated cube in its equilibrium position; one of the {111} facets is pointing in the direction of the z-axis. The translucent blue square indicates the interface. (c) A side view of the truncated cube in this equilibrium position, the thick black line indicates the interface.

For a given q, θ_1, θ_2, and θ_3, Eq. (7) gives rise to a three-dimensional (3D) free energy of adsorption landscape, see Figure A5.4 for an example. This landscape was established by numerically determining the values of r_{1t}, r_{2t}, r_{3t}, and r_{12} on a (z, ψ, φ) grid, which can be easily accomplished using the triangular-tessellation technique described in refs[33, 34]. In the case of a faceted particle our technique's results are exact. The normalization in Eq. (1) allows us to directly obtain the fractional values r_{it} and r_{12}. In the following we take $z \in [-0.4, 0.4]$, $\psi \in [0, \pi/4]$, and $\varphi \in [0, \pi/2]$ with 100 equidistant steps for each of these parameters. Whenever s = 1, the radius of a circumscribed sphere for our truncated cube is always smaller than 0.4. This implies that our choice of $z \in [-0.4, 0.4]$ always samples the full range of adsorption configurations.

The thermodynamic equilibrium is assumed in the minimum of the free-energy landscape, i.e., the z, ψ, and φ combination for which f has the lowest value; we will denote this minimum as $(z, \psi, \varphi)_{min}$. This point can be easily approximated by searching through our free-energy landscape on a grid for the (z, ψ, φ) combination that gives the lowest value of f. The density of grid points (100^3) allows us to approach the actual minimum $(z, \psi, \varphi)_{min}$ to within a sufficient level of precision to justify further analysis. Note that the presence of metastable minima in the free energy of adsorption is not taken into consideration by analysing the lowest free-energy value only.

Results of our theoretical study

An advantage of our model is that the r_{it} and r_{12} only have to be determined only once for a given q in order to establish $f(z, \psi, \varphi)$ for different values of θ_i. To probe the effect of different surface patterning on $(z, \psi, \varphi)_{\min}$, or equivalently different ligand concentrations on the facets, we varied $\cos \theta_i \in [-1, 1]$ in equidistant steps of 0.03.

Figure A5.5 shows the distribution of $(z, \psi, \varphi)_{min}$ in the 3D (z, ψ, φ) landscape upon varying the contact angles for q =0.30. Note that the distribution of $(z, \psi, \varphi)_{min}$ is not homogeneous. In fact, an analysis of our results shows that the equilibrium orientations of the truncated cube can be roughly divided into three categories: (i) the normal of one of the {100} facets is pointing in the direction of the z-axis, (ii) the normal of one of the {110} facets is pointing in the direction of the z-axis, and (iii) the normal of one of the {111} facets is pointing in the direction of the z-axis, also see Figure A5.6. We refer to these three configurations as the 'prototypical' configurations. This rough division assumes that, for instance, the state where the particle is adsorbed at depth z is equivalent to the one where it is adsorbed at depth −z. Moreover, we assume that $|\psi` - \psi| < 0.03\pi$ and $|\varphi` - \varphi| < 0.03\pi$ constitute the same configuration, where $\psi`$ and $\varphi`$ are the angles corresponding to the prototypical orientation of one of the three categories. The tolerance in the depth z is considered on a case-by-case basis.

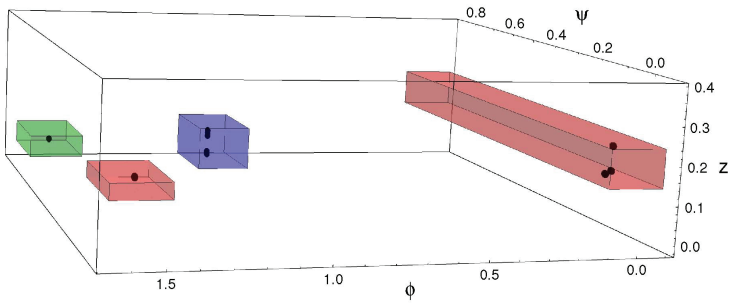

Figure A5.5: The distribution of equilibrium adsorption configurations (z, ψ, φ)min (black dots) obtained by varying cos θi ∈ [−1, 1] (i = 1, 2, 3) in equidistant steps of 0.03 for a truncated cube with q =0.30. Note that the distribution of (z, ψ, φ)min is not homogeneous, only a few of the possible values of (z, ψ, φ) are assumed. The red, green, and blue translucent boxes indicate to which 'prototypical' configuration we assign these (z, ψ, φ)min points. Configuration in the red boxes correspond to adsorption with the normal of one of the {100} facets pointing in the direction of the z-axis, configurations in the green box correspond to adsorption with the normal of one of the {110} facets pointing in the direction of the z-axis, and configurations in the blue box correspond to the normal of one of the {111} facets pointing in the direction of the z-axis; also see Figure A5.6, which uses the same colour coding. The two red boxes accommodate a single congruence class.

Working backwards we can now find the three values of cos θ_i for which the truncated cube is in one of the prototypical equilibrium configurations, see Figure A5.6, which shows this correspondence. Here we only give cos θ_1, cos $\theta_2 \in [-1, 1]$ and cos $\theta_3 \in [0, 1]$, since the graph is point symmetric in the origin, which can be easily shown by considering the signs of the cos terms in Eq. (7). We find that the {100}-prototypical equilibrium configurations is the most common and there is a slightly greater number of {111} than {110} equilibrium configurations. However, it should be noted that interpreting the graph on the basis of surface area alone can be misleading, since $\theta_i \gtrsim 150°$ and $\theta_i \lesssim 30°$ represent atypical values of the contact values, i.e., $|\cos\theta| \lesssim 0.87$ is reasonable.

Following the approach that we employed for q =0.30, we can study the influence of the surface properties of the different types of facet as a function of the level of truncation *q*, also see Figure A5.7-Figure A5.10. Note that for q = 0 there are only two types of equilibrium configurations, one where one of the {100} facets is pointing upward, and one where one of the '{110} facets' is pointing upward. The first can be explained by the particle minimizing its contact area with the unfavoured medium, whilst still excluding a piece of the interface (thereby lowering its free energy). The second arises when there is a limited difference between the two media; the colloid can lower the free energy by excluding the maximum amount of surface area from the interface. N.B., for a cube (q = 0) the two prototypical configurations are the only two possible configurations within the confines of our model, i.e., there is no spread in the $(z, \psi, \varphi)_{min}$. For small levels of truncation q =0.15, see Figure A5.8, the division into two prototypical equilibrium configurations ({100} and {110}) remains. The spread of the $(z, \psi, \varphi)_{min}$ around these configurations increases. The surface properties of the {110} facets have a small influence on the configurations that are assumed by the truncated cubes, as can be seen in Figure A5.8. However, the presence of {111} facets do not seem to affect the equilibrium configurations sufficiently to cause the third prototypical configuration to appear.

Further truncation of the cube, see Figure A5.6 for the *q =0.30* and Figure A5.9 for the *q =0.45* result, respectively, appears to promote the {111} prototypical configuration. It is likely that a greater level of truncation destabilizes the {110} configuration in favour of the {111} configuration, because the maximum amount of surface area that can be excluded from the interface in either configuration becomes comparable. This hypothesis was confirmed by considering truncated cubes with homogeneous surface properties, as well as other ways of truncating a cube[35]. However, when the level of truncation is great, see Figure A5.10 for the q =0.60 result, the truncated cube becomes rather spherical. This implies that there is no longer a limited number of favoured orientations on the basis of excluded surface area arguments. As can be appreciated from Figure A5.10 this results in a more coarse distribution of 'prototypical' equilibrium configurations, as well as the appearance of three more configurations.

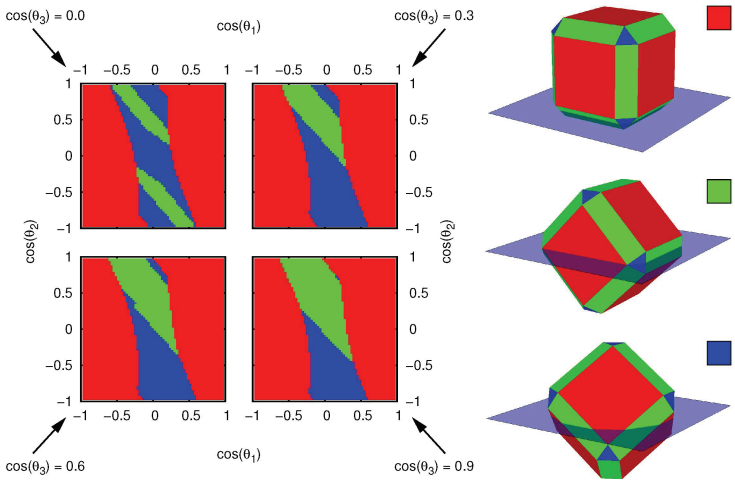

Figure A5.6: The equilibrium configurations that present themselves for a truncated cube with truncation level q =0.30 as a function of its surface properties. The sub-plots show four cos θ3 slices: top, cos θ3 =0.0 (left) and cos θ3 =0.3 (right); bottom, cos θ3 =0.6 (left) and cos θ3 =0.9 (right). These indicate the prototypical equilibrium configuration that is assumed by the truncated cube as a function of cos θ1 and cos θ2. (legend) The three equilibrium configurations and associated colour code: (red) the normal of one of the {100} facets is pointing in the direction of the z-axis, (green) the normal of one of the {110}facets is pointing in the direction of the z-axis, and (blue) the normal of one of the {111} facets is pointing in the direction of the z-axis.

Discussion and Outlook

Let us first consider the likelihood of interfacial adsorption. For a spherical particle with homogeneous surface properties the minimum difference in free energy ΔF between the adsorbed and desorbed state is easily shown to be given by $\Delta F = \pi a^2 \gamma_{12}(1 - |\cos\theta|)^2$. Here, a is the radius of the sphere, θ is the (air/liquid)-sphere-liquid contact angle, and γ_{12} is the interfacial surface tension. We can use this value to estimate what the strength of adsorption for our nanocrystals might be. We assume that the nanocrystals are at the air/toluene interface, based on previous experimental observations for similar systems.[36, 37] The surface tension of the air/toluene interface is given by $\gamma_{12} \approx 2.8 \cdot 10^{-2}\ \mathrm{Nm}^{-1}$.[38] Note that finite values of cos θ lower ΔF . However, for realistic values of θ this reduction in ΔF is no more than a factor of 10, with the maximum in ΔF assumed when cos θ = 0. The smaller nanocrystals, which have a diameter of 5.4 nm, therefore adsorb to the interface with at most $\Delta F \approx 1 \cdot 10^2\ k_B T$, where k_B is Boltzmann's constant and T is the temperature. The larger nanocrystals, which have diameter of 9.9 nm, adsorb with at most $\Delta F \approx 5 \cdot 10^2\ k_B T$. This simple estimate gives some ab initio justifications of the applicability of our theoretical results to the experimental system. Under ideal circumstances there will be a strong influence of the interface on the nanoparticles, which drives these towards their equilibrium adsorption configurations. It should, however, be mentioned that these estimates do not factor into account surface-tension lowering effects such as the presence of surfactants at the interface or pollutants in the toluene.

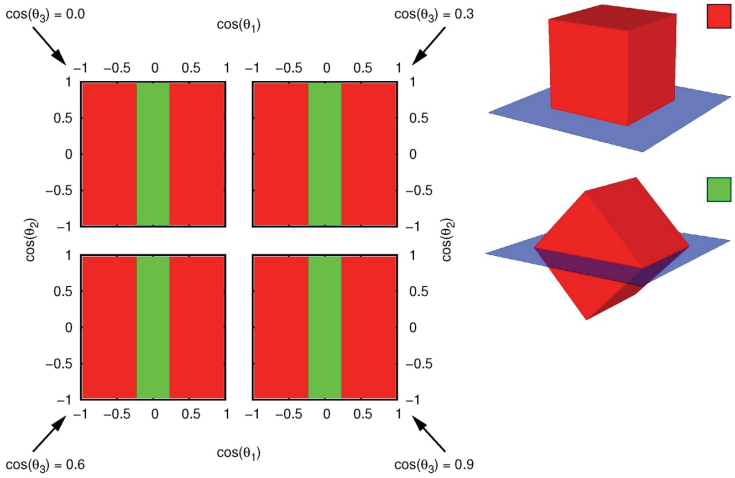

Figure A5.7: The equilibrium configurations that present themselves for a cube (q = 0) as a function of its surface properties. The sub-plots indicate the (prototypical) equilibrium configuration that is assumed by the cube as a function of cos θ1 and cos θ2, for various cos θ3 values. (legend) The two equilibrium configurations and associated colour code. Note that the type of configuration only depends on the surface properties of the red {100} facets, as expected for this level of truncation.

Our results indicate that the three experimentally observed configurations can be explained within the framework of adsorption-desorption equilibria for the ligand concentration on the various facets. Indeed, upon varying the surface properties of the three types of facet - by modifying the contact angle -we theoretically found the possible equilibrium adsorption configurations to coincide with the orientations of the particles in the superstructures that formed at the interface. Moreover, it was experimentally observed that the level of truncation for the larger nanocrystals (9.9 nm) was less than that for the smaller variety (5.4 nm). This could explain the fact that the honeycomb structures were only observed for the smaller nanocrystals, since the {111} adsorption configuration does not occur for smaller levels of truncation, within the confines of our model.

We therefore propose the following explanation for our observations. At low concentrations of the truncated cubes the adsorption-desorption equilibrium for the ligands covering the facets is shifted towards the ligands being preferentially adsorbed in the ethylene glycol. When the truncated particles come together there is irreversible and disordered aggregation. However, for higher particle concentrations the equilibrium shifts to a sufficiently high ligand covering of the facets that immediate aggregation is prevented. Moreover, we believe that for these systems the surface properties of the nanoparticles are such that the equilibrium adsorption configuration is of the {100} or the {110} type, where the latter is preferentially assumed for lower particle concentrations. These configurations lead to the formation of two-dimensional (2D) rod-like ({110}) and square assemblies ({100}) by oriented attachment via the {100} facets, respectively. That is to say, for the {100}-like

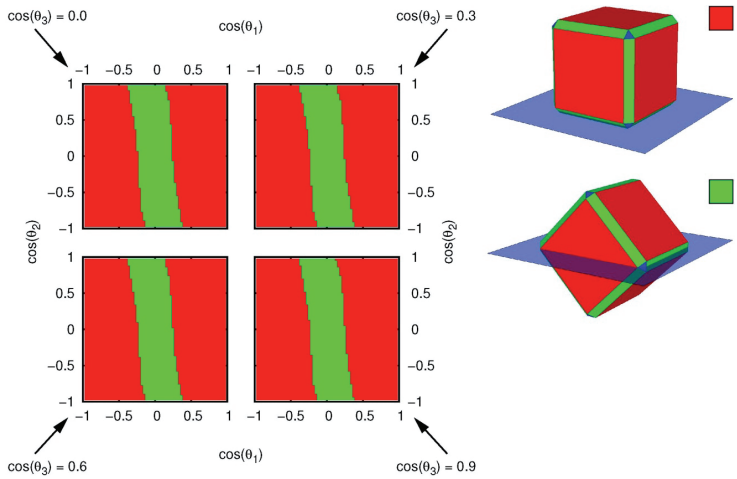

Figure A5.8: The equilibrium configurations that present themselves for a truncated cube with truncation level q =0.15 as a function of its surface properties. The sub-plots indicate the (prototypical) equilibrium configuration that is assumed by the truncated cube as a function of cos θ1 and cos θ2, for various cos θ3 values. (legend) The two equilibrium configurations and associated colour code. Note that there is a small dependence on the surface properties of the {110} facets (cos θ2) for this level of truncation. However, the surface properties of the {111} facets do not appear to play a role.

configuration, four of the {100} facets are oriented perpendicular to the interface, allowing for oriented attachment via these facets in the plane of the interface, which gives rise to square structures. For the {110} configuration, only two (opposing) {100} facets are perpendicular to the interface, allowing for oriented attachment that results in linear structures. Upon increasing the nanoparticle concentration from low to intermediate values, the ligand adsorption/desorption equilibria are shifted resulting in a different nanoparticle surface pattern. This surface pattern leads to preferential adsorption at the interface of the {111} type and subsequent oriented attachment via the (now) exposed {110} facets of the particles into honey-comb superstructures. The latter situation does not, however, occur when the level of truncation is too small to allow for the {111} configuration to be stable.

It is important to note that our results (and the conclusions we based on these) were obtained using a simple model for the adsorption of a particle at a liquid-liquid or liquid-air interface. We leave a full investigation of the experimental phenomenology by theoretical or simulation means as an open problem for future study. An interesting question for such a study to answer is if a simple model that incorporates particle-concentration-based ligand adsorption/desorption equilibria, is capable of capturing the shift from the {100} towards the {111} equilibrium configuration, whilst at the same time showing a lower ligand covering of the facets which we believe to mediate the oriented attachment. A conformation of this shift would give strong support for our hypothesis that the interface and ligand adsorption/desorption play a crucial role in determining the structure of the assemblies that we observed to form by oriented attachment.

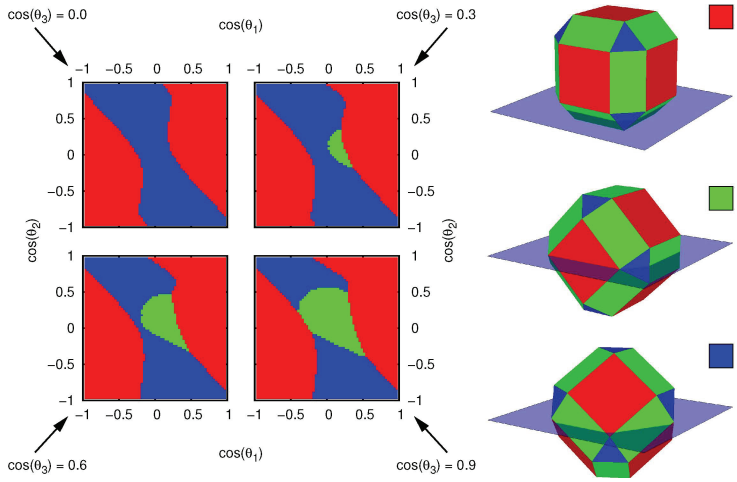

Figure A5.9: The equilibrium configurations that present themselves for a truncated cube with truncation level q =0.45 as a function of its surface properties. The sub-plots indicate the prototypical equilibrium configuration that is assumed by the truncated cube as a function of cos θ1 and cos θ2, for various cos θ3 values. (legend) The three equilibrium configurations and associated colour code.

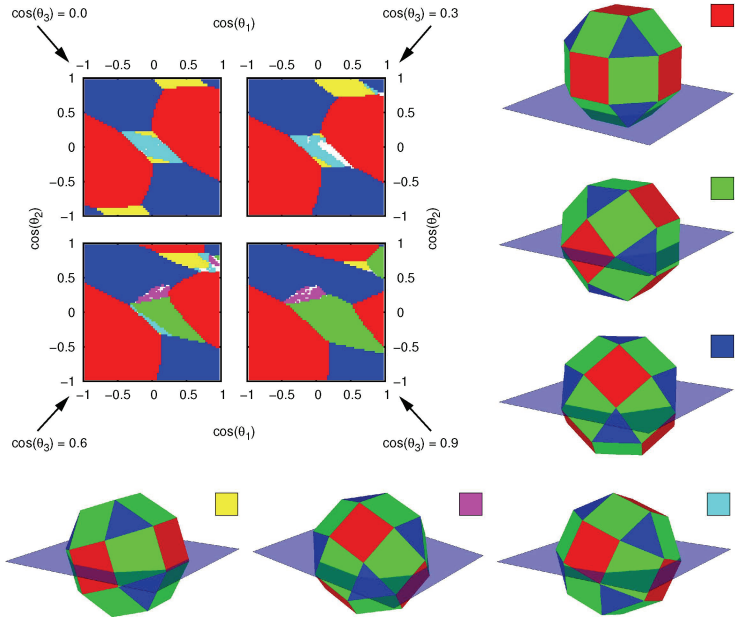

Figure A5.10: The equilibrium configurations that present themselves for a truncated cube with truncation level q = 0.60 as a function of its surface properties. The sub-plots indicate the prototypical equilibrium configuration that is assumed by the truncated cube as a function of cos θ_1 and cos θ_2, for various cos θ_3 values. (legend) The six prototypical equilibrium configurations and associated colour codes. (red) one of the {100} facets is pointing in the direction of the z-axis, (green) one of the {110} facets is pointing in the direction of the z-axis, (blue) one of the {111} facets is pointing in the direction of the z-axis, (yellow) the {210} 'facet' is pointing in the direction of the z-axis, (magenta) the {221} 'facet' is pointing in the direction of the z-axis, and (cyan) the {321} 'facet' is pointing in the direction of the z-axis. The white points in the sub-plots indicate for which cos θ_i combinations we were unable to assign a prototypical equilibrium configuration.

Chapter 6

Two fold emission from the s-shell of PbSe/CdSe core/shell quantum dots

The optical properties of PbSe/CdSe core/shell quantum dots with core sizes smaller than 4 nm are reported in the 5–300 K range. The photoluminescence spectra show two peaks, which become increasingly separated in energy as the core diameter is reduced below 4 nm. It is shown that these peaks are due to intrinsic exciton transitions in each quantum dot, rather than emission from different quantum dot sub-ensembles. Most likely, the energy separation between the peaks is due to inter-valley coupling between the L-points in the Brillouin scheme of rocksalt PbSe and electron hole exchange. The temperature dependence of the relative intensities of the peaks implies that the two emitting states are not in thermal equilibrium and that dark exciton states must play an important role.

6.1 Introduction

Nanocrystalline quantum dots (QDs) of Pb-chalcogenides have attracted increasing interest in recent years since these systems hold promise for optoelectronic applications in the near- and mid-IR (such as photodetectors, LEDs, photonic switches, and photovoltaic cells).[1-3] Two routes have been developed for the fabrication of Pb-chalcogenide nanocrystals (NCs): vapour-phase epitaxial deposition methods, which result in QDs embedded in a solid matrix, and wet chemical syntheses, which yield colloidal suspensions of organically capped NCs. For instance, PbTe QDs embedded in a coherent CdTe matrix have been grown by molecular beam epitaxy and annealing.[4] Colloidal PbTe QDs are also available, and recently well-defined PbTe/CdTe core/shell colloidal QD systems have been reported.[5] Colloidal core/shell QDs and hetero-NCs with other geometries are of particular interest since the ability to join different materials in one particle opens up new possibilities to engineer their properties.[6] Furthermore, superlattices consisting of self-assembled colloidal PbSe NCs hold promise for photovoltaic applications and photon detection in the near-IR, as well as for transistor type devices.[2, 7-10]

The effective masses of the electron and hole in Pb chalcogenides are small, leading to large exciton Bohr radii (e.g., 46 nm for PbSe).[10, 11] This results in strong quantum confinement for relatively large NCs, making it possible to tune the optical properties of Pb-chalcogenide NCs over a wide spectral range by controlling their size. For example, the bandgap of PbSe QDs can be tuned from the bulk value (0.3 eV) up to about 1.5 eV by decreasing the NC diameter from 100 to 2 nm.[12] The electronic (fine) structure of Pb-chalcogenide QDs is complex, and there are still several unresolved issues. These materials crystallize in the rock-salt structure and have an electronic band structure that differs considerably from that of typical II–VI compounds. The maximum of the valence band and the minimum of the conduction band are both situated at the L-point in the Brillouin zone (Figure 6.1). Since there are four L-points per fcc Brillouin zone the fundamental bandgap is eight-fold degenerate if spin degeneracy is included. This yields a 64-fold degenerate lowest exciton state ($1S_h$–$1S_e$). This degeneracy is partially lifted by a number of effects (viz., intraband and inter-valley couplings and electron–hole exchange), leading to an exciton fine structure that is not yet completely investigated. In the case of PbSe QDs, tight binding,[13] pseudo-potential,[14] and first-principle calculations[15, 16] have been used to reveal the impact of valence-to-conduction-band coupling and coupling between the four L-points (i.e., inter-valley coupling) on the electronic structure in the strong quantum confinement regime. Electron–hole exchange is also important. In combination with the coupling effects this exchange leads to an intricate exciton fine structure consisting of a number of bright and dark states. These effects depend critically on the size and shape of the PbSe NC and possibly also on the surface termination, which makes it difficult to obtain a comprehensive experimental and theoretical picture of the exciton fine structure in PbSe NCs and in Pb-chalcogenide NCs in general. Further experimental investigations of the

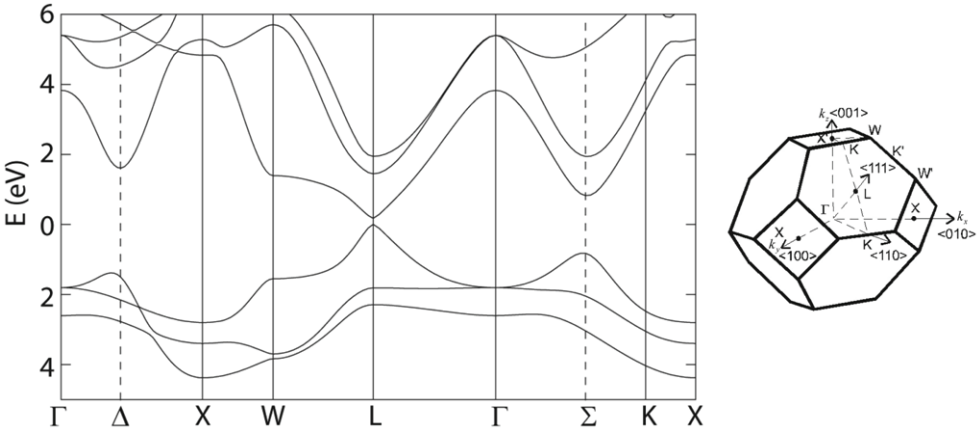

Figure 6.1: Band structure of bulk PbSe (left). The zero of energy is located at the top of the valence band.[13] The first Brillouin zone for a fcc lattice is also shown (right).

electronic (fine) structure of well-defined PbSe QDs is therefore highly desirable, particularly for PbSe diameters below 4 nm.

Here we report a comprehensive study of the (time-resolved) photoluminescence (PL) of small (<4 nm) PbSe NCs in a PbSe/CdSe core/shell colloidal QD system over a broad temperature range (5–300 K). The samples investigated in this work consist of dilute colloidal suspensions (10^{-7} mol L^{-1}) of QDs and therefore Förster energy transfer and other forms of interaction between the QDs can be neglected. We have used a recently reported a Pb for Cd ion-exchange reaction to convert small PbSe NCs (≈4 nm diameter) into PbSe/CdSe core/shell hetero-NCs.[17] Three different batches of parent PbSe NCs with average diameters of 3.7, 4.0, and 4.2 nm were used. The overall size and shape of the NCs remain unchanged upon ion-exchange, hence the duration of the ion-exchange reaction defines the thickness of the CdSe shell and the size of the remaining PbSe core. This allows the study of increasingly smaller PbSe NCs that are chemically and photochemically stable and have a well-defined PbSe/CdSe interface. The PbSe rock-salt and the CdSe wurtzite or zinc-blende lattices do not alloy but have a commensurate Se sub-lattice. Therefore, the PbSe/CdSe hetero-interface consists of Se (111) planes that are nearly strain free.[18] The PL of the PbSe/CdSe core/shell colloidal QDs investigated in this work is strong and decreases gradually in intensity from 5 K to room temperature. Strikingly, the PL spectra consist of two peaks, with a separation that increases with decreasing volume of the PbSe cores. A similar behavior is observed for PbSe colloidal QDs. These two emission peaks are ascribed to two bright exciton fine-structure states in the 64-manifold $1S_e$ –$1S_h$ state of the PbSe QDs. These two emitting states are also reflected in the excitation spectra. The splitting between the states is most likely due to inter-valley coupling and electron–hole exchange. Intriguingly, the two states are not in thermal equilibrium.

6.2 Experimental

The colloidal PbSe/CdSe core/shell QDs investigated in this work were synthesized in two steps. First, oleic acid capped PbSe NCs were grown following the method developed by Houtepen et al.[19] Subsequently, the PbSe QDs were converted into PbSe/CdSe core/ shell hetero-NCs using a Pb for Cd ion-exchange method.[17, 20] The syntheses were carried out under an inert atmosphere. Three different batches of PbSe QDs with average diameters of 3.7, 4.0 and 4.2 nm (10% size dispersion) were used as parent NCs. The diameter of the parent PbSe QDs was determined by TEM, while the core diameter of PbSe/CdSe core/shell QDs was estimated from the spectral position of the lowest energy absorption peak using an empirical sizing curve,[12] under the assumption that this transition involves states that are primarily localized in the PbSe core. The validity of this assumption has been demonstrated by recent studies correlating the optically estimated core size with those determined from TEM analyses.[21] HR-TEM measurements were performed using an aberration-corrected Titan microscope operating at 300 kV. Absorption spectra were measured using a Perkin-Elmer Lambda 950 UV/VIS/IR absorption spectrophotometer. PL spectra and PL excitation spectra were recorded using an Edinburgh Instruments FLS920 spectrofluorometer. For the PL excitation spectra a Halogen lamp was used as the excitation source. PL decay time measurements were performed by using an excimer laser pumped tunable dye laser (Lambda Physik LPX 100 and LPD3000) as the pulsed excitation source (20 ns pulses with a 10 Hz repetition rate) and the spectrofluorometer described above to detect the emission. The dye Coumarin 102 was used and a wavelength of 500 nm was selected. Decay curves were obtained using a Tektronix 2430 digital oscilloscope (500 MHz), interfaced with a PC.

6.3 Results and discussion

6.3.1. General Characterization and Room Temperature Optical Spectra

Low resolution transmission electron microscopy (TEM) images of PbSe QDs before and after the Pb for Cd ion-exchange reaction are shown in Figure 6.2A and Figure 6.2C respectively. A schematic representation of the cation-exchange process is also presented (Figure 6.2B). Prior to ion-exchange the parent PbSe QDs have a multifaceted nearly spherical shape with a diameter of 3.7 nm (10% standard deviation). Batches of PbSe QDs with a diameter of 4.0 and 4.2 nm were also used as parent NCs. The ion-exchange reaction leads to the formation of PbSe/CdSe core/shell QDs in which the PbSe cores progressively shrink as the CdSe shell grows. As a result the PbSe core diameter decreases with increasing ion-exchange time. The total diameter and shape of the QDs remain the same, while the core develops a faceted octahedral like shape (see Figure 6.3d–f for illustrative

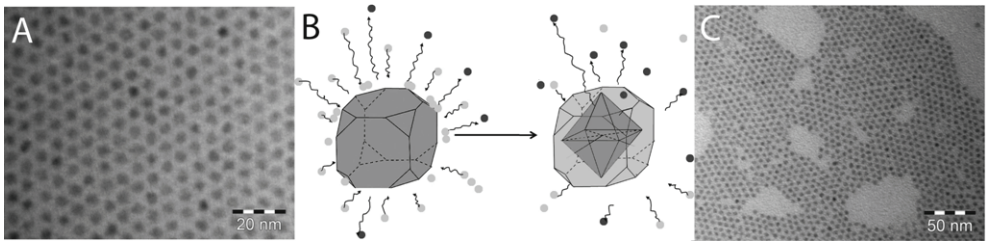

Figure 6.2: A) TEM image of the parent PbSe QDs (3.7 nm in diameter). B) Schematic diagram of the ion-exchange process (light grey and dark gray dots represent Cd and Pb atoms, respectively). C) PbSe/CdSe core/shell QDs obtained after 120 min of ion-exchange time (3.7 nm in total diameter).

high-resolution (HR) TEM images). This indicates that ion-exchange proceeds faster at the {111} surfaces of PbSe (truncated corners in Figure 6.2B). The PbSe/CdSe hetero-interface consists predominantly of Se {111} planes and appears to be atomically sharp, as expected on the basis of the very small lattice mismatch (≈1%),[17] and negligible atomic diffusion between the rock-salt (RS) PbSe and zinc blende (ZB) CdSe phases. The immiscibility of the two materials results from the different co-ordination numbers of the atoms in the two types of crystal structure (4-fold in ZB, 6-fold in RS).[6] The small size and octahedral-like shape of the PbSe cores makes it difficult to reliably estimate the core dimensions from TEM images. Therefore, the core 'diameter' in the PbSe/CdSe core/shell QDs was estimated from the spectral position of the lowest energy optical absorption transition using an empirical sizing curve,[12] under the assumption that this transition involves states that are primarily localized to the PbSe core. The validity of this assumption has been demonstrated by recent studies correlating the optically estimated core size with those determined by TEM analysis.[21] Figure 6.3A–C presents the room temperature absorption and PL spectra of 3.7 nm PbSe QDs and PbSe/CdSe core/shell QDs obtained with PbSe core diameters of 3.2 and 2.1 nm respectively. Illustrative HR-TEM images of these hetero-NCs are presented in Figure 6.3D–F. The absorption spectra of the parent PbSe NCs show two sharp absorption peaks, assigned to the $1S_h$–$1S_e$ and $1P_h$–$1P_e$ transitions, respectively, in agreement with previous reports.[22, 23] The $1S_h$–$1S_e$ emission peak is located at 0.88 eV is slightly red shifted with respect to the corresponding absorption peak and has a full width at half maximum of 90 meV. As discussed above, the growth of a CdSe shell by Pb-for-Cd exchange leads to a reduction of the PbSe core size (Figure 6.3D–F), and markedly changes the optical properties. The lowest energy absorption peak and the emission peaks shift to higher energies and become broader over time during the Pb-for-Cd ion-exchange reaction. At room temperature the maximum of the emission peak shifts from 0.88 eV (3.7 nm PbSe) to 0.95 eV (3.2 nm PbSe core), and then to 1.10 eV (2.1 nm PbSe core). Similar results have been reported in the original work by Pietryga et al.[17] and in recent work by De Geyter et al.[21] The blue shift of the absorption and emission spectra can be ascribed to the decreasing size of the remaining PbSe core in the PbSe/CdSe core/shell hetero-NC, under the understanding that the exciton remains confined in the PbSe core (i.e., type-I localization regime). Resonant scanning tunneling microscopy on single PbSe/CdSe

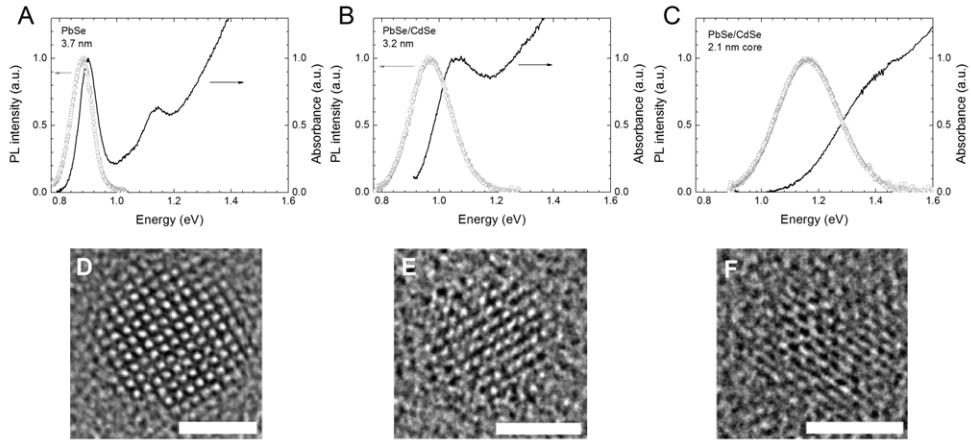

Figure 6.3: A) Room-temperature absorption (black line) and photoluminescence spectra (circles) of PbSe NCs (3.7 nm in diameter), B) PbSe/CdSe core/shell quantum dots of 3.7 nm with a core of 3.2 nm, and C) PbSe/CdSe core/shell quantum dots of 4.2 nm with a core of 2.1 nm (different PbSe NC parent batch). The total diameter of the parent PbSe NCs is preserved during the ion-exchange. HR-TEM images of the 3.7 nm PbSe NC (D) and PbSe/CdSe core/shell quantum dots obtained after 5 min (E) and 60 min (F) of ion-exchange. The scale bars correspond to 2 nm.

core/shell QDs and optical spectroscopic investigations indicate that these hetero-NCs can best be described as a type-I system in which the s-electron wave function is centered in the PbSe core (albeit partially extending into the CdSe shell) and the hole wave function is completely confined into the core.[21, 24] It will be shown below that the broadening of the PL spectrum at room temperature is mainly reflective of the intrinsic electronic effects taking place in the small PbSe QDs.

6.3.2 Temperature-Dependent Photoluminescence Spectra

Figure 6.4 presents the PL spectra of PbSe/CdSe core/shell QDs with decreasing PbSe core diameters at 5 K. It is clear that the broad PL spectra consist of two peaks. The spectra (energy scale) were fit to a sum of multiple Gaussian bands using the minimum number of Gaussians needed to accurately describe the spectra. In all cases the best fit was obtained with a convolution of only two peaks. The solution was unique in terms of the position, width, and total area of the Gaussians needed to accurately describe the spectra. Moreover, the spectra of different samples emitting at the same energies gave essentially the same results. The width of the peaks is given in Figure 6.5. The overview in Figure 6.5 gives the full width half maximum (FWHM) of the two contributions to the emission peak versus the temperature. Both peaks are temperature independent in a range of 5-100 K for all samples. Very probably, the peak width reflects the distribution in the volume of the PbSe cores in the sample (Inhomogeneous broadening). Above ~100 K the broadening slowly increases. This can be attributed to additional thermal broadening. The lowest and highest energy

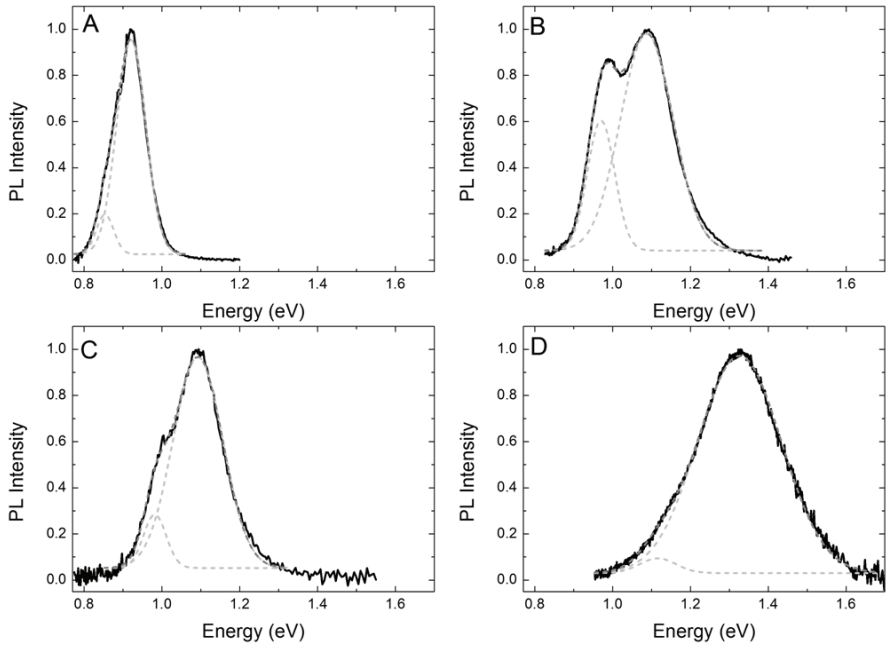

Figure 6.4: Low temperature (5 K) photoluminescence spectra of PbSe/CdSe core/shell QDs with varying core diameters. The PL spectra are fitted to a convolution of two Gaussian peaks (dashed curves). A) 3.2 nm PbSe core, total diameter 3.7 nm. B) 2.1 nm PbSe core, total diameter 3.7 nm. C) 2.1 nm PbSe core, total diameter 4.2 nm. D) 1.1 nm PbSe core, total diameter 3.5 nm.

peaks will be denoted hereafter as $P_1$and P_2 respectively. The intensity of each transition ($I(P_1)$ and $I(P_2)$) is given by the area under the peaks. Figure 6.4 shows that the relative intensities of the two PL peaks differ from case to case, but are reproducible for different samples emitting in the same spectral range. The peak at lower energy is the weaker one in most samples, except in those emitting at ≈1 eV (Figure 6.6).

The observation of two PL peaks at low temperatures and under low excitation densities is unusual and striking. We first demonstrate that the two peaks are not due to two different types of QDs in the sample, but rather reflect two intrinsic emitting states in each PbSe/CdSe core/shell QD. The evidence that the two peaks are due to two different intrinsic states in each of the PbSe/CdSe core/shell QDs is two-fold. Firstly, if the two peaks were due to emission from different QDs in the sample (i.e., two different sub-ensembles) this would imply either a bimodal distribution in the size of the PbSe QDs or of the PbSe cores in the PbSe/CdSe core/shell QDs. However, TEM studies (Figure 6.2 and Figure 6.3) show no evidence of a bimodal size distribution. Furthermore, the double emission peaks were reproducibly observed in PbSe/CdSe core/shell QD samples obtained from different syntheses and different batches of parent PbSe NCs (Figure 6.4C) as well as in the PL spectra of plain PbSe QDs. Similar observations have been made by Harbold and Wise.[25]

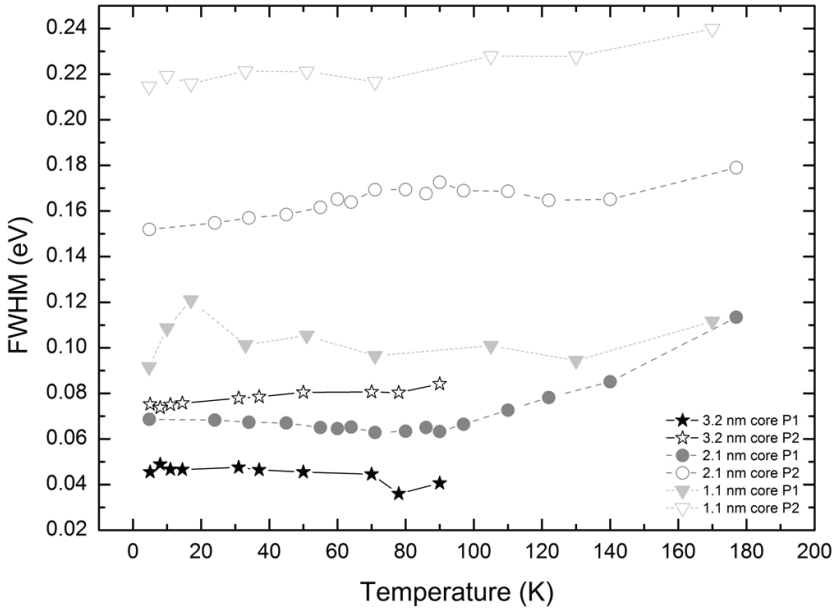

Figure 6.5: Overview of the FWHM of the two peaks of the emission spectra versus the temperature for PbSe/CdSe NCs with a total diameter of 3.7 nm and core diameters of 3.2, 2.1 and 1.1 nm.

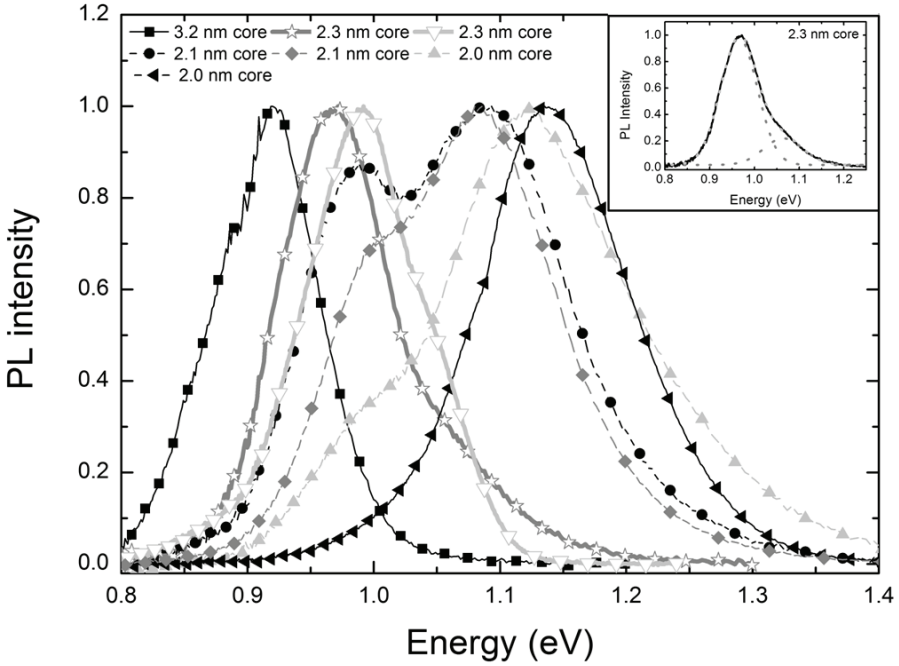

Figure 6.6: Selection of Low temperature (5K) photoluminescence spectra of PbSe(core)/CdSe(shell) QDs showing the trend of the double peaks as a function of the average emission energy. Only the samples around 1 eV show a peak with high intensity at lower energy (inset for the 2.3 nm core).

It is unlikely that different syntheses by different groups would lead to very similar bimodal size distributions. Secondly, further evidence is obtained by analyzing the PL excitation spectra. Figure 6.7 presents the PL excitation spectra obtained while monitoring emission at different spectral positions in the region of the double peaks. When monitoring at high energy (1.15 eV, P_2), it is evident that the lowest-energy excitation peak can be fitted with just one Gaussian, reflecting the contribution of one state. In contrast, when monitoring the excitation spectrum of the low energy peak (0.97 eV, P_1+P_2), two Gaussians are needed to obtain a proper fitting of the lowest energy feature in the excitation spectrum. From this it is evident that the low-energy photoluminescence peak (P_1) partly arises from excitation into the high-energy peak (P_2). Since the nanocrystal suspension is sufficiently dilute (10^{-7} mol·L^{-1}), energy transfer between QDs in the suspension cannot occur, especially at low temperatures when the sample is frozen solid. The above shows that the two peaks observed in the photoluminescence spectra originate from two intrinsic emitting states belonging to the 64-manifold $1S_e$–$1S_h$ exciton state of PbSe. It is evident that both the PL excitation and the luminescence spectra reflect the same two states. Furthermore, the energy separation between the emission and the lowest-energy excitation (absorption) peaks is remarkably large, viz., 220 and 280 meV for the low- and high-energy peaks respectively.

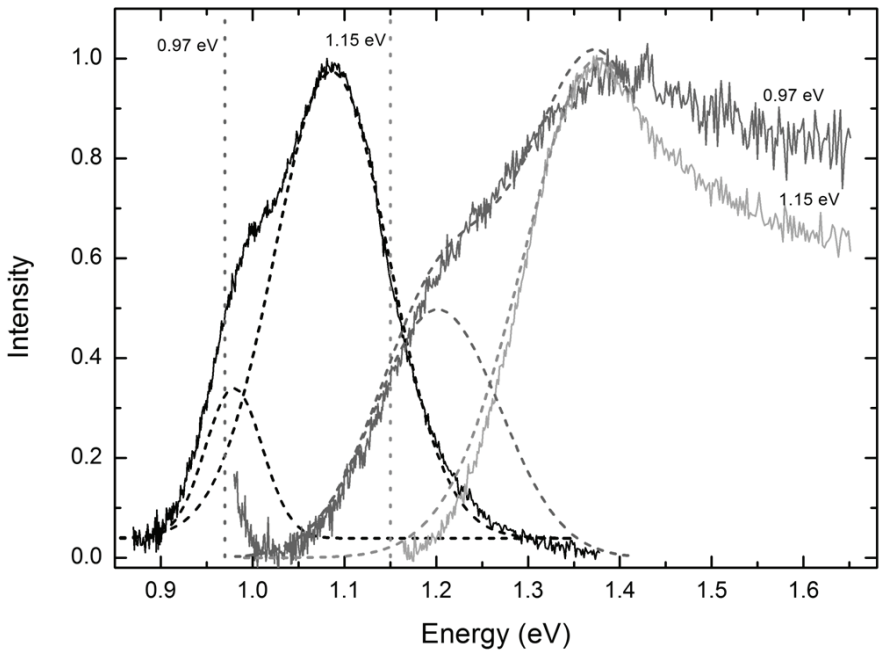

Figure 6.7: Photoluminescence (PL, black solid line) and PL excitation spectra (gray lines) of PbSe/CdSe core/shell QDs with 2.1 nm diameter core (total diameter: 4.2 nm). Excitation spectra were taken while monitoring different PL energies indicated by the dotted lines (0.97 eV, dark gray PLE spectrum, and 1.15 eV, light gray PLE spectrum). The first part of the excitation spectrum at high energy was fitted with a single Gaussian (dashed lines). This Gaussian was used as an invariable parameter to fit the two Gaussians in the excitation spectrum of the low energy side (0.97 eV).

Figure 6.8 presents the PL spectra acquired in the 5–300 K temperature range for a PbSe/CdSe core/shell QD sample with a 2.1 nm diameter core. An additional example is presented online[26] (Figure S2, sample with a 2.3 nm diameter core). The PL spectra can be well described by a convolution of two Gaussian peaks (i.e., P_1 and P_2) at all temperatures. Furthermore, the relative intensities of the two peaks change considerably with increasing temperature. Figure 6.8D shows the temperature dependence of the total PL intensity ($I(P_1)+I(P2)$) and of the relative intensity of the lower energy peak ($I(P_1)/ (I(P_1)+I(P_2))$). It can be seen that $I(P_1)/ (I(P_1)+I(P_2))$ decreases to a minimum when heating from 5 to 90 K and then increases again upon further increasing the temperature. The total PL intensity decreases gradually with increasing temperature. Although the high energy peak (P_2) becomes more dominant at higher temperatures for all samples investigated, there is no evidence that the two intrinsic exciton states are thermally coupled, since the higher-energy state (P_2) remains prominent at 5 K. In case of thermal equilibrium the population of the higher-energy state should be negligible at 5 K.

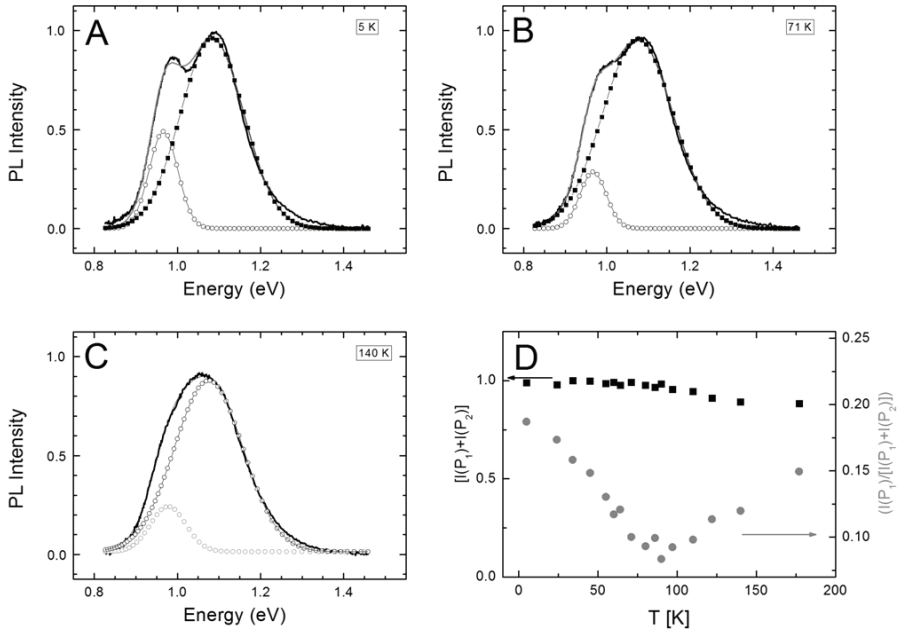

Figure 6.8: A–C) Temperature-dependent photoluminescence spectra of PbSe/CdSe core/shell QDs (60 min of Pb/Cd ion exchange, 3.7 nm total diameter, 2.1 nm core diameter) acquired at the temperatures indicated. The spectra are fitted to a convolution of two Gaussian peaks (dotted curves). D) Total PL intensity (squares), and ratio of the lower-energy peak intensity to the total intensity (circles) as a function of temperature.

The energies of the maxima of the emission peaks $E(P_1)$ and $E(P_2)$ of the PbSe/CdSe core/shell QDs investigated in this work are plotted as a function of temperature in Figure

6.9B. It can be seen that the peak positions are nearly independent of the temperature. Furthermore, both peaks shift to higher energies with decreasing volume of the PbSe core. In addition, the energy separation ($E(P_2)$-$E(P_1)$) increases considerably with decreasing core size, from 70 meV for a 3.2 nm core to 210 meV for a 1.1 nm core (Figure 6.9C). A similar trend is observed for colloidal PbSe QDs in diluted suspensions (10^{-7} mol L^{-1}), which is supported by the observations of Harbold and Wise for PbSe QDs in QD solid films.[25] The values of the PL energy splitting observed for PbSe QDs are also included in Figure 6.9C. Interestingly, in the case of the PbSe/CdSe core/shell QDs, the parent PbSe QDs in solution and the PbSe QDs in QD solids all follow the same size-dependent trend. These observations provide another strong indication that the two PL peaks are not due to two different QD subensembles within the samples, but rather reflect an intrinsic property of PbSe QDs. The origin of the energy separation between the two peaks will be discussed below.

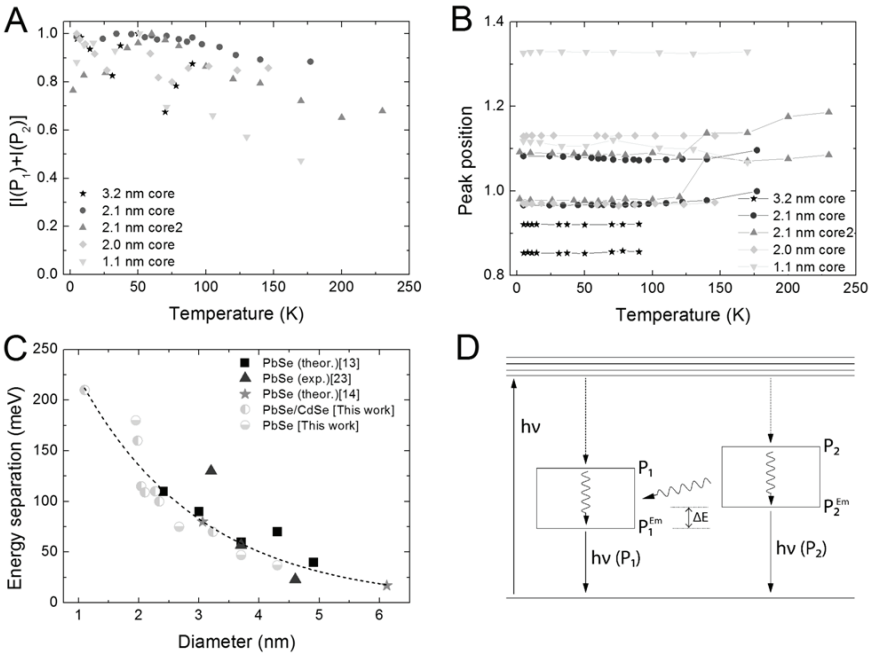

Figure 6.9: A) Total emission intensity ($I(P_1)+I(P_2)$) of PbSe/CdSe core/shell QD samples with various sizes as a function of temperature. B) Temperature dependence of the positions of the lower- and higher-energy PL peaks of PbSe/CdSe core/shell QDs. C) Energy separation between the higher- and lower-energy PL peaks as a function of the PbSe core diameter. Experimental data for PbSe QDs obtained in this work and from ref. [25] are also included. The values from ref. [25] were obtained for PbSe QD solids, while our data concerns diluted suspensions of colloidal PbSe QDs. The theoretically predicted inter-valley coupling splitting in the $1S_h$ –$1S_e$ exciton fine structure of PbSe QDs is also included for comparison using the values calculated by An et al. [14] and Allan and Delerue. [13] The dashed line is a guide to the eye. D) Schematic representation of the two states. The lower line represents the ground state while the top lines represent higher energy levels. The boxes (P_1 and P_2) represent (parts) of the 64-fold 1st excited state ($1S_h$ –$1S_e$). ΔE is the energy difference between the two emitting states.

6.3.3 Photoluminescence Decay Rates

Figure 6.10A presents room temperature PL decay curves for a series of PbSe/CdSe core/shell QD samples with decreasing core size, obtained from 3.7 nm diameter PbSe QDs. The decay curve of the parent PbSe QDs is also shown. The decay transients were acquired while monitoring the maximum of the PL peak, which corresponds to a wavelength in between the two PL peaks mentioned above. It can be clearly seen that the PL decay rates decrease as the volume of the PbSe core decreases. The slightly nonexponential decay curves can be accurately fitted with log-normal distribution functions[27] (Figure 6.10B). The results show that the average lifetime increases as the volume of the PbSe cores decreases, with a concomitant broadening in the distribution of decay rates. It is reasonable to assume that the inhomogeneity of the PbSe/CdSe core/shell QDs in the sample (i.e., distribution of core volumes) is the main cause of the slightly multiexponential character of the observed decay curves. It is of interest to distinguish the decay dynamics of the two radiative transitions by monitoring narrow spectral regions pertaining to the two peaks. Figure 6.10C presents the PL decay curves measured at $E(P_1)$ (0.99 eV) and at $E(P_2)$ (1.07 eV) for the PbSe/CdSe core/shell QD sample with 2.1 nm diameter core at 5 K. The decay curves can be fitted with a log-normal distribution function, which yields slightly faster average decay rates for P_2 (viz., 9.3×10^4 and 6.3×10^4 s, for P_1 and P_2 respectively). If we assume that the contribution from nonradiative recombination can be neglected it can be concluded that the radiative decay rates of both intrinsic transitions differ by a factor of ≈1.5, where a factor of 2 is expected based on the difference in emission energies. This shows that the transition dipole moments for the two transitions are similar.

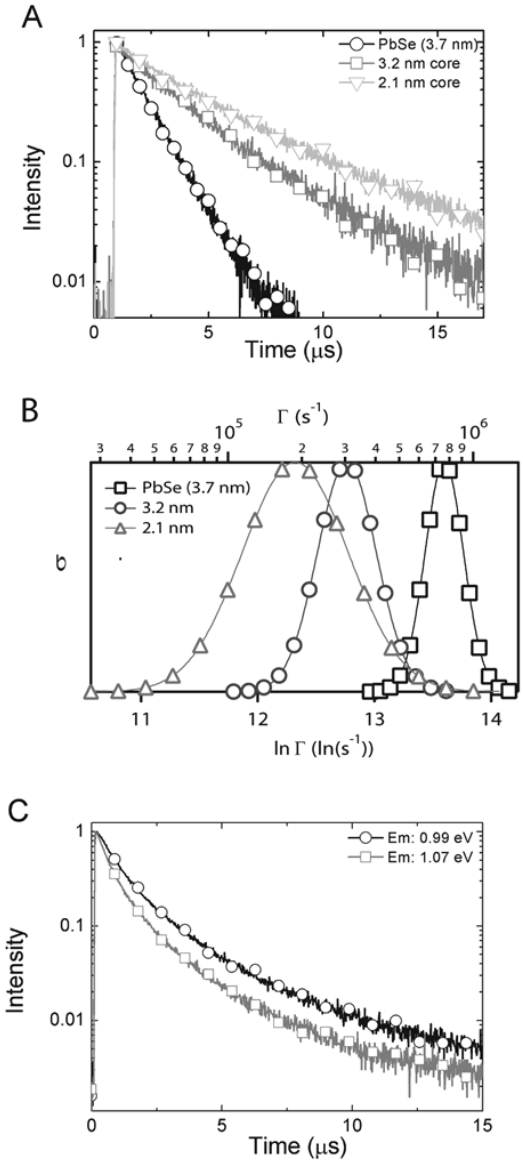

Figure 6.10: A) Room-temperature photoluminescence decay curves of PbSe/CdSe core/shell QDs obtained from 3.7 nm diameter PbSe QDs by Pb/Cd ion exchange. The total diameter is preserved, while the PbSe core diameter decreases with increasing reaction time (viz. , 5 min: 3.2 nm; 60 min: 2.1 nm). The PL decay curve of the parent PbSe QDs is also shown for comparison. The monitored wavelengths correspond to the maximum of the PL peak in all cases. B) Decay-rate distributions obtained by fitting the decay curves to log-normal distribution functions, where Γ is the decay rate and σ gives the relative probability that a given decay rate occurs (for clarity, the maxima of σ have been normalized to one). C) PL decay curves of PbSe/CdSe core/shell QDs with a 2.1 nm core (total diameter: 3.7 nm) measured at 5 K. The decay transients were obtained for two different emission energies (0.99 and 1.07 eV), corresponding to the peak positions of the lower- and higher-energy emission, respectively.

6.3.4 Exciton Fine Structure in the PL Spectra of PbSe NCs

The results above show that PbSe and PbSe/CdSe core/ shell QDs have two emitting states in the 64-manifold $1S_e - 1S_h$ exciton state. It could be argued that the lower-energy peak (P_1) is due to radiative recombination via surface or interfacial states. However, it should be realized that PbSe QDs of sizes similar to the PbSe cores investigated here also show a two-fold PL peak, with very similar separations between the two peaks, both in diluted colloidal suspensions and QD solids (Figure 6.9C). It is extremely unlikely that widely different interfaces (viz., the oleic acid-capped PbSe QD surface in solution, in the QD solid, and at the PbSe/ CdSe hetero-interface) would show exactly the same type of localized states. Moreover, trap-related radiative recombination was excluded by Harbold and Wise[25] as the origin for the double PL peak observed in their work on PbSe QD solids. In this case the PL spectra maintained their shape when the excitation densities were varied over many orders of magnitude. The absence of trap-saturation formed an argument to assign both PL peaks to intrinsic exciton states in small PbSe QDs.[25] The absence of optically active surface traps is in line with the results of tight-binding[13] and first principle calculations[15] for PbSe QDs. Furthermore, the PL excitation spectra (see Figure 6.7) clearly shows the existence of two intrinsic states wherein the peak intensities indicate that the higher-energy state has a somewhat stronger absorption (emission) strength then the lower-energy peak. This is in line with the PL decay curves, which show a higher decay rate for the emission at higher energies. Hence, excitation and emission in PbSe and PbSe/CdSe core/shell QDs can be schematically represented as shown in Figure 6.9D.

The intricate electronic structure of PbSe QDs has received much attention. It has been theoretically found that the 64-fold degeneracy of the $1S_h - 1S_e$ exciton is partially lifted by inter-valley coupling, anisotropy, and valence band–conduction band coupling. An et al. have discussed in detail the effects of intervalley coupling and electron–hole exchange on the allowed exciton transitions.[14] For PbSe QDs of 3.06 nm diameter they find that inter-valley coupling leads to two allowed transitions separated by 80 meV. This is in good agreement with the energy separation observed between the two PL peaks of the PbSe/ CdSe core/shell (3.2 nm core) QD sample investigated here (Figure 6.9C). Delerue and Allan found that inter-valley coupling splits the electron and hole energy levels into groups.[13] The energy separation between these groups increases when the PbSe NC size is reduced below 4 nm.[13] The exciton states themselves were not discussed. Harbold and Wise[25] compared the energy separation between the double-peaks observed in the low temperature PL spectra of PbSe QDs (3–4.6 nm in diameter) with the maximum inter-valley splitting calculated from the energy level splitting reported by Allan and Delerue[13] and found a fair agreement. In Figure 6.9C we plot the energy separation between the two PL peaks ($E(P_2)$ -$E(P_1)$) as a function of the PbSe core size for both the PbSe/CdSe core/shell QDs and the PbSe colloidal QDs investigated here. The data obtained by Harbold and Wise[25] is also included. It is clear that there is a good agreement between the energy

separation, the inter-valley-splitting calculated by An et al.,[14] and the maximum splitting derived from the energy levels calculated by Delerue and Allan.[13] This suggests inter-valley coupling as the most likely origin of the two-fold exciton emission observed in both PbSe and PbSe/CdSe core/shell QDs.

The observation of two exciton emissions separated by 70–210 meV over a broad temperature range is quite remarkable since it implies the kinetic isolation of the two emitting states and the absence of any thermalization between these states. In the case of thermal equilibrium only luminescence from the lower exciton state would be observed in the low temperature range, i.e., $k_B T << (E(P_2) - E(P_1))$. Hence, it is likely that after the absorption of a nonresonant photon there is a comparable probability that the higher exciton state relaxes into one of the two emitting fine-structure $1S_h$–$1S_e$ exciton states (Figure 7D, P_1 and P_2). The excitation spectra show that the higher-energy state can relax into the lower one, but the temperature dependence of both peaks excludes thermal equilibration. We note that the coexistence of emission from two different states without thermalization is a common occurrence in organic molecules (viz., singlet and triplet states). It has also been reported for s^2-ions where emission from two minima in the Jahn–Teller split excited sp state occurs,[28, 29] but is unusual for semiconductor NCs at low excitation densities. Nevertheless, the observation of two coexisting emission transitions has been recently reported for CdTe/CdSe hetero-NCs, and was ascribed to two exciton emitting states with different degrees of spatial localization.[30] In the case of PbSe and PbSe/CdSe core/shell QDs the two emitting states should be ascribed to fine-structure exciton states originating from a partial lifting of the 64-fold degeneracy of the $1S_h$–$1S_e$ exciton by inter-valley coupling and electron–hole exchange interactions. It is also striking that both states show a large shift (>200 meV) between the lowest energy absorption and the emission (Figure 6.9D). Each state shows strong relaxation effects wherein the higher-energy state can also relax into the lower-energy state. In contrast to what was reported by Harbold and Wise,[25] up-conversion has not been observed in the present work under laser excitation.

The results presented here show that there is an intriguing dependence of the relative intensities of the two PL peaks on the temperature. For example, Figure 6.8 shows that in the 5–90 K temperature range the high-energy peak gains intensity with increasing temperature while the low-energy peak becomes weaker with the total PL intensity remaining (nearly) constant. A minimum in $I(P_1)/(I(P_1) + I(P_2))$ is reached at 90 K, after-which further temperature increases result in the low-energy peak regaining intensity and the high-energy peak becoming weaker. Most likely this reflects thermal communication with dark states of the 64-fold degenerate $1S_e$ –$1S_h$ manifold. It is beyond the scope of the present work to obtain a quantitative understanding of this intriguing behavior.

6.4 Conclusion

In summary, we report the occurrence of two radiative transitions in colloidal PbSe and PbSe/CdSe core/ shell quantum dots. We present strong evidence that the two emitting states can be attributed to two bright excitons originating from the $1S_h$–$1S_e$ manifold of PbSe QDs. It is highly likely that the energy separation between these two states is caused by inter-valley coupling and electron–hole exchange. The evolution of the two luminescence peaks with the temperature is nontrivial and implies an intricate communication between bright and dark states. The understanding of this unusual temperature dependence will require new theoretical efforts.

References

1. Rauch, T.; Boberl, M.; Tedde, S. F.; Furst, J.; Kovalenko, M. V.; Hesser, G.; Lemmer, U.; Heiss, W.; Hayden, O. *Nature Photonics* **2009,** 3, (6), 332.
2. Konstantatos, G.; Howard, I.; Fischer, A.; Hoogland, S.; Clifford, J.; Klem, E.; Levina, L.; Sargent, E. H. *Nature* **2006,** 442, (7099), 180.
3. Groiss, H.; Kaufmann, E.; Springholz, G.; Schwarzl, T.; Hesser, G.; Schaffler, F.; Heiss, W.; Koike, K.; Itakura, T.; Hotei, T.; Yano, M.; Wojtowicz, T. *Applied Physics Letters* **2007,** 91, (22), 222106.
4. Heiss, W.; Groiss, H.; Kaufmann, E.; Hesser, G.; Boberl, M.; Springholz, G.; Schaffler, F.; Koike, K.; Harada, H.; Yano, M. *Applied Physics Letters* **2006,** 88, (19), 192109.
5. Lambert, K.; Geyter, B. D.; Moreels, I.; Hens, Z. *Chemistry of Materials* **2009,** 21, (5), 778.
6. de Mello Donega, C. *Chemical Society Reviews* **2011,** 40, (3), 1512.
7. Sukhovatkin, V.; Hinds, S.; Brzozowski, L.; Sargent, E. H. *Science* **2009,** 324, (5934), 1542.
8. Trinh, M. T.; Houtepen, A. J.; Schins, J. M.; Hanrath, T.; Piris, J.; Knulst, W.; Goossens, A. P. L. M.; Siebbeles, L. D. A. *Nano Letters* **2008,** 8, (6), 1713.
9. Law, M.; Beard, M. C.; Choi, S.; Luther, J. M.; Hanna, M. C.; Nozik, A. J. *Nano Letters* **2008,** 8, (11), 3904.
10. Sashchiuk, A.; Amirav, L.; Bashouti, M.; Krueger, M.; Sivan, U.; Lifshitz, E. *Nano Letters* **2003,** 4, (1), 159.
11. Wise, F. W. *Accounts of Chemical Research* **2000,** 33, (11), 773.
12. Moreels, I.; Lambert, K.; De Muynck, D.; Vanhaecke, F.; Poelman, D.; Martins, J. C.; Allan, G.; Hens, Z. *Chemistry of Materials* **2007,** 19, (25), 6101.
13. Allan, G.; Delerue, C. *Physical Review B* **2004,** 70, (24), 245321.
14. An, J. M.; Franceschetti, A.; Zunger, A. *Nano Letters* **2007,** 7, (7), 2129.
15. Franceschetti, A. *Physical Review B* **2008,** 78, (7), 075418.
16. Leitsmann, R.; Bechstedt, F. *Physical Review B (Condensed Matter and Materials Physics)* **2008,** 78, (20), 205324.
17. Pietryga, J. M.; Werder, D. J.; Williams, D. J.; Casson, J. L.; Schaller, R. D.; Klimov, V. I. *Journal of the American Chemical Society* **2008,** 130, (14), 4879.
18. Heiss, W.; Groiss, H.; Kaufmann, E.; Hesser, G.; Boberl, M.; Springholz, G.; Schaffler, F.; Leitsmann, R.; Bechstedt, F.; Koike, K.; Harada, H.; Yano, M. *Journal of Applied Physics* **2007,** 101, (8), 081723.
19. Houtepen, A. J.; Koole, R.; Vanmaekelbergh, D.; Meeldijk, J.; Hickey, S. G. *Journal of the American Chemical Society* **2006,** 128, (21), 6792.
20. Grodzinska, D.; Pietra, F.; van Huis, M. A.; Vanmaekelbergh, D.; de Mello Donega, C. *Journal of Materials Chemistry* **2011,** 21, (31), 11556.

21. De Geyter, B.; Justo, Y.; Moreels, I.; Lambert, K.; Smet, P. F.; Van Thourhout, D.; Houtepen, A. J.; Grodzinska, D.; de Mello Donega, C.; Meijerink, A.; Vanmaekelbergh, D.; Hens, Z. *ACS Nano* **2010,** 5, (1), 58.
22. Liljeroth, P.; van Emmichoven, P. A. Z.; Hickey, S. G.; Weller, H.; Grandidier, B.; Allan, G.; Vanmaekelbergh, D. l. *Physical Review Letters* **2005,** 95, (8), 086801.
23. Koole, R.; Allan, G.; Delerue, C.; Meijerink, A.; Vanmaekelbergh, D.; Houtepen, A. J. *Small* **2008,** 4, (1), 127.
24. Swart, I.; Sun, Z.; Vanmaekelbergh, D. l.; Liljeroth, P. *Nano Letters* **2010,** 10, (5), 1931.
25. Harbold, J. M.; Wise, F. W. *Physical Review B* **2007,** 76, (12), 125304.
26. Grodzińska, D.; Evers, W. H.; Dorland, R.; van Rijssel, J.; van Huis, M. A.; Meijerink, A.; de Mello Donegá, C.; Vanmaekelbergh, D. *Small* **2011,** 7, (24), 3493.
27. van Driel, A. F.; Nikolaev, I. S.; Vergeer, P.; Lodahl, P.; Vanmaekelbergh, D.; Vos, W. L. *Physical Review B* **2007,** 75, (3), 035329.
28. Jacobs, P. W. M. *Journal of Physics and Chemistry of Solids* **1991,** 52, (1), 35.
29. Oomen, E. W. J. L.; Smit, W. M. A.; Blasse, G. *Chemical Physics Letters* **1984,** 112, (6), 547.
30. de Mello Donegá, C. *Physical Review B* **2010,** 81, (16), 165303.

Samenvatting

De laatste decennia is er veel interesse de vorming en eigenschappen van colloïdale nanokristallen. Tegenwoordig zijn er vele verschillende synthese en preparatie methodes beschikbaar wat geleid heeft tot een goede controle over de grote, vorm en chemische samenstelling van deze nanokristallen. Maar wat zijn nanokristallen eigenlijk en waarom zijn ze zo interessant? Nanokristallen zijn kristallen waar minimaal 1 van de dimensies slechts enkele nanometers groot is. De eigenschappen van een materiaal veranderen wanneer de atomen 'telbaar' worden, zo tussen de ~100-100.000 atomen. We beschouwen als voorbeeld halfgeleiders, kristallen waarbij een met elektronen gevulde band is gescheiden van een lege geleidingsband door een zogenoemde bandkloof. De grote van de bandkloof wordt direct bepaald door de grote van het nanokristal. Halfgeleidende materialen kunnen licht absorberen (wanneer deze een grotere energie heeft dan de bandafstand) en uitzenden (emitteren, de energie van de grote van de bandafstand). Door de grote van het halfgeleidende nanokristal, ook wel kwantum dot genoemd, te variëren, en dus de afstand tussen de gevulde band en de lege band te veranderen, kunnen de emissie en de absorptie kwantum energie gevarieerd worden van het nabije infrarood tot ver in het zichtbare gebied. Zo emitteert bijvoorbeeld een cadmium selenide (CdSe) nanokristal van 3 nm groen en een CdSe nanokristal van 6 nm rood licht.

Het is zeer interessant om deze colloïdale nanokristallen te ordenen in een rooster (zogenaamd superrooster) om zo een macroscopische grote vaste stof te creëren bestaande uit nanokristallen als bouwstenen. Naast de mogelijkheid om één soort nanokristallen in een superrooster te brengen kan het ook interessant zijn om twee (of meerdere) soorten nanokristallen met verschillende eigenschappen in een zogenoemd binair (tweevoudig) superrooster te brengen. De elektronische structuur en de optische eigenschappen van dergelijke superroosters worden bepaald door de aard van de individuele bouwstenen en hun (kwantum mechanische) interactie.

Er zijn twee mogelijkheden om nanokristallen in het superrooster te krijgen. Men kan beginnen met een vaste stof van het gewenste materiaal en hier gedeeltes uit weg te 'etsen' en zodoende een patroon op nano- of micrometer schaal te creëren. Echter, dit is een arbeidsintensief en duur proces waarbij het tevens moeilijk is om een hoge complexiteit te behalen. Een andere methode is om met voorafgemaakte nanokristallen in een suspensie te beginnen en deze te laten zelforganiseren in een superrooster. Deze methode is mogelijk omdat nanokristallen de eigenschap hebben om colloïdale roosters te vormen. Dit betekent dat het energetisch gunstiger is dat ze allen bij elkaar in een geordend (hexagonaal) rooster gaan zitten dan in de ongeorganiseerde vloeibare equivalent met dezelfde deeltjes dichtheid.

Alles in de natuur is gebaseerd op het minimaliseren van de vrije energie van het systeem, zo ook bij spontane zelforganisatie. Er zijn twee drijvende factoren die belangrijk zijn om deze energie te minimaliseren, de entropie en de enthalpie. Entropie is een maat voor de wanorde van een systeem. Een systeem streeft naar zoveel mogelijk vrijheid, en dus naar zoveel mogelijk verschillende toestanden. Het is daarom gunstiger voor deeltjes om ver van elkaar af (wanordelijk) te zijn. Echter, een deeltje in een superrooster heeft meer vrijheid (en dus een gunstigere entropie), dan in een wanordelijke staat met dezelfde dichtheid. Dit leidt tot de verassende conclusie dat colloïdale kristallisatie gepaard kan worden met een toename in entropie. De tweede kracht, de enthalpie, is de energie die de deeltjes (onderling) ondervinden. De enthalpie verandering is gerelateerd aan verschillende krachten, bijvoorbeeld aantrekkingkracht tussen de deeltjes (van der Waals krachten (vdW)) of de aantrekkingkrachten van twee tegengesteld geladen deeltjes. In hoofdstuk 1 wordt een uitgebreidere uitleg gegeven over de drijvende krachten achter de zelforganisatie.

Wil zelforganisatie van nanokristallen ooit toepasbaar worden, dan moeten de drijvende krachten bekend zijn en gemanipuleerd kunnen worden. Zo zijn de vdW krachten tussen twee halfgeleidende deeltjes klein en wordt er dus zelforganisatie op basis van entropie toename verwacht. Bij de combinatie van twee soorten metaal deeltjes (of een metaal deeltje en een halfgeleidend deeltje) zijn de attractieve interacties tussen de deeltjes veel groter en dus niet meer verwaarloosbaar. Daardoor is het moeilijker te voorspellen wat voor soort structuren er gevormd kunnen worden. Hoofdstuk 2 beschrijft een onderzoek naar de krachten die belangrijk zijn in de binaire zelforganisatie van halfgeleidende (lood selenide (PbSe) en CdSe nanokristallen) en metallische (goud (Au)) deeltjes. Een mix van de twee soorten nanokristallen in suspensie wordt gecontroleerd, en de gevormde structuren worden met Transmissie Elektron Microscopie (TEM) en elektron tomografie onderzocht. De experimentele parameters die veranderd worden zijn de verhouding in concentratie en grootte van de twee soorten deeltje en de temperatuur. De gevormde structuren worden vergeleken met de structuren die voorspeld worden door “harde bollen” modellen (geen interactie tussen de deeltjes). We tonen aan dat de kristallisatie van de superroosters bestaande uit twee soorten halfgeleidende deeltjes entropie gedreven is. Dit is in tegenstelling tot de kristallisatie van halfgeleidende en metallische deeltjes waarbij er nagenoeg geen overeenstemming met het model is, en dus de interacties tussen de deeltjes niet te verwaarlozen is.

Naast binaire zelforganisatie is het ook mogelijk om een hogere complexiteit toe te voegen en de zelforganisatie uit suspensies met drie soorten kristallen te bestuderen. Hoofdstuk 3 beschrijft het eerste echte superkristal bestaande uit 3 verschillende bouwstenen; een zogenoemd ternair superkristal. Het ternair superkristal bestaat uit PbSe met twee verschillende diameters en CdSe nanokristallen. Door middel van elektron tomografie, een techniek die uit 2D TEM projecties een 3D reconstructie maakt, wordt aangetoond dat het

ternaire kristal isostructureel is met de atomaire structuur van Aluminium Magnesium tetra Boride ($AlMgB_4$).

Hoofdstuk 4 beschrijft hoe elektron tomografie kan worden gebruikt om tot een correcte interpretatie van 2D TEM plaatjes te komen. Twee voorbeelden worden gegeven waarbij tomografie meer inzicht verschaft en zelfs onmisbaar is voor een goede interpretatie. In het eerste voorbeeld wordt voor 4 bekende binaire superkristallen bestaande uit PbSe, CdSe en Au geïllustreerd dat dubbelzinnige interpretatie van 2D TEM data kan worden voorkomen, diepliggende defecten bestudeerd en dat de orde/wanorde aan de boven en onderkant van het binaire superrooster kan worden bekeken. De resultaten laten zien dat het waarschijnlijk is dat de zelforganisatie (nucleatie en groei) plaatsvindt aan het vloeistof-lucht oppervlak en dus niet in de oplossing of op het substraat. Het tweede voorbeeld beschrijft de analyse van drie verschillende projecties van kristal structuren die drie verschillende superroosters suggereren. Met behulp van elektron tomografie hebben we de chemische samenstelling en eenheidscellen van de drie samples bepaald. Voor zover ons bekend is, heeft de A_6B_{19} kristal structuur geen atomair equivalent.

In hoofdstuk 5 staat de zelforganisatie van één type deeltjes centraal, de georiënteerde zelf organisatie van PbSe nanokristallen op een vloeibaar (ethyleen glycol) substraat. Georiënteerde aanhechting is een proces waarbij de nanometer-grote kristallen fuseren door dat kristal vlakken met atomaire precisie aan elkaar hechten, waardoor een micrometer groot éénkristal gevormd wordt. Naar verwachting is georiënteerde aanhechting moeilijker te controleren dan zelforganisatie. Echter, hoofdstuk 5 laat zien dat deze aanname niet waar hoeft te zijn. Door simpele parameters in de synthese the veranderen, zoals temperatuur en concentratie, kan georiënteerde aanhechting van PbSe nanokristallen in 1 of 2 dimensies gecontroleerd worden en dat 1D staafjes en 2D vierkante en honingraatachtige éénkristallen kunnen worden gegroeid. Tevens kunnen deze kristallen, bestaande uit PbSe, omgevormd worden tot andere materialen door selectief één van de twee atomen, namelijk Pb, uit te wisselen voor Cd of Cu en zodoende CdSe of Cu_2Se eenkristallen te verkrijgen met een vierkante of honingraat nanogeometrie.

In hoofdstuk 6 worden de optische eigenschappen van PbSe(kern)/CdSe(schil) colloïdale hetero kristallen in detail onderzocht met tijds-opgeloste fotoluminescentie spectroscopie. De PbSe|CdSe colloïden worden gemaakt startende uit PbSe kernen waarbij Cd-voor-Pb uitwisseling wordt gebruikt om een CdSe schil te groeien. De foton emissie die gepaard gaat met de overgang van een elektron van een hoog naar een lager gelegen energie niveau van deeltjes met een PbSe kern kleiner dan 4 nm laat twee pieken in het emissie spectrum zien die verder uit elkaar gaan liggen naarmate de kern grootte kleiner wordt. Er wordt aangetoond dat de luminescentie pieken een intrinsiek eigenschap zijn van kleine PbSe(kern)/CdSe(schil) nanokristallen. De kristal structuur van de kern leidt tot een 64-voudige exciton structuur; de degeneratie van deze exciton structuur wordt deels

vernietigd door koppeling tussen twee verschillende karakteristieke L-punten in de Brillouin zone en door elektron-gat uitwisseling. Hierdoor ontstaan twee groepen van licht emitterende (toegelaten) exciton overgangen naast verschillende groepen van verboden exciton overgangen. Deze theorie kan echter niet verklaren waarom er geen thermisch evenwicht is tussen de twee groepen van toegelaten overgangen.

List of publications

This thesis is based on the following publications:

- Evers, W.H.; Goris, B.; Bals, S; Casavola., M.; de Graaf, J.; van Roij, R.; Dijkstra, M.; Vanmaekelbergh, D. Low-dimensional semiconductor superlattices formed by geometric control over nanocrystal attachment; Submitted, **2012**

- Boneschanscher, M.P. Evers, W.H.; Qi, W.; Meeldijk, J.D.; Dijkstra, M.; Vanmaekelbergh. D.; Electron tomography resolves a complex and novel crystal structure in a nanocrystal assembly; Submitted, **2012**

- Grodzińska, D.; Evers, W. H.; Dorland, R.; van Rijssel, J.; van Huis, M. A.; Meijerink, A.; de Mello Donegá, C.; Vanmaekelbergh, D. Two-fold emission from the S-shell of PbSe/CdSe core/Shell quantum dots; *Small* **2011,** 7, (24), 3493-3501.

- Evers, W. H.; Nijs, B. D.; Filion, L.; Castillo, S.; Dijkstra, M.; Vanmaekelbergh, D. Entropy-driven formation of binary semiconductor-nanocrystal superlattices; *Nano Letters* **2010,** 10, (10), 4235-4241.

- Evers, W. H.; Friedrich, H.; Filion, L.; Dijkstra, M.; Vanmaekelbergh, D. Observation of a ternary nanocrystal superlattice and its structural characterization by electron tomography; *Angewandte Chemie International Edition* **2009,** 48, (51), 9655-9657.

- Friedrich, H., Gommes, C.J., Overgaag, K., Meeldijk, J.D., Evers, W.H., de Nijs, B., Boneschanscher, M.P., de Jongh, P.E., Verkleij, A.J., de Jong, K.P., van Blaaderen, A., Vanmaekelbergh, D. Quantitative structural analysis of binary nanocrystal superlattices by electron tomography. *Nano Letters* **2009,** 9, (7), 2719-2724.

- Overgaag, K., Evers, W., de Nijs, B., Koole, R., Meeldijk, J., Vanmaekelbergh, D. Binary superlattices of PbSe and CdSe nanocrystals. *Journal of the American Chemical Society* **2008**, 130, (25), 7833-7835.

Other publications

- Pietra, F.; Rabouw, F. T.; Evers, W. H.; Byelov, D. V.; Petukhov, A. V.; de Mello Donegá, C..; Vanmaekelbergh, D. GISAXS study of semiconductor nanorod self-assembly at the liquid/air interface. *Submitted,* **2012**.

- Pijpers, J. J. H.; Koole, R.; Evers, W. H.; Houtepen, A. J.; Boehme, S.; de Mello Donegá , C.; Vanmaekelbergh, D.; Bonn, M. Spectroscopic studies of electron injection in Quantum dot sensitized mesoporous oxide films; *The Journal of Physical Chemistry C* **2010**, 114, (44), 18866-18873

Acknowledgements

A PhD thesis, although designated to only one person, would not be possible without the help of many people and collaborations. In this part I would like to thank all the people involved in helping me bringing my PhD thesis to a good finish.

First of all I would like to thank my promoters Daniël Vanmaekelbergh and Andries Meijerink for providing the opportunity to work in the CMI group, for always being enthusiastic for whenever I came with a new structure and always seeing new research opportunities. Also, for giving me the freedom to perform my research and the help with writing it down.

Next I would like to express my gratitude towards the whole of the CMI group; Alex, Andries, Bert, Celso, Dariusz, Dominika, Denis, Esther, Francesca, Freddy, Hans, Harold, Ingmar, John, Joost, Joren, Linda, Marianna, Mark, Onno, Peter, Philipp, Relinde, Rosa, Stephan, Yiming, Zachar, Zhixiang and all the students who came and went during my time here. I had a lot of fun in the group and learned a lot from you. Special thanks I would like to express to the people with whom I had collaborations. Mark, Hans and Heiner for the corporation with the TEM tomography and Sara and Bart for providing the nice high resolution HAADF-STEM images. Freddy, Dima and Francesca for the measurements at the ESRF, (and for all the 'Friday afternoon' experiments which led to this research). Marianna, for providing me with specially shaped particles. The help of Laura, Joost and Marjolein was also vital for theoretical input for my practical work, my thanks for this! Dominika for our collaboration with the optical work which resulted in a nice chapter in our theses. Also is would not be possible to finish any PhD without technical help! Therefore, I thank Stephan for helping to keep my computer 'alive'. I would like to appreciate special thanks to Hans for helping me build all kind of set-ups which we thought of, without it my research would have been completely different. I would also like to thank my office mates, Esther, Rosa, Timon and Denis for the fun time and the (non)scientific conversations.

Als laatste zou ik mijn familie willen bedanken die me altijd de mogelijkheid hebben gegeven om te studeren wat uiteindelijk tot deze thesis geleid heeft.

Curriculum Vitae

Wiel Evers was born on May 14th 1985 in Weert, the Netherlands. In 2002 he obtained his high school degree ("HAVO") at Scholen gemeenschap Sint Ursula in Horn. In the same year he started his bachelor "Toegepaste natuurwetenschappen" (applied sciences, chemistry) at the Fontys hogescholen and obtained his bachelor degree in 2006. For his master he went to the Utrecht University where he did the master "Nanomaterials: Chemistry and physics". His master research was performed in the group of Condensed Matter and Interfaces (CMI) at the Utrecht University under supervision of Prof. Daniel Vanmaekelbergh, where he investigated the self-assembly of nanocrystals.
After obtaining his master degree in 2008 he continued on the topic of his master research and joined the CMI group as a PhD student under supervision of Prof. Daniel Vanmaekelbergh and Prof. Andries Meijerink. Most results of this PhD project are described in this thesis and published in peer-reviewed scientific journals. Besides his research activities he supervised three master and four bachelor students and assisted in the first year analytical course and the quantum chemistry course of first year students.